APPLICABILITY OF CHRONICALLY IMPLANTABLE AND TRANSPARENT MICROECOG DEVICES FOR SIMULTANEOUS MEASUREMENT OF SPONTANEOUS CALCIUM AND ELECTROPHYSIOLOGICAL ACTIVITY IN AWAKE MICE

PhD thesis

Madarász Miklós

János Szentágothai Doctoral School

Semmelweis University

Supervisor:	Dr. Rózsa Balázs, MD, Ph.D
Official reviewers:	Dr. Dávid Csaba, Ph.D
	Dr. Borbély Sándor, Ph.D
Head of the Final Exam. Committee:	Prof. Kamondi Anita, MD, D.Sc
Members of the Final Exam. Committee:	Dr. Varga Viktor, Ph.D
	Dr. Kis Petiková Katarína, Ph.D

Budapest
2025

Table of Contents

List of Abbreviations

3D three dimensional
AAV adeno-associated virus
ACSF artificial cerebrospinal fluid
Al RIE aluminum reactive ion etching
ANOVA analysis of variance
AO acousto-optical
AP antero-posterior
AR amplitude ratio
BCI brain–computer interface
BI burstiness index
CA1 Cornu Ammonis 1
CaM Calmodulin
CCPE combined constant phase element
CPE constant phase element
DAPI 4′,6-diamidino-2-phenylindole
DC direct current
DV dorsoventral
ECoG electrocorticography
EEG electroencephalography
EIS electrode impedance spectroscopy
FOV field of view
FWHM full width at half maximum
GFAP glial fibrillary acidic protein
GFP green fluorescent protein
I.p. intraperitoneally
IQR interquartile range
IR infrared
ITO indium tin oxide
LFP local field potential
MEA multielectrode array
MEMS micro-electro-mechanical system
ML medio-lateral
MUA multi-unit activity
NA numerical aperture
NIR near-infrared
PFA paraformaldehyde
PBS phosphate buffered saline
PDMS polydimethylsiloxane
PEDOT Poly(3,4-ethylenedioxythiophe
PET Polyethylene terephthalate
PMT photomultiplier tube
PSF Point Spread Function
PSS polystyrene sulfonate
RCT charge transfer resistance
ROI region of interest
RPM rotations per minute
SD standard deviation
SEM standart error of the mean
SIROF sputtered iridium oxide film
SMP shape memory polymer
SNR signal-to-noise ratio
SPW-R sharp wave – ripple
SUA single-unit activity
TIFF tagged image file format
UV ultraviolet
V1 primary visual cortex
VIS visible
WD Warburg element

1. Introduction

Neuroimaging methods are extensively combined with other experimental techniques in the field of neuroscience in recent years, to study neural activity and map brain connectivity [Hillman, 2007]. This combined approach allows brain mechanisms and pathological states to be understood and contributes to the identification of biomarkers for neurological diseases. Among the techniques used for monitoring brain activity, electrophysiology is still the gold standard, despite the advent of optical characterization tools like optogenetics, calcium imaging or voltage imaging [Scanziani 2009]. The limitations of individual neuroimaging techniques have compelled neuroscientists to combine multiple approaches, such as electrophysiology with functional magnetic resonance imaging, multiphoton imaging or optogenetics [Hillman 2007, Uludağ 2014]. Neuroimaging techniques can provide the desired spatial information that complements the information obtained from electrophysiological techniques such as electrocorticography (ECoG). The emergence of multimodal measurements that utilize both electrophysiology and optical interrogation [Malvache 2016, Judák 2022] catalyzed the development of transparent neural interfaces that enable the application of both modalities. Electrophysiological methods with high temporal resolution are therefore often used in parallel with a non-invasive optical method with high spatial resolution [Fekete 2017]. Transparent neural interfaces designed specifically for experimental and clinical studies may help to understand how the brain processes information through revealing functional connectivity patterns, therefore they are promising candidates for brain–computer interfacing (BCI) technology [Hébert 2018].

In my thesis, I introduce two micro-electro-mechanical system (MEMS) based microelectrode device and present data of their capacity to enable multimodal neuronal activity measurements by combining electrocorticography and two-photon calcium imaging. I start by introducing the two measurement modalities and elaborate on MEMS-based microECoG devices and the current approaches to multimodal measurements with such devices, before discussing the results of multimodal measurements with the two devices, the first based on the composing materials Parylene HT / ITO and the latter on Thiol-ene/acrylate / SIROF.

1.1 Electrocorticography

Electrophysiology is applied in many contexts in neuroscience. Electrical activity can be measured from a small segment of a dendrite of a single neuron [Davie 2006], on the surface of the brain [Miller 2020] or on the scalp [Baumgartner 2018]. The source of the gathered information can scale from only a small membrane segment of a single cell to the summed activity of an immense population of neurons. The characterizing advantage of electrophysiology over other investigation methods that record neuronal activity is its yet unchallenged temporal resolution. The sampling rates of the different measurements typically range from 200 to 20000 samples per second, determined by redundancy rather than technical limitations [Weiergräber 2016].

Electrocorticography is one of the methods to measure the potential changes in a living brain, with arranged electrodes that measure the field potential on the surface of the brain as a function of time [Branco 2023, Buzsáki 2012, Bédard 2012]. ECoG signals are rich in frequency components that are difficult to record in a reliable manner with EEG due to the filtering properties of the skull, the subcutaneous tissue and the scalp [Burle 2015]. These frequency components cover the gamma bandwidth, which correlates with large scale brain networks, for example sensory - motor activity and cognitive functions such as memory [Schalk 2011, Muller 2018, Buzsáki 2012b]. Although ECoG devices are invasive probes that require microsurgical implantation, they offer considerable benefits over EEG devices in terms of signal quality, longevity, reliability, spatial and temporal resolution and frequency band [Moon 2024, Buzsáki, 2012a].

The cell membrane separates the intracellular and extracellular space and allows the existence of potential difference between these two compartments. Resulting from the actively maintained uneven distribution of positively and negatively charged ions, the potential difference between the intracellular and the extracellular space is around −70 mV in central nervous system neurons. The field potential measured by the ECoG is generated when charged ions move through the membrane and temporarily change the extracellular ion composition. Synaptic events, extrasynaptic ion channels, cell-intrinsic potential fluctuations and the generation of action potentials are some of the main contributors of the field potential [Hales 2014]. There are many factors that shape the extracellular signal [Mazzoni 2012, Einevoll 2013, Herreras 2016, Herreras 2023]. The

amplitude of the signals decay according to the inverse of the distance, so a source further from the electrode may contribute less to the aggregate signal [Torres 2019]. The geometric arrangement of sources has a similarly profound effect. As in- or outward currents generate counterparts with opposing signs, depending on the relative position of these dipoles and the electrode, inward and outward currents may mutually negate the registration of the other on the electrode [Herreras 2016]. On a larger scale, the cytoarchitectural arrangement of the cells in a region may prevent the generation of field potentials and therefore the registration of its activity [Kajikawa 2012, Herreras 2023]. Synchrony is another determinant of the extracellularly recorded signal. As the contribution of individual cells is small in itself, the activity of cells that are synchronously active may influence the recorded signal more [Herreras 2023]. Nevertheless, the electrocorticogram can be used to infer the underlying neuronal activity and record the oscillatory activity of large networks of neurons [Gallego-Carracedo 2022]. In clinical practice, the source epileptic seizures are explored with implanted electrocorticography devices in patients in preparation for resective surgery [Schaft 2025, Grewal 2020, Goel 2023].

1.2. Two - photon microscopy

Two-photon microscopy has evolved to be a primary tool for high spatial resolution fluorescence imaging in intact neural tissue [Helmchen 2009, Grienberger 2022]. It utilizes ultrashort pulses of near - infrared light which is directed through an optical system to excite suitable fluorophores with two low-energy photons in a short time window. The volume in which fluorophores can be excited is confined, as the high energy density that is necessary for the absorption of two-photons within the short timespan is not available outside of the focus [Stosiek 2003]. In fact, excitation light is pulsed instead of continuous specifically to provide the necessary energy. With reduced off-focal fluorescene, images can be obtained with higher contrast, from deeper in the tissue. The use of near - infrared excitation light also aids deeper imaging, as it is less scattered in the nervous tissue. Since two photons combine their energy during measurement, they are less harmful to biological tissues than single-photon excitation.

Excitation depends on the structure of the molecule excited and many dyes are incompatible with multiphoton imaging due to their insufficient absorption cross-sections [Lecoq 2019]. The activity of cells can be visualized with fluorescent dyes (fluorophores). These molecules absorb a particular wavelength band of light (excitation wavelength) and then emit light at another, longer wavelength (emission wavelength). Live cells can be labeled by local dye injection into a tissue or by the expression of genetically encoded fluorescent proteins.

Calcium indicators are the most commonly used fluorophores for in vivo two-photon imaging experiments. Two-photon calcium imaging is an efficient way to monitor the calcium-binding kinetics with a highly precise morphological image [Stosiek 2003]. This method uses the fact that in the living cells, most of the depolarizing signals are in connection with the Ca^{2+} influx because of the voltage gated Ca^{2+} channels [Tsien 2003], which allow the determination of neuronal activity indirectly, increasing fluorescence with the increase in intracellular calcium concentration. While calcium imaging is the method of choice for measuring the activity of single neurons and populations in vivo, it is afflicted by the slow kinetics of the dyes and the influence of reporters on signal integration due to the binding of calcium ions.

1.3. Transparent microECoG devices

MicroECoG devices are miniature recording systems designed to measure the electrical activity on the surface of the brain with multiple electrodes arranged in an organized layout. Their main components are the conductive layer used to record the field potential and the substrate layer, an insulating, encapsulating layer lending structure to the device. These devices enable the concurrent investigation of different brain regions [Noy 2015, He 2008], the exploration of the functional architecture of a given region [Zátonyi 2018, Konerding 2018, Donahue 2018] and the localization of pathological neuronal networks [Wang 2013, Carrette 2013, Khosravani 2009, Gompel 2008]. Integration of multiple and complementary techniques in an attempt to leverage the temporal resolution of electrophysiology and the spatial resolution of neuroimaging is expected to receive great interest in the near future, as understanding the relationship between anatomical and

functional neural connectivity is essential for both diagnostic and therapeutic applications.

Neural interfaces combining electrophysiology and neuroimaging are required to satisfy several requirements [Alahi 2021, Fekete 2024, Bhunia 2015], as neuroscience shifts increasingly toward chronic experiments on awake and behaving subjects. Recording quality, transparency, flexibility, biocompatibility and overall size are a few of the crucial design aspects. Arguably, such devices should ideally be tailored to the specific experiment for optimal performance.

1.3.1. Conductive materials

When describing the recording sites of microECoG devices, impedance is reported generally as their main attribute, as it takes all components of the equivalent circuit models of electrodes into account, therefore yields more informative data on the performance of the electrodes than conductivity. The impedance of electrodes inherently depends on the conductive material as well as on their size, with smaller recording sites having higher impedance.

High conductivity of recording sites is desired for high signal to noise ratio (SNR), however, conventionally applied thin film metal layers with excellent conductive properties like gold [Kim 2007, Hollenberg 2006], gold/platinum [Schendel 2013, Richner 2014, Muller 2018], platinum [Stieglitz 2000, Rubehn 2009] or iridium [Stieglitz 2000]) have low transparency. This introduces a trade-off, as a non-transparent conductive layer blocks imaging access to a sizeable portion of the optical window and prevent the complete imaging of the sample. There are a choice of transparent conductive materials that can be considered for microECoG devices. Nanowires [Neto 2021] and nanomeshes [Qiang 2018], carbon nanotubes [Zhang 2018], graphene [Park 2014, Kuzum 2014, Driscoll 2021], transparent conductive polymers such as PEDOT [Khodagoly 2015, Furukawa 2013, Castagnola 2015] and metal oxides like indium-tin-oxide [Qiang 2018, Hébert 2018].

Additionally, when recording sites are exposed to a particular material-specific wavelength of light, electrons are excited, and an electric artifact appears in the detected current or voltage signal, which may hinder noise-free electrical recording and limit the

evaluation of experimental outcome. This effect is also called the Becquerel effect [Han 2012], and a reasonable approach for mitigating it is the use of conductive materials with a wide bandgap, which requires a compromise during the selection of potential conductive materials. The energy bandgap of the conductive material determines the extent of optical transmission and the excitation of charged carriers. For conventionally used metals, the conduction and valence bands overlap and therefore require lower excitation energy for electrons to move to conduction bands [Fekete 2024], which leaves them more susceptible to light induced artefacts.

1.3.2. Substrate materials

Recent advances in materials science have had a transformative effect on the fabrication of microimplants that enable the simultaneous application of electrical recording and optical imaging [Wellman 2018]. A growing number of transparent substrate materials, such as polyimide [Zátonyi 2018b], SU-8 [Obaid 2020], Parylene C [Golda-Cepa 2020, Yang 2021], Parylene HT [Zátonyi 2020], polydimethylsiloxane (PDMS) [Renz 2020] and PET [Thunemann 2018, Chen 2021] have been proposed to hold functional layers of transparent neural implants. However, their material properties, transparency, flexibility and biocompatibility in particular, are of key importance in determining their final application, and their processability and manufacturing schemes also have limitations [Fekete 2024].

While it is hard to overstate the importance of transparency in a setting of optical imaging, flexibility and biocompatibility are pivotal as well. Compressive and tensile forces inherently act on neural interfaces either during the surgical procedure of implantation or due to micromotions (e.g. breathing, heartbeat, brain pulsation, circulation) inside the skull. These phenomena induce cyclic stress in the material, which may also be disadvantageous to the integrity of the layer structure of the interface. Highly tensile and tear-resistant devices [Renz 2020, Juhász 2024] therefore may ease implantation and prevent the loss recording channels. To alleviate the consequences of such mechanical processes, the elasticity and stretchability of the implant material are of key importance.

Although the implantation of microECoGs is less invasive to the brain tissue that penetrating probes, it has been reported that microECoG devices do induce foreign body

reaction — the specific immune response of the nervous system to implanted neuroprostheses [Campbell 2018, Degenhart 2016]. Stress from micromotions has been implicated as the main reason for neuroinflammatory response during prolonged presence of microECoGs, which may result in glial scar formation and finally the encapsulation of the artificial system [Marin 2010, Kim 2019, Harris 2011, Blumenthal 2025]. In chronic experiments, encapsulation of neuroprostheses will lead to unreliable electrical recordings, unstable signal quality over the extended period and eventually impedance increase or even loss of functionality, due to the spatial and electrical insulation from active neuronal ensembles [Gilletti 2006, Bérces 2016].

It is suggested that mechanically compliant neural interfaces that conform better to the curvilinear surface of the brain would be more likely to reduce stress at the biotic – abiotic interface [Harris 2011, Lecomte 2018, Jorfi 2015]. In order to maximize conformity and minimize foreign body reaction, various approaches were developed. Rigid materials were covered temporarily with soft bioresorbable polymer materials [Yu 2016, Pas 2018]. Flexible polymer materials were employed, such as polyimide [Wurth 2017, Wu 2011, Zátonyi 2018, Márton 2015, Vomero 2020], Parylene C [Konerding 2018, Vitale 2018, Park 2016, Khodagholy 2015], SU-8 [Márton 2015, Zhang 2018] and silicone rubber [Minev 2015, Hotson 2016]. MicroECoG arrays with a mesh-form structure of open interelectrode spaces, or fenestrae were fabricated to enhance the contactability with the curvilinear surface of the brain [Baek 2014, Rubehn 2009].

The proportional elastic deformation of a material can be characterized by Young's modulus, which equals the compressive or tensile stress exhibited upon the strain of the material. Unfortunately, elastic properties of the mentioned thin polymer interfaces (Young's modulus in the GPa range) [Fekete 2024] are still significantly different from the neural tissue (3-100 kPa) [Lecomte 2018]. The reduction of mechanical mismatch can be attained via a variety of routes, including bioresorbable polymer materials such as silk [Wu 2015, Watanabe 2017] and poly(lactic-coglycolic acid) [Pas 2018], mechanically adaptive substrates like hydrogel [Li 2020] and with the application of fenestrae or aperture that disrupt the consistency of the device structure [Toda 2011]. These attempts are either trying to approximate the Young's modulus of the device to the surrounding tissue or increase the compliance by forming mesh-like structures.

The group of mechanically adaptive materials consist of softening polymers (e.g. Thiol-ene/acrylate thermoset or shape memory polymers) [Simon 2017, Zátonyi 2019, Frewin 2019, Stiller 2018] and hydrogels from natural materials such as polyglycolic acid, polyethylene glycol and polyvinyl alcohol [Pas 2018, Guangli 2018, Guangli 2021]. Softening polymers transition in response to stimuli (e.g. temperature, ion concentration, pH, aqueous environment) when they are exposed to the extracellular space. They maintain their mechanical robustness (Young's modulus in the GPa range) during implantation, thus providing easy handling before and after neurosurgeries.

1.3.3. Advantages of Parylene HT / ITO

Parylene HT as a prospective substrate material for a transparent microECoG device came to our consideration via the established use of a variant, Parylene C. However, compared to Parylene C or other substrate materials, Parylene HT has several advantages that justify its choice for transparent microECoGs.

In terms of transmittance, autofluorescence and UV light stability, Parylene HT is superior to other electrode substrate materials [Lu 2009, Lu 2010]. It shows transparency greater than 90% between 400–980 nm that is remarkably higher than that of polyimide [Zátonyi 2018] or PET [Ong 2018], slightly higher than that of Parylene C and similar to SU-8 substrates [Prajzler 2014] and PDMS [Liu 2015]. Its low autofluorescence is also desired to avoid disturbing background noise. Some groups have presented initial results comparing various polymers like Parylene C, PET, polyimide [Lu 2010] or SU-8 [Walczak 2011]. Their findings indicated that among these materials, Parylene C provides the best performance in this respect. However, Parylene HT may be superior to Parylene C. Initial lower autofluorescence of Parylene HT film was attributed to the strength of C–F bond that is much higher than C–H bond. It is prone to be less sensitive to dehydrogenation, consequently the amount of C = C bonds which are responsible for higher autofluorescence intensity remains low under UV illumination [Lu 2009].

From a manufacturing point of view, the advantage of the thin layer of thermoplastic Parylene is that it can be formed by chemical vapor deposition at low ambient temperature. The deposited layer is conformal, pin-hole free, chemically inert, while showing low vapor permeability [Tan and Craighead 2010]. Parylene HT has a long-term

service temperature up to 350 °C while Parylene C and other polymers used for neural applications (e.g. epoxy, silicone) tolerate processes with only a lower thermal budget [Minami 2008]. In case of certain conductive materials with high melting point such as iridium, patterning on Parylene HT is still compatible with the potentially high deposition temperature in contrast to Parylene C [Rodger 2008]. Among the four Parylene variants, Parylene HT exhibits the lowest coefficient of friction - beneficial for biocompatibility, the lowest permeability to moisture, fluids and gases (<0.01% water absorption after 24 h) decreasing the risk of delamination due to swelling [SCS Data Sheet 2015] and shows better performance in many applications due to its lower dielectric constant [Diaham 2014].

The widely used indium-tin oxide (ITO) is formed by doping In_2O_3 with Sn impurities. Oxidation of these impurities contributes to the release of electrons in the conduction band, which leads to a net increase in charge carrier density and therefore, conductivity. ITO differs from other metallizations conventionally used for microECoG devices, such as platinum, iridium or gold, in the structure of its electron bands. While for conventionally used metals, the conduction and valence bands overlap and therefore require lower excitation energy for electrons to move to conduction bands, the conduction mechanism of ITO is instead based on oxygen vacancies. These vacancies feature large bandgap (2.6–3.65 eV) and excitation photons with wavelength from visible (VIS) to infrared (IR) spectral range have less energy, which keeps photovoltaic effects at a low level and allow simultaneous measurements [Mryasov 2001, Ledochowitsch 2015].

A popular alternative to ITO is graphene. However, the fabrication of graphene relies on stacking of graphene monolayers require complicated steps, which deteriorates uniformity and process reproducibility. Moreover, each graphene monolayer stacked to form uniform layers deteriorates the transmittance by ~2.3% [Park 2016]. On the other hand, ITO may work as standalone layer sandwiched between two thin Parlyene HT layers, requiring only two photolithography steps. Depending on its thickness and the deposition parameters, the optical transparency of ITO at VIS–NIR wavelengths is generally >80% [Park 2014, Kunori 2015, Kwon 2013, Ledochowitsch 2011, Granqvist 2002], as a result of its wide energy bandgap. Together with its lower sensitivity to photovoltaic effects, this translates to considerable benefits during imaging, as the field of view is not being limited by the metallization layer

1.3.4. Advantages of Thiol-ene/acrylate / SIROF

Minimizing the neural response improves the longevity of implants in multimodal neuroimaging schemes. The application of responsive polymers that reduce the inflammatory response by reducing the mechanical mismatch at the tissue and neural interface may be a key technology in this endeavor [Lu 2010, Thunemann 2018, Shoffstall 2018]. The group of mechanically adaptive materials constitutes of softening (or shape memory) polymers [Simon 2017, Zátonyi 2019, Frewin 2019, Stiller 2018] and hydrogels [Pas 2018, Li 2018, Li 2021].

Hydrogels, in their dry state, express a Young's modulus in the GPa range but in the aqueous environment of the intracranial space, even a few MPa is achievable (e.g., 3.4 GPa to 2.6 MPa [Lecomte 2018]). The main drawback (and controversially, the greatest appeal) of hydrogels is their excessive water absorption. Their swelling rate varies between 10% and 70%, which is an additional risk for structural degradation and metal delamination. Swelling also distances recording sites from active neurons and increases intracranial pressure. Like hydrogels, shape memory polymers such as Thiol-ene/acrylate maintain their mechanical robustness (Young's modulus in the GPa range) during implantation, thus providing easy handling before and after neurosurgeries. However, softening polymers can be engineered to undergo stimuli responsive transition (e.g., temperature, ion concentration, pH, aqueous environment) when they are exposed to the extracellular space to reduce the mechanical mismatch. The major advantage of a Thiol-ene/acrylate based microECoG device is that its Young's modulus is gradually reduced from the GPa range down to the 100 MPa range at glass transition temperature, which is engineered to be close to tissue temperature (Ware 2012), with less than 3% fluid uptake. The use of Thiol-ene/acrylate as a SMP substrate material to create neural interfaces has only been exploited recently [Ware 2014, Black 2018, Shoffstall 2018, Zátonyi 2019].

Thiol-ene based flexible devices have been characterized previously both electrically [Stiller 2018, Frewin 2019] and optically [Feidenhans'l 2014]. Thiol-ene has high optical transparency (above 85% @ 550 nm) with a refractive index of about 1.54 [Xiao 2016].

2. Objectives

Given the aforementioned advantages of Parylene HT as a substrate and ITO as a conductive layer, we set the goal of demonstrating combined electrocorticography and two - photon calcium imaging in vivo in mice chronically implanted with the Parylene HT / ITO device (Figure 1 B). This goal defined a roadmap from bench-top tests, through in vitro experiments, in vivo measurements of awake mice to post-hoc characterization, a step by step process of validation and verification. In line with this, my aims connected to the Parylene HT / ITO device were the following.

1.1 The in vivo implantation of the Parylene HT / ITO device into a cranial window in a way that enabled electrocorticography and two-photon imaging

1.2 Investigation of the limits to the in vivo use of the device, focusing on photodegradation and photovoltaic effects

1.3 Demonstration of simultaneous electrocorticography and two-photon calcium imaging, particularly long term chronic measurements

1.4 The immunohistological characterization of the implantation

Following the experiments with the Parylene HT / ITO device and building upon the experiences with it, the design and fabrication of a new device was started. The shape memory polymer Thiol-ene/acrylate was chosen as substrate, thus placing emphasis on flexibility and conformability to the brain, while iridium oxide (SIROF) was chosen as the conductive layer, favoring conductivity in place of transparency of recording sites. The dimensions of the new device were adapted to address the challenges of limited space. First, recording sites were defined to be smaller and closer to each other, arranged in a recording area that requires a smaller cranial window. Second, a more compact data connector was selected that still accomodated the same amount of recording channels. Third, the length of the ’neck’ part of the device that connects the recording area to the

connector, was carefully chosen to allow the placement of the connector directly on the skull and the imaging objective over the craniotomy at the same time.
Encouraged by these improvements, we set our sights on long term combined electrocorticography and two - photon calcium imaging again, as well as chronic hippocampal measurements potentially. My aims with the novel Thiol-ene/acrylate / SIROF microECoG device were the following.

2.1 Cortical implantation of the Thiol-ene/acrylate / SIROF device into a cranial window in a way that enabled electrocorticography and two-photon calcium imaging

2.2 Demonstration of chronic electrocorticography and two-photon calcium imaging through cortical measurements

2.3 Utilizing the improved adaptability of the Thiol-ene/acrylate / SIROF device for simultaneous hippocampal electrocorticography and two-photon calcium imaging

2.4 The immunohistological characterization of the cortical and hippocampal implantations

3. Methods

3.1. Fabrication of Parylene HT / ITO devices

In overview, the Parylene HT / ITO device holds 32 recording sites with a diameter of 150 µm and 500 µm inter-site distance (Figure 1 A, C). The outline of the sensor array is 4.5 mm × 5.5 mm. The device is composed of a 100 nm thick indium tin oxide conductive film embedded between two layers of 8 µm thick Parylene HT (SCS, UK). Conductive traces and bonding pads are made of indium tin oxide, which were connected to a PreciDiP connector. The microfabrication of the device relies on standard MEMS technologies (Figure 2).

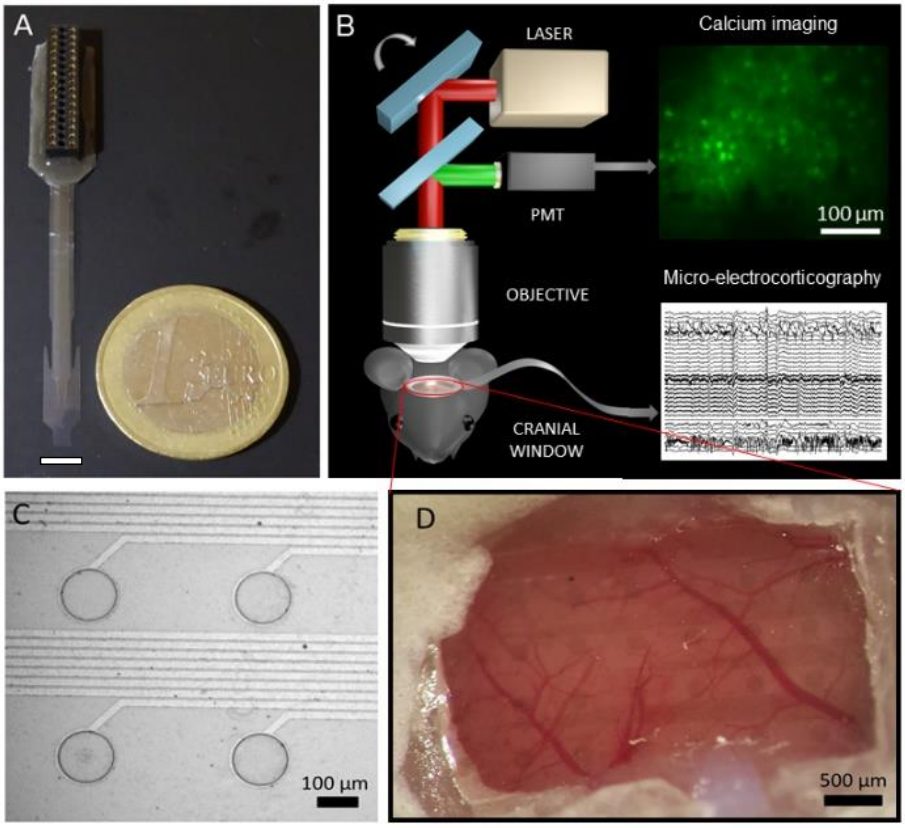

Figure 1. Introduction of the Parylene HT ITO based microECOG device. (A) Perspective view of the transparent microECoG device. Scale bar is 5 mm. (B) Schematic figure representing the experimental design for simultaneous Ca^{2+} imaging and

electrophysiology *in vivo* using our transparent microECoG device. (C) Camera image of four recording sites and conductive wires made of sputter-deposited ITO. (D) Epidurally implanted transparent microECoG array prepared for two-photon imaging in freely moving mouse.

In detail, a double side polished silicon wafer was immersed to 1:20 hydrofluoric acid solution for 30 seconds. Using a releasing agent, Parylene HT dimer was vaporized at 150 °C under vacuum into a dimeric gas form, then pyrolyzed (690°C, 0.5 torr) to cleave the dimer to its monomeric form. The monomeric gas was then deposited at room temperature on the silicon wafer to form an 8 µm thick transparent polymer layer. A lift-off pattern for the conductive layer was created with Ti35 Image reversal resist (Microchemicals GmbH, Germany). The photoresist was spin-coated at 4000 rpm for 45 seconds, then baked at 100 °C for 2 minutes on a hotplate. A Karl Süss MA6 Mask Aligner (Suss Microtec Ag, Germany) was used for UV light exposure (200 mJ/cm^2), followed by a relaxation time of 10 minutes, a reversal bake at 130°C for 2 minutes on a hotplate, and a second UV exposure (500 mJ/cm^2). In order to improve the adhesion between the polymer and the metal oxide layer, oxygen plasma strip was used before ITO deposition for 30 s (80 W) (Diener Pico, PCCE, RFG 13.56/300, Diener electronic GmbH + Co. KG) (Figure 2 A).

Indium-tin-oxide was deposited in a Leybold - Heraeus Z550 RF sputtering equipment (Leybold GmbH, Germany). Ar gas flow rate was 50 sccm (standard cubic centimeters per minute) and radio frequency power to form the plasma was 300 W. After ITO deposition, wafers were left in the acetone bath until the lift-off was completed (Figure 2 B).

An adhesion promoter was applied to support the encapsulation of the second layer of 8 µm thick Parylene HT. A 100 nm thick aluminum thin film serving as a hard mask for Deep Reactive Ion Etching was then deposited at 2 nm/minutes with an e-beam evaporator (ATC 1800-HY, AJA International, Inc., USA). A thin layer of photoresist (Microposit 1818, Rohm and Haas Company, USA) was spin coated on top of the hard mask to form the photolithographic pattern, soft baked at 115 °C for 90 seconds on a hotplate and then exposed to UV light (100 mJ/cm^2). The photolithographic pattern was developed, then hard-baked at 110 °C for 30 minutes in a convection oven (Figure 2 C).

Aluminum was wet-etched in a solution of phosphoric acid, acetic acid and nitric acid (H2O:H3PO4:CH3COOH:HNO3 = 2:16:1:1). The exposed Parylene HT surfaces were removed in high-density inductively coupled O_2 plasma in a Deep RIE System (Plasmalab 100, Oxford Instruments, UK) at 1000 W power (0.7 mm/min etching speed). The aluminum masking layer was then removed in 0.025 M NaOH solution at room temperature (Figure 2 D).

After soaking the wafers in distilled water for 2 weeks, arrays were released from the silicon surface. Arrays were mounted on a 32 channel PreciDiP electrical connector (Preci-dip SA, Switzerland) with a two - component conductive epoxy material (CW2400, Chemtronics, Georgia, US). The backside of the connector pins were protected by a two - component adhesive epoxy paste (Araldite 2014-1, Huntsman Advanced Materials GmbH, Switzerland).

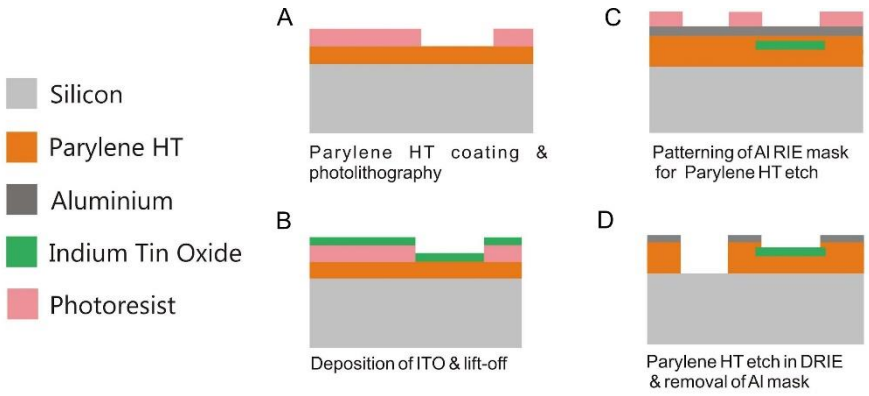

Figure 2. Schematic process of the Parylene HT / ITO device fabrication. (A) Deposition of Parylene HT on the silicon wafer as monomeric gas, lift-off pattern creation, spin coating of a photoresist layer, UV exposure, oxygen plasma stripping. (B) ITO deposition with sputtering. (C) aluminum thin film deposition, spin coating of photoresist, photolithographic pattern development. (D) Wet-etching of aluminum, reactive ion etching of exposed Parylene HZ surfaces, removal of aluminum masking layer.

3.2. Fabrication of Thiol-ene/acrylate / SIROF devices

In overview, the Thiol-ene/acrylate based device holds 31 symmetrically arranged recording sites in a 2.4 mm wide and 3 mm long area (Figure 3 A, B). The first and

seventh rows of the array had three recording sites each, while the five rows in between had five sites each, all equally distant from neighboring sites. Site diameter was 115 µm and inter-site distance was 400 µm. The composite device is 18 µm thick in areas with conductive traces and 14 µm thick in other areas with only substrate (Figure 3 C). Microfabrication was carried out at Qualia Labs, Inc., based on a micromachining scheme for Thiol-ene/acrylate based intracortical probes published earlier [Zátonyi 2018, Zátonyi 2019].

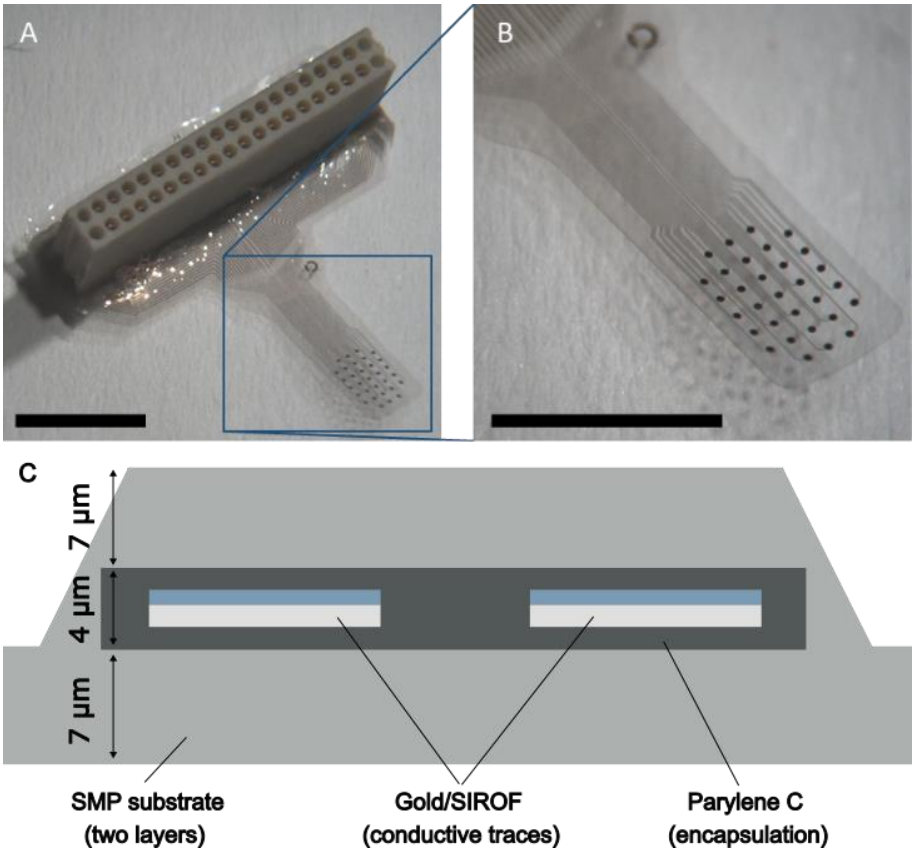

Figure 3. (A) Photograph of the finished device. Scale bar is 5 mm. (B) Magnified view of the contact points. Scale bar is 5 mm. (C) A schematic (not to scale) presenting a cross-sectional view of the layer composition of the device.

Briefly, a 7 µm thick Thiol-ene/acrylate layer was spin coated on a silicon handle wafer, and then coated with a 2 µm thick Parylene C layer. Gold conductive traces (400 nm) were then photolithographically patterned on top, and encapsulated with another 2 µm thick Parylene C and 7 µm thick Thiol-ene/acrylate layer. Recording sites and bonding

pads were then exposed with reactive ion etching in oxygen plasma, and an additional 300 nm thick sputtered iridium oxide (SIROF) layer was patterned on top of the exposed gold recording sites. On some devices, SIROF deposition was omitted ('gold-only' devices). The devices were released from the silicon handle wafer with tweezers after immersion in distilled water and mounted on a through-hole Omnetics connector (A79022-001, Omnetics Connector Corp., USA). Interconnection between the integrated conductive traces and the connector pins was created with a two-component conductive epoxy (CW2400, Chemtronics, USA), dried at room temperature for 24 h. To isolate the through-hole joints, a final layer of Araldite 1401 adhesive (Huntsman Advanced Materials, TX, USA) was applied and cross-linked without using any thermal annealing processes.

3.3. Electrochemical characterization

Electrochemical characterization of the devices was performed with a Gamry Reference 600+ Potentiostat (Gamry Instruments, Warminster, PA, US) at 25 mV root mean square. Measurements were conducted in a Faraday-cage. Impedance was measured at 1, 10, 100, 1000 and 10000 Hz in a three compartment electrochemical cell which consisted of a leakless miniature Ag/AgCl electrode as reference (ET072-1, eDAQ Pty Ltd., Australia), a platinum wire as a counter and the recording sites as working electrodes. The electrolyte was a 0.01 M phosphate buffered saline (PBS) solution (P4417, tablet diluted in 200 mL distilled water, pH 7.4, Merck KGaA, Germany). Recording sites were measured one by one to create bode plots of impedance magnitude and phase angle versus frequency, immediately after submersion in the electrolyte and thereafter on a daily basis. An equivalent circuit model was constructed in the Impedance Model Editor using Gamry Echem Analyst software. A Randles circuit (Figure 4) was constructed by a constant phase element (CPE) to model imperfect or leaky double layer capacitors with a charge transfer resistance or polarization resistance, RCT, in parallel. In series with RP is a Warburg element (WD), representing the diffusion of ions to the electrode surface. The circuit is connected in series with RS, the resistance of the bulk electrolytic solution combined with internal resistance. The CCPE is modeled using two terms: Y, the coefficient of CPE capacitance per unit length and α, a parameter defined by the phase

angle of the CPE. α has values between 0 and 1, where α = 1 represents an ideal capacitor with a phase angle of 90°, and is proportional to surface roughness and charge uniformity [Jorcin 2006].

The Parylene HT / ITO device was subjected to an accelerated aging test and measured for 4 days at 67 °C, to simulate the degradation mechanism of the electrode material and demonstrate device reliability and long-term stability in harsher than physiological conditions. Increasing the temperature by about 10 °C roughly doubles the rate of many polymer reactions [Hukins 2008]. This empirical observation can be described by the following equation:

$$T_{sim} = T_{exp} \cdot Q_{10}^{\frac{\Delta T}{10}}$$

where Q_{10} is the aging factor for 10 °C increase or decrease in temperature, and it equals two and $\Delta T = T - T_{ref}$ where T_{ref} is the body temperature (37 °C). Thiol-ene/acrylate devices were measured for 16 days at room temperature. To obtain better curve fitting, the common Randles circuit was extended with a capacitive parameter (Figure 4), which represented the porous surface of SIROF electrodes.

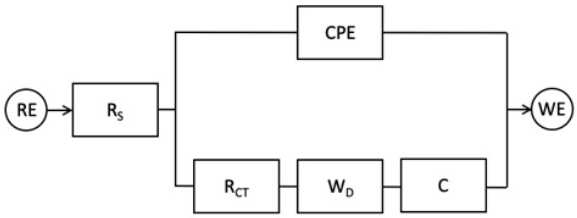

Figure 4. The Randles equivalent circuit applied on EIS data. RS: resistance of the bulk electrolyte combined with the internal resistance of the electrode. CPE: constant phase element of the double layer capacitance (CPE) featuring the interface between solid and ionic solution due to charge separation. The CPE is modeled using two terms: Y, the coefficient of CPE capacitance per unit length and α, a parameter defined by the phase angle of the CPE. RCT: charge-transfer resistance (RCT), refers to the resistance of the electrode-electrolyte interface. WD: Warburg element representing the diffusion of ions into the porous electrode surface. C: capacitive parameter, represents the porous surface of SIROF

3.4. Mechanical stability

To demonstrate the robustness of the Parylene HT / ITO device, a custom-designed bending tester based on a stepper-motor and an Arduino control board was built and applied to evaluate electrical resistance at various bending angles. Data acquisition and hardware operation were controlled with custom LabView code. The samples (Figure 5 B, C) were mounted on a frame, which translated the motion through a stepping motor and bent the middle of the samples around a cylinder with a diameter of 1 mm (Figure 5 A). Four-wire resistance measurements were used to monitor the change in resistance at 0, 45, 90, 135 and 180 degree positions. Altogether, results on five samples were analyzed through 100 bending cycles.

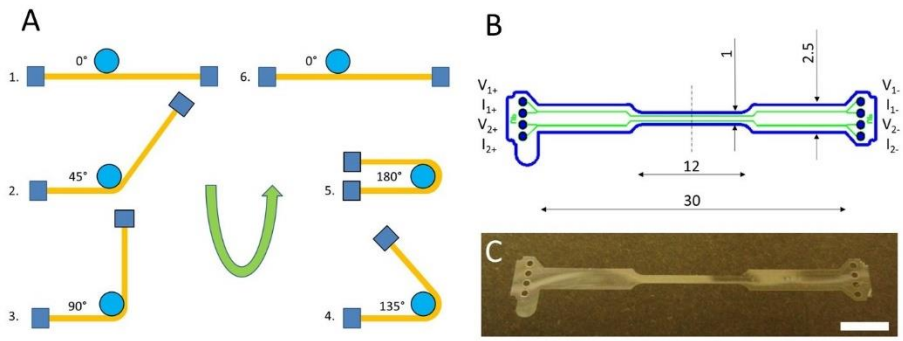

Figure 5. (A) Schematic steps of the cyclic bending tests. (B) Dimensions (in mm) and (C) representative photo of a dummy device with the same layer structure for mechanical analysis.

3.5. Transmittance and autofluorescence

The optical transmission of Parylene HT and Parylene C substrates were determined using a Cary 17 type, double beam UV-VIS-NIR absorption spectrophotometer (Varian). A xenon flash lamp was used as a light source. The beam that reflected from a monochromator alternately reached the sample and the reference. The beams (contact area: 8 mm diameter) from the sample and reference alternately registered on the photomultiplier detectors, measuring the transmittance. The selected wavelength range was 400-980 nm, considering the excitation wavelength of GCaMP in two-photon

imaging (900-910 nm excitation). Transmittance values were acquired on the raw substrates of equal thickness (16 μm). Auto-fluorescence intensity measurements were also conducted to test the Parylene HT/ITO materials attenuation at an emitted light wavelength of 512 nm. Autofluorescence characteristics were determined with Jobin−Yvon IBH FL-322 Fluorolog 3 spectrometer (Horiba Ltd, Japan) at room temperature, equipped with 450 W xenon arc lamp, double-grating excitation (260-600 nm, with 10 nm step size), and emission (270-800 nm, with 2 nm step size) monochromators.

3.6. Animals

All of the procedures were in accordance with the Hungarian Act of Animal Care and Experimentation (2013, (II.14), section 40/2013) and approved by the Animal Care and Use Committee of the Government Office (PE/EA/674-5/2019, PE/EA/776-5/2021, PE/EA/00749-6/2024). Mice were sourced from the Medical Gene Technology Unit of HUN-REN Institute of Experimental Medicine. Mice were housed in a temperature-controlled environment (24±1 °C) on a 12 h reverse light cycle (dark period between 08:00 and 20:00) and humidity between 40 and 70% and were kept in small groups (2–4 mice/homecage) in enriched environments with cardboard rolls, rotary discs, and extra nesting material (sizzle pet). Mice had ad-libitum access to food and water.

For in vitro experiments, transgenic mice expressing GCaMP6f under the thy1 promoter (FVB.129*p2 - Pde6b + Tyr c-ch* : Tg (*Thy1 - Gcamp6f*) / EMGTU) were used (Parylene HT / ITO: either sex, 12-15 weeks old; Thiol-ene / acrylate: 3 male mice. For in vivo experiments with Parylene HT / ITO devices, 8-12 weeks old wild type FVB/Ant mice of either sex were used.

For cortical in vivo experiments with Thiol-ene / acrylate devices, 6 adult, wild type C57BL6/J male mice were used. 3 mice were used for electrical characterization and immunohistology and 3 for chronic two-photon imaging. For hippocampal in vivo experiments with Thiol-ene/acrylate devices, 4 male and 3 female FVB/Ant mice expressing GCaMP6f under the thy1 promoter (FVB.129*p2 - Pde6b + Tyr c-ch* : Tg (*Thy1 - Gcamp6f*) / EMGTU) were used were used.

3.7. Acute brain slices

Mice were deeply anesthetized with isoflurane and decapitated. The brain was quickly excised and put into an intermediate ice-cold solution containing (in mM): 2.8 KCl, 1 $MgCl_2$, 2 $MgSO_4$, 1.25 NaH_2PO_4, 1 $CaCl_2$, 10 D-glucose, 26 $NaHCO_3$ and 206 sucrose. 350 µm thick horizontal slices of the hippocampus were prepared with a vibratome (Leica VT1000S) and stored at room temperature in artificial cerebrospinal fluid (aCSF) containing (in mM): 126 NaCl, 2.5 KCl, 2 $CaCl_2$, 2 $MgCl_2$, 1.25 NaH_2PO_2, 26 $NaHCO_3$ and 10 glucose and perfused with carbogen gas. Slices were then transferred to a recording chamber with continuous aCSF flow and carbogen gas perfusion for two-photon imaging.

3.8. Anesthesia

During cortical microinjection of AAV vectors and device implantation surgery, mice were anesthetized with fentanyl (0.05 mg/kg), medetomidine (0.5 mg/kg), midazolam (5 mg/kg) i.p. and ropivacaine (5 mg/kg, subcutaneously) was used for local analgesia. After surgery, revertor (2.5 mg/kg), flumazenil (0.5 mg/kg) and nexodal (1.2 mg/kg) were administered i.p. to wake the mice, as well as melosolute (0.2 mg/kg) for analgesia and Ringer's solution for hydration. Mice were let to rest for 3 - 5 days after procedures involving anesthesia

3.9. AAV injection

Following anesthesia, eye ointment (Opticorn A) was applied, and the surgical area was disinfected with Betadine. The skin on the head was opened, and two 0.3 mm diameter holes were drilled in the skull over the left hemisphere. The vector solution (0.3 µl / injection) was injected into the cortex at 30 nl / min using a glass pipette with a beveled tip. After injection, the pipette was left in place for 3-5 minutes to prevent backflow. The skin was then closed with sutures and anesthesia antidotes were administered.
For Parylene HT / ITO devices, injection coordinates were (AP, ML, DV in mm): 1) −3.2, −2.3, −0.35. 2) −3.1, −1.4, −0.35. For in vivo two-photon imaging, GCaMP6f was

expressed under the Syn promoter (titer: 1.50 × 10^12), which was prepared in-house from plasmids. The plasmid pAAV.Syn.GCaMP6f.WPRE.SV40 was a gift from The Genetically Encoded Neuronal Indicator and Effector Project (GENIE) & Douglas Kim (Addgene plasmid #100837; http://n2t.net/addgene: 100837; RRID: Addgene_100837). For Thiol-ene/acrylate devices, the vector AAV1 - mDlx - GCaMP6f was injected at coordinates (AP, ML, DV in mm): 1) −1.6, −2.0, −0.35. 2) −2.4, −2.0, −0.35.

3.10. Surgery

Following anesthesia, eye ointment (Opticorn A) was applied, and the surgical area was disinfected with Betadine. Skin on the top of the skull was removed and the underlying bone was cleaned with 3% H_2O_2. The boundary of a rectangular craniotomy enclosing the viral injections was marked and drilled with a 0.3 mm burr bit (1AU, Busch & CO). On the edge where the device would exit the craniotomy, a bone ramp was formed for smoother placement. Once the bone flap was removed, sterile tampons (Gelita, BBraun) soaked in Ringer's solution were used for constant hydration. The device was placed on the brain surface and covered with two custom-sized 0.15 mm thick rectangular glass coverslips. The inner one fit into, while the outer one overlapped with the edge of the craniotomy. The glass coverslips were glued to the bone with a mix of dental cement (ESPE RelyX, 3M) and cyanoacrylate glue, holding the device on the brain surface and sealing the craniotomy. After curing, the connector was fixed to the skull in a separate step, and exposed parts of the substrate were also covered with glue. An epidural reference electrode was implanted over the left side of the cerebellum. Finally, a steel headbar was fixed to the skull anterior to the craniotomy with dental adhesive (Super-Bond C&B). Specific to Parylene HT / ITO devices, the craniotomy was ≈3-by-4 mm, fit to the corner defined by the midline and the lambda sutures. After the craniotomy, a thin steel plate was bonded to the skull over the right hemisphere to provide stability for the electrical connector, which was then bonded to the plate with dental cement and cyanoacrylate glue (Figure 6, Figure 1 D). Specific to Thiol-ene/acrylate / SIROF devices, the craniotomy was ≈ 2.5 by 3.2 - 3.8 mm, with the sagittal suture and one of the short edges enclosing an angle of ≈27° and the two vertices of this short edge positioned

against the sagittal and lambdoid sutures. The two glass coverslips were joined by optical adhesive (NOA71, Norland) in advance (Figure 7 A, B).

In case of hippocampal implantation of Thiol-ene / acrylate devices, Dexamethasone (Baxter Healthcare Corp., 0.2 mg/kg) and Baytril (Bayer, 200 µl/10 g bodyweight) were administered subcutaneously to reduce brain edema and local tissue inflammation. A 3 mm circular craniotomy was made above the hippocampus using a dental drill, with a small extension towards the lambda suture, where the device would exit the craniotomy. The cortex overlying the hippocampus was carefully removed by aspiration (Aspiret, National Industrial Corporation) and the vessels were sealed with a bipolar coagulator (Diatrom 80, Fazzini). The device was then gently placed onto the hippocampal surface and held in place with a deep brain adapter (Judák 2022). Cylinders were hand selected to best fit the particular animal. On one end of the cylinders, a 4 mm diameter round coverslip (Glaswarenfabrik Karl Hecht GmbH & Co KG) was glued eccentrically with UV curable adhesive (NOA71, Norland). This eccentric positioning left space for guiding the flexible part of the electrode on the side of the craniotomy out to the skull surface. The Omnetics connector of the device was then positioned to the contralateral side of the head. A reference electrode and headbar was also installed as mentioned above. The Omnetics connector was then fixed to the skull tilted at an angle of ~ 45° to leave the required space for the two-photon imaging objective. (Figure 7 C, D).

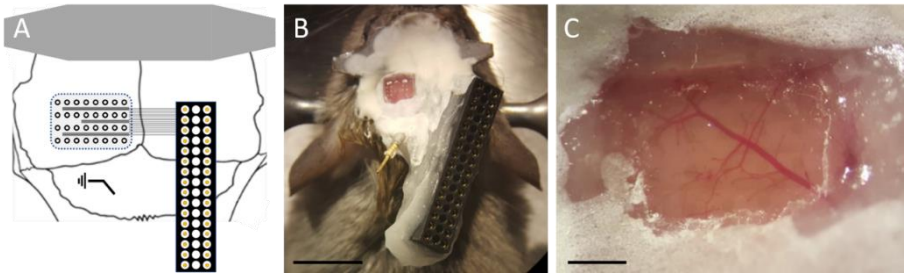

Figure 6. Parylene HT device and implantation. (A) Schematics of the surgical arrangement (not to scale). (B) Arrangement of the implanted Parylene HT / ITO device. Scale bar is 5 mm. (C) Close view of the cranial window with the implanted device above the dura mater relative to vascularization. Scale bar is 500 µm.

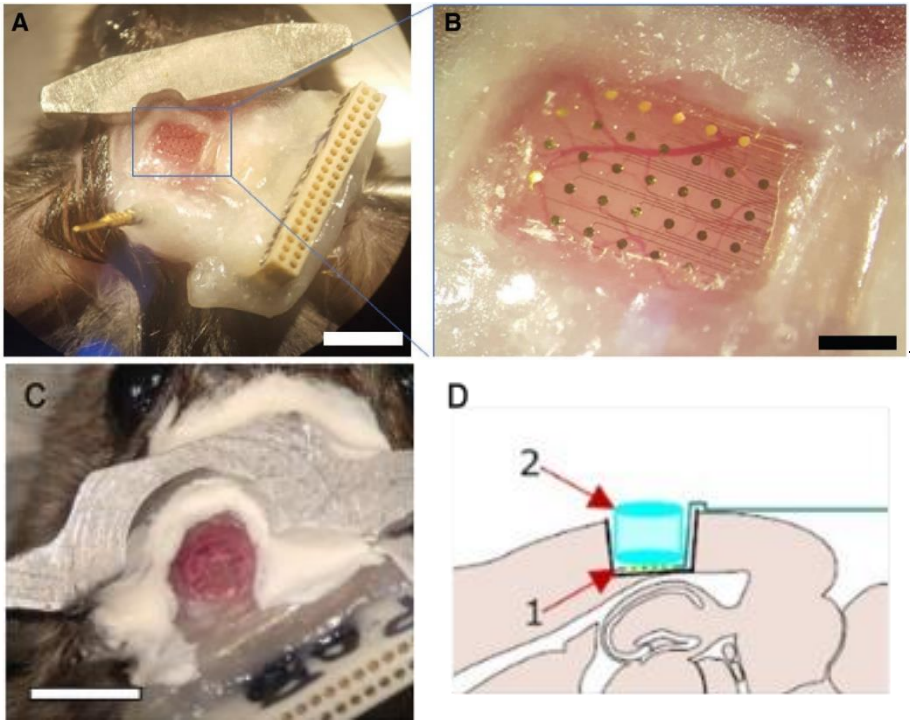

Figure 7. (A) Surgical arrangement of the cortically implanted Thiol-ene/acrylate / SIROF device on the top of the cortical surface. Scale bar is 5 mm (B) Position of SIROF recording sites compared to cortical vascularization. Scale bar is 1 mm. (C) Surgical arrangement of the hippocampally implanted device. Scale bar is 4 mm. (D) Schematic figure of the implantation. The device is placed on the hippocampal surface. 1: recording sites of the implanted device, 2: silicone cylinder (deep brain adapter).

3.11. Immunohistology

Mice were deeply anesthetized with isoflurane (Isoflurane, 0.5–1%, Forane, Abbott) and transcardially perfused with 4% (w/v) PFA for 20 minutes. After perfusion, the implanted device was detached, the brain was removed and postfixed in 4% PFA until sectioning. Brain blocks were cut into coronal sections (40 µm, cryo) on a sliding microtome (Leica SM2010 R) and stored in 24-well plates in 1% PBS with 0.3% Sodium Azide. Sections were immersed in 30% sucrose solution (in PBS) at 4 °C at least overnight or until the tissue was completely saturated. Free-floating sections were washed 3 times for 10 min with 1X PBS, then blocked for an hour at room temperature in a blocking buffer (5% Bovine Serum Albumin and Goat Serum (Thermo Scientific) containing 0.5% Triton-X

(Sigma) for membrane permeabilization). After blocking and following 3 subsequent 10-min washing steps, first with 0.3% Triton-X then with 1% PBS, GFAP primary antibody (1:2500, chicken anti-GFAP, #PA1-10004, Invitrogen) was applied directly. Slices were kept at 4°C overnight before additional 3 subsequent 10 min washing steps and the application of the species-specific secondary antibody (1:200, goat anti-chicken Alexa Fluor 647, #A-21449, Invitrogen). In addition to the secondary antibody, green fluorescent Nissl stain (1:400, NeuroTrace, #N21480, Invitrogen) was applied to the tissue sections for 2 h at room temperature. Unbound secondary antibodies were then washed off with 1X PBS (3×10 min). Sections were mounted using Fluoromount-G mounting medium containing DAPI (#00–4,959-52, Invitrogen) to co-label total cell nuclei. The slides were stored at 4°C in darkness until immunofluorescent imaging was performed. Fluorescent images were acquired using a Slide Scanner (Pannoramic MIDI II, 3DHISTECH) equipped with a 20X objective under blue (DAPI filter), green (FITC filter) and far red (Cy5 filter) illumination. The digital images were processed in CaseViewer (3DHISTECH) and were exported at 300 dpi in TIFF file format. Histological slices that were determined to originate from the implantation area by comparison of surgical coordinates and the slices' position from bregma according to The Mouse Brain atlas were included in the analysis (Franklin 2013).

3.12. Immunohistological analysis

3.12.1. Cortical Parylene HT / ITO implantations

Animals were arranged into three groups for analysis according to the duration of implantation (M1, M2-4, M5) and 16–18 contiguous slices were quantified from each animal (Table 1). Rectangular regions of interest (ROI) were then manually drawn on cortical areas that were under the implanted device and mirrored contralateral areas. Superficial (layers I-IV) and deep (layers V-VI) layers were distinguished with separate ROIs for separate analysis of upper and lower layers. Raw fluorescence intensity values of every pixel in a ROI were averaged and then normalized to the ROI area (mean intensity / mm^2) using MATLAB (Mathworks). Neuronal density was calculated on images of NeuroTrace stained slices. Cells were counted using the ITCN plugin of ImageJ

(NIH). Cells in superficial and deep ROIs were summed and normalized to the summed area of both ROIs (cells / μm^2) for comparison between implanted and control sides. Cortical thickness was measured in CaseViewer (3DHISTECH). Lines matching the inclination of the brain surface at the position of the ROIs were drawn on the slices, and cortical thickness was measured perpendicular to these lines with the distance measurement tool of CaseViewer. Statistical evaluation was performed in Prism 6.0 (GraphPad). Data groups selected for comparison were tested to be normally distributed with the D'Agostino & Pearson test, Anderson-Darling test, Shapiro–Wilk test and Kolmogorov–Smirnov test. If any of these four tests reported the groups to be normally distributed, a paired t-test was used, otherwise, a Wilcoxon matched-pairs signed rank test was used. Every test was two-tailed with Type I error rate of 0.05. Data is presented as mean ± standard deviation, whiskers of box plots show minimum and maximum values within Q1−1.5 × IQR and Q3 + 1.5 × IQR, respectively, data points outside of this range are considered to be outliers.

3.12.2. Cortical Thiol-ene / acrylate implantations

In vitro immunohistochemical labeling was carried out post mortem, 80 days after implantation on average, in three mice. Bilateral cortical areas were annotated in a manner that the marked regions were both rectangular, 500 × 500 μm and placed at the same distance from the midline at the border of layers IV and V, so that they would be the exact reflections of each other. As reference for cortical layer distinction [Matelli 1991], nuclei of giant pyramidal cells were stained among every cell nucleus with DAPI. Sample regions of the cortex were annotated on sections covered with the implanted device both on the implantation side and the intact contralateral hemisphere, which served as primary control. Image analysis was carried out with custom code in MATLAB (Mathworks). Analysis was performed for each labeling separately. Average background intensity was calculated from a separate annotation of an imaged area with no tissue, then subtracted from the values of sample annotations. Non-negative pixel values of ROIs were then averaged. Average intensities of electrode-side and contralateral side samples of sections were then compared with Student's paired t-test. As manual cortical thickness measurements can lead to inaccuracy, a custom, MATLAB based method was used. Equal

sized annotations that were placed on the border of layers IV and V extended beyond layer I and therefore included background. The ratio of tissue and background pixels were used to compare cortical thickness between hemispheres, based on the rationale that annotations on samples with larger cortical thickness would include less background. The 95th percentile of the pixel distribution of background annotations was used as the threshold value in sample annotations.

3.12.3. Hippocampal Thiol-ene / acrylate implantations

1Immunohistochemical analysis consisted of five mice implanted with the soft transparent microECoG device combined with a silicone cylinder approximately six months after implantation and one mouse implanted only with a transcortical silicone cylinder without the device, which served as secondary control during the analysis. One mouse was excluded from immunohistochemical analysis, which died before the measurements were completed. 12 Regions of Interest (ROI) were chosen from each animal from both the implanted and non-implanted hemisphere. As the main focus of the histological analysis was to shed light to the cellular changes caused by the implantation of the device, ROIs (rectangular, 400 μm × 300 μm) were placed just below the surgical area arranged so that the CA1 pyramidal region of the hippocampus could be located in the middle of the ROI. Overall number of cells, number of cells in the CA1 pyramidal region of the hippocampus and the number of astrocytes were calculated using the QuantCenter plugin of 3DHISTECH's SlideViewer program. Significance calculations were performed using Student's t-tests (two-tailed, paired), comparing to the control hemisphere, and a two-tailed two-sample heteroscedastic Student's t-test was used for comparison with the control animal implanted without an electrode. Test results were considered significant for p-values less than 0.05.

3.14. Electrophysiology

Electrode impedance and electrophysiological data were recorded at 2 kHz (cortical recordings) or 20 kHz (hippocampal recordings) using a 32-channel recording headstage (RHD 2132) and the open source RHD2000 Evaluation system (INTAN Technologies)

in vivo. Generally, impedance was measured between 1 and 5000 Hz weekly or at 1 kHz before data recordings with the built-in feature of the recording system. The number of working channels was determined based on the regular impedance measurements, in order to filter out failed electrode sites. Acceptance criteria was chosen as <500 kΩ at 1 kHz frequency for cortical and <1 MΩ for hippocampal measurements. Above these values, electrode sites were considered nonfunctional. Impedance measurements for the electrochemical characterisation of the implanted devices were taken in a closed, sound insulated box, with no lighting.

For detection of sharp wave-ripples, cut-off frequencies were set to 150 Hz and 250 Hz and used the difference between the two Gaussian filters. Only channels with the highest ripple band LFP power and events exceeding 25 ms and 4 SD over the baseline were analyzed in a MATLAB-based program (Data Analysis Suite, https://github.com/BenceSzmola/DataAnalysisSuite). Signals were discarded when they were also present on the reference channels. The automatic detections were manually curated to exclude artifacts.

For the spike detection, the MATLAB based Kilosort3 spike sorting algorithm was used (UCL Cortical Processing laboratory), followed by manual curation of the data using the Python based Phy software (UCL Cortical Processing laboratory). The spike clusters were then categorized into multi-unit activity (MUA) and single-unit activity (SUA) based on waveform characteristics, amplitude distribution, and auto-correlogram analysis. The quality metrics used for evaluation of the spike sorting performance were calculated with the Python based Spikeinterface (Buccino 2020). To calculate the auto-correlograms and assess the signal-to-noise ratio, we utilized Spikeinterface along with custom Python and MATLAB scripts. The signal was determined as the maximum amplitude of the spike waveforms, while the noise was defined as the standard deviation of the noise present on the same channel. The MATLAB based Spikes software (UCL Cortical Processing laboratory) and custom MATLAB scripts were employed to visualize waveforms and compute parameters such as firing rate, amplitude distribution, number of spikes, and real amplitudes. In order to distinguish between the various cell types, putative pyramidal cells, narrow-waveform interneurons, and wide-waveform interneurons were classified based on two criteria: the trough-to-peak time of the waveform and the burstiness index (BI) which was calculated based on the autocorrelograms of the recorded single units.

The threshold for determining burstiness was set according to the literature [Senzai 2017]. Code for KiloSort, Phy and Spikes can be accessed here: https://github.com/orgs/cortex-lab/repositories.

3.15. Two-photon imaging

Measurements were recorded and analyzed with MES software (Femtonics) running on MATLAB 2020b (Mathworks).

In vitro two-photon imaging of Parylene HT / ITO devices was performed on a Femto2D microscope (Femtonics). Laser pulses were generated by a Mai Tai HP laser (SpectraPhysics) at 900 nm and delivered through a 20x/1.0NA objective (XLUMPLFLN-W 20x/1.0 NA, Olympus). Signals were detected by a PMT (H7422P-40-MOD, Hamamatsu) separated by a dichroic mirror (700dcxru, Chroma Technology).

In vivo two-photon imaging through cortically implanted devices was performed on a Femto2D - DualScanhead microscope (Femtonics). Laser pulses were generated by a Chameleon Ultra II laser (Coherent) at 910 nm and delivered through a 16x/0.8NA Nikon objective (CFI75 LWD, Nikon). Signals were detected by a PMT (H10770B-40, Hamamatsu) separated by a dichroic mirror (700dcxru, Chroma Technology).

During measurements, awake mice were head-fixed on a circular treadmill but were otherwise freely moving. The movement of the treadmill (running) was also recorded. Cells expressing GCaMP6f located under the microECoG device were imaged with resonant scanning at 31 Hz.

Hippocampal two-photon calcium imaging was performed with an acousto-optical microscope (FEMTO3D Atlas Plug & Play, Femtonics) equipped with an Alcor 920-4 laser (Spark Lasers), an H10770B-40 PMT (Hamamatsu) and a CFI75LWD 16 × objective (Nikon). Fluorescence emission was detected in the 490–550 nm range using a ET520/60m-2p dichroic mirror (Chroma). Calcium activity was recorded from the hippocampus under the implanted device with chessboard scanning [Szalay 2016]. ROIs were placed in regions between electrode traces and sites and recorded with chessboard scanning (63–111 Hz). Active cells were manually labeled as ROIs. Traces were filtered with a gauss kernel of 4 and ΔF was calculated as $\Delta F = F_i - F_0/F_0$ with F_0 being the gauss average of the 500 neighbouring frames for each frame. Mice were habituated to the

recording environment and to head fixation before the measurements. Training and experiments were conducted during the dark cycle of animals.

3.16. Microbead measurements

Fluorescent microbeads of 0.175 μm diameter (P7220, ThermoFisher) and 6.0 μm (F14808, ThermoFisher) were sealed between two glass coverslips and two-photon images then were recorded with and without Parylene HT / ITO devices placed on the microbeads. The Point Spread Function (PSF) was calculated as the FWHM (full width at half maximum) of the gaussian fit of the microbead intensity profile, corrected for the nominal (0.175 μm or 6.0 μm) microbead size and normalized to the average PSF size of beads measured without devices placed on them. Images were analyzed with MES (Femtonics) in MATLAB (Mathworks). Paired sample t-test was used to compare bead sizes (n=10).

In case of Thiol-ene / acrylate devices, only 6 μm diameter beads were measured. The same microbeads were imaged with and without the device on top. A custom bead detection and size calculation algorithm based on the Circle Hough Transform [Atherton 1999] was used. The uncertainty of the bead edge was overcome with thresholding (MATLAB function *im2bw* with level value 0.005). The diameters of the beads were compared with Student's paired t-test with 0.05 α value with OriginPro.

3.17. Photodegradation and photoelectric artefacts

Laser power was increased step by step (range: 7.7 − 132.4 mW) while recording with the electrode, to characterize photoelectric artefacts of scanning and to determine the maximum laser power to use with the electrode. Parylene HT/ITO devices were immersed into Ringer's solution and imaged with both galvanic and resonant scanning while recording with the electrodes. The exact recording sites were identified according to the layout of the device. The field of view was chosen to contain only one recording site, which was selected as a ROI in measurements of 5 seconds long temporal image stacks (155 frames).

At each laser power tested, the pixel intensity values inside the ROI were averaged for every frame, and these averages were normalized to the maximum averaged value at the lowest laser power tested with that scanning mode. Then, the quotient of the sum of these averages and the number of frames was calculated, where values closer to 1 would reflect higher similarity to the state of the recording site at the lowest tested laser power. These quotients were then visualized as a percentage of the previous quotient value, while the first one (of the lowest tested laser power) was not fractioned. The safe-to-use light intensity limit was determined by evident damage to the contact site on the recordings as the settings of the last image not to cause visible photodegradation. The standard deviation of the frame averages was also calculated, and evident damage were reflected by the average SD increasing above 1.

In galvanic mode, we varied laser power between 9.6 mW and 34 mW and Z-level between 0 μm and −30 μm relative to the device surface. For galvanic scanning, all images were 500 × 500 pixels in size (pixel size is 0.95 μm), acquired at 2.11 Hz frame rate (10 frames) at every focal plane and laser power used. In resonant mode, we used a laser power between 7.7 mW and 132.4 mW and Z-level between 0 μm and −30 μm. For resonant scanning, all images were 512 × 512 pixels, 0.88 μm pixel size, acquired at 30.98 Hz frame rate (155 frames) at every focal plane and laser power used. Photoelectric artefacts were evaluated in the frequency domain of the electrical signals recorded during the measurements of photodegradation. To quantify the contribution of the light induced artifact, the power density of noise is calculated, which represents the power distribution of noise in the frequency domain.

3.18. Neurite measurements

Two-photon images of the CA1 region of the hippocampus were recorded with and without the device on the acute slices. Sample images were chosen to measure the average diameter of neurites in a field of view. Images were analyzed with a custom MATLAB script employing gauss filtering, angle and gradient calculation, morphological operations and minor axis length measurement (MATLAB function *regionprops*).

In case of Thiol-ene/acrylate devices, images were cut to four overlapping tiles and the fluorescence values were normalized to be between 0 and 1, in order to achieve more

accurate detection. These tiles were segmented differently based on their average intensity. If the mean intensity of the tile was larger than 0.1, adaptive thresholding was used with a sensitivity value of 0.1. Otherwise, a global threshold was used, based on Otsu's method [Huang 2009]. The tiles were structured with morphological operations (MATLAB functions *bwareafilt*, *strel*, *imopen*, *imclose*) for neurite detection. After this, a watershed algorithm was used to separate the detected objects. Neurites were detected automatically by determining the circularity of detected objects, which was determined by using the circularity field of the *regionprops* function. A detected object was determined as neurite if this metric was lower than the threshold level (0.1). After the detection, the detected objects from the tiles were mapped to their original coordinate on the image, and duplicates were filtered out. The statistical comparison was performed on the neurite diameter (minor axis length) with Student's two-sample t-test with 0.05 α value with OriginPro.

3.19. Calculation of relative intensity

Time-series image stacks were averaged across time, and cell bodies on the averaged images were automatically detected, with the same algorithm used for the detection of neurites in case of Thiol-ene/acrylate devices. A detected object was determined as a cell body if the circularity was larger than the threshold (0.4). Detected cells were used as regions-of-interest to extract cellular calcium activity. Raw fluorescence of ROIs was Gauss filtered ($\sigma = 5$) and converted to relative fluorescence change as $\Delta F = F_i - F_0/F_0$, where F_0 is the mean of the lowest 12.5% data points of an individual trace, and Fi are the individual intensity values over time.

3.20. Calculation of SNR

The calculation of signal to noise ratio from electrophysiological data was performed with a custom MATLAB program. The treadmill movement was used to identify resting periods in the measurements. A 30 s long segment when mice remained immobile was selected from every measurement. The SNR was calculated based on the work of Lecomte et al. [Lecomte 2017] as SNR = A / 2 * SDnoise, where A is the peak-to-peak value of

the filtered data. The noise was derived from the difference between the raw data and the filtered data, and its standard deviation was calculated to determine the SNR. Raw data was filtered with either a 1 Hz high pass filter (fourth order Chebyshev filter with 30 dB attenuation) and a 140 Hz low pass filter (fourth order Chebyshev filter with 30 dB attenuation), or a 200 Hz low pass filter (5th order Butterworth) and a 1 Hz highpass filter (3rd order Butterworth). The noise was derived from the difference of the raw data and the filtered data, and its standard deviation was calculated to determine the SNR.

3.21. Custom code availability

The custom analysis codes that are described at different levels of detail in the thesis are made available in a common repository at github.com/mm90210/thesis.

4. Results

4.1. Characterization of the Parylene HT/ITO device

4.1.1. Electrochemical stability

In an approach where the device is chronically implanted on the brain surface, long term electrochemical stability is necessary to maintain electrophysiological signal quality and structural cohesion of the substrate layers. These in turn extend the lifetime of the implant and increase the amount of obtainable data. We tested the long term electrochemical stability of Parylene HT / ITO devices with the accelerated aging test, where devices were constantly soaked in 0.01 M PBS at 67 °C for 4 days, which simulates 24 days of soaking at 37 °C. As a way to recognize recording sites as functional or non-functional, we set up the criteria that recording sites with the impedance below 500 kΩ at the conventionally relevant 1 kHz frequency were considered as functional. Microscopic inspection of non-functional recording sites showed that failures were mainly caused by the delamination of connection points at the contact pads of PreciDip connectors. Impedance of functional channels decreased slightly from 369 ± 42 kΩ to 345 ± 130 kΩ at 1 kHz on average during the test. Results of the test are shown on Bode plots of impedance magnitude and phase angle against frequency (Figure 8 A-B, E-F). Curve fitting and equivalent circuit analysis were then applied to the measured data employing a common method based on the Randles circuit model (Figure 4, Figure 8 C). The variations in the components of the modeled equivalent circuit during aging experiments are summarized on (Figure 8 D). Resistance of the bulk electrolyte is represented as spreading resistance (RS). The fitted RS, representing the bulk electrolyte, which is independent from the active surface area of recording sites, remained in the same range (RS = 0.3 MΩ) during the aging test. The charge transfer resistance (RCT) did not change significantly, while CCPE (a) changed slightly from a capacitive to a resistive state (a = 1 for ideal capacitor; a = 0 for ideal resistor). Decrease in α suggests a possible penetration of moisture over time, resulting in a larger contact area on the electrode–electrolyte interface. Since the diffusion path length of ions was short, the constant of Warburg impedance (WD) did not vary with time.

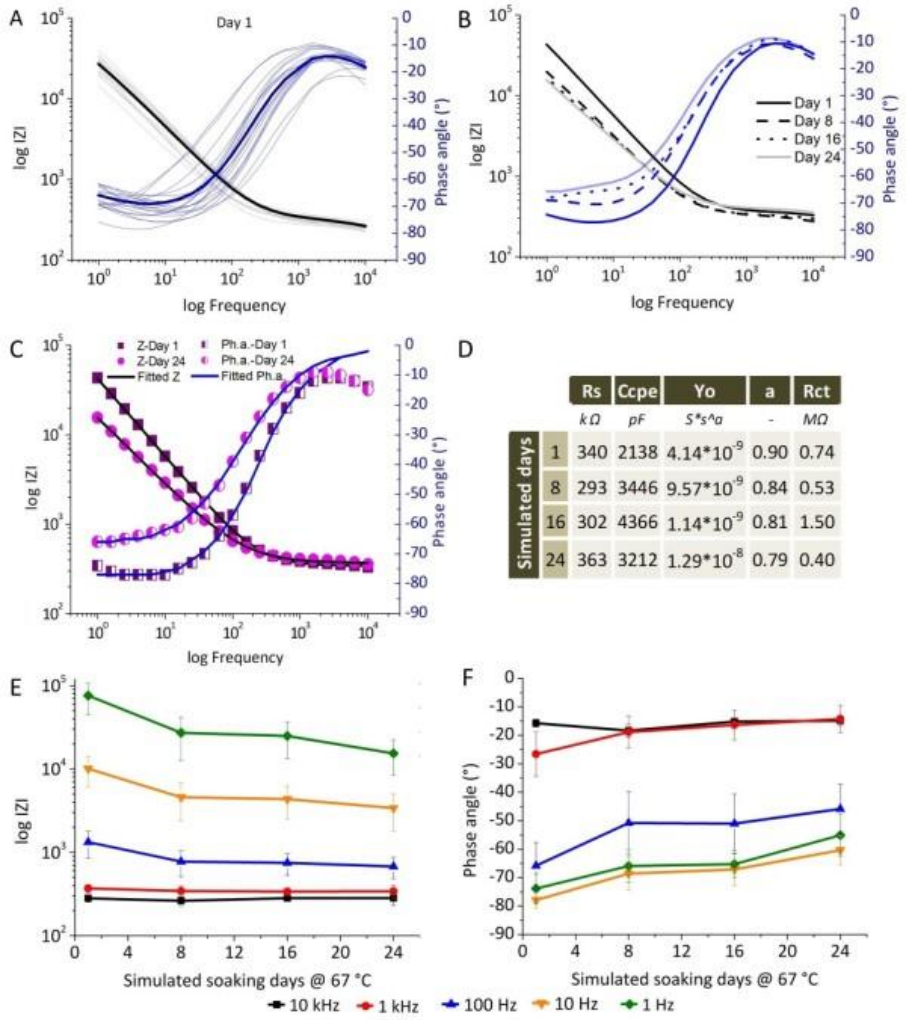

Figure 8. (A) Impedance magnitude (Z) and phase angle of 22 recording sites on the first day of the accelerated aging test. Black lines: impedance magnitude, blue lines: phase angle. Bold lines: averages, pale lines: single channels. (B) Representative Bode plot of a channel on the first 4 d of the accelerated aging test (1, 8, 16 and 24 simulated days). The color code is the same as for (A). (C). Representative Bode plot and the relevant fitted curves of a channel on the 1st and 24th simulated day. Filled symbols: impedance magnitude. Semi-filled symbols: phase angle. Squares: simulated day 1. Circles: simulated day 24. Continuous black lines: fitted impedance magnitude. Continuous blue lines: fitted phase angle. (D) Fitted equivalent circuit parameters during the accelerated aging test. Average of 22 channels. Frequency is color coded (10 kHz - black, 1 kHz - red circle, 100 Hz - blue, 10 Hz - orange, 1 Hz - green). (E) Average impedance and (F)

average phase angle of 22 sites during the accelerated aging test. Data is presented as mean ± standard deviation.

4.1.2. Mechanical stability

The device is exposed to mechanical stress during implantation, as it must be secured to the skull in a way that prevents the animal from damaging it and simultaneously allow freedom of movement between measurements. Attaching and removing connectors before and after measurements also puts repeated strain on the device. Therefore, characterization of mechanical stability is key in ensuring reliability. We characterized stability by bending dummy devices cyclically (Figure 5) and measuring and comparing wire resistance at specific angles. Changes in resistance between various angles were below 0.5 % for every compared angle, even after 100 cycles (Figure 9 A-B), suggesting that the Parylene HT/ITO device is sufficiently stable to tolerate mechanical stress during chronic experiments.

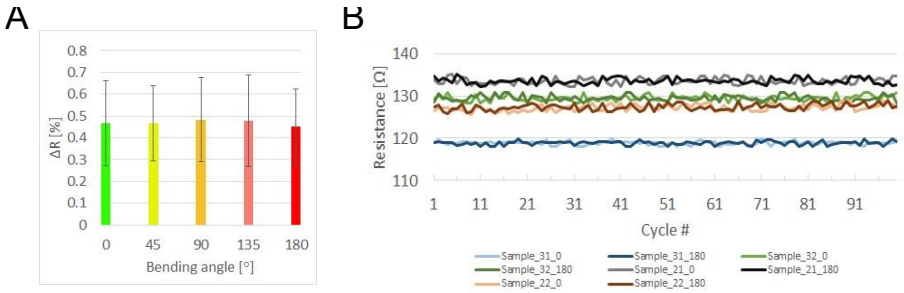

Figure 9. (A) Change in resistance (ΔR) of devices at various bending angles. (B) Resistance (Ω) of individual devices according to cycle number for angles 0° and 180°. Pale colors: 0°, bold colors: 180° (n = 4 devices).

4.1.3. Transmittance and autofluorescence

When combining surface microECoG devices with two - photon imaging, substrate materials with highly compatible optical properties are desired. Suboptimal compatibility may decrease the functionality of two - photon imaging and therefore make the device less useful in practice. From this aspect, the optimal substrate material is not refractive,

and has high transmittance and low autofluorescence in the wavelength range of both two-photon excitation and emission. We evaluated the Parylene HT substrate with autofluorescence (excitation 260–600 nm, emission 270–800 nm) and visible–near–infrared (380–980 nm) spectroscopy, together with Parylene C as a reference material, as it is frequently used in microelectrode devices. According to our measurements, Parylene HT showed lower autofluorescence intensity over the selected spectrum compared to Parylene C (Figure 10 A) and higher transmittance (~ 2% higher at 900 nm (Figure 10 B). Based on the fluorescence and transmittance spectra, Parylene HT is suitable and more preferable than Parylene C for two-photon imaging application.

4.1.4. Microbead measurements

In conjunction with the transmittance and autofluorescence tests, we speculated that imaging through the Parylene HT/ITO device may affect spatial resolution (Liu 2012). Therefore, I imaged fluorescent microbeads with a nominal diameter of 0.175 μm and 6.0 μm through the Parylene HT/ITO device and compared their size. I found that the smaller microbeads, that are below the spatial resolution, were larger in size when the ECoG device covered the bead preparation (without ECoG: 0.79 ± 0.02 μm, with ECoG: 0.95 ± 0.03 μm, $p < 0.001$, $n = 12$, Mann–Whitney U-test). This size difference was absent on larger structures, as the size of 6.0 μm microbeads were equal (without ECoG: 6.11 ± 0.05 μm, with ECoG: 6.06 ± 0.05 μm, $p > 0.05$, $n = 10$, Mann–Whitney U-test) (Figure 10 C) and the impact of imaging neurons through the implanted microECoG device was not observable in vivo (Figures 12 E, F, Figure 15 C, F).

4.1.5. Neurite size measurements

As an additional test to verify the combined use of the Parylene HT / ITO device and two-photon imaging before in vivo experiments, we compared image quality with and without the microECoG device on in vitro hippocampal slices of GCaMP6f expressing mice by measuring the size of neurites on the images. Cells in the CA1 subregion were clearly visible together with fine dendritic structures in *stratum radiatum* when slices were covered with the ECoG device (Figure 10 E, F). Our custom image processing algorithm

recognized 221 neurites on the images taken through the ECoG device and 142 neurites on the images taken without the ECoG device. The mean width of the neurites under the device was 2.17 ± 0.17 µm, while without the device, the mean size of the neurites was 1.73 ± 0.11 µm (Figure 10 D), measured 30-70 µm from the cell soma. It should be noted that the refractive index of Parylene HT (1.55) is higher than that of the surrounding medium, which may introduce a slight optical distortion to the measured dimensions in the presence of the microECoG device. Nevertheless, the fluorescent signals of the neuronal structures could be detected clearly through the transparent ECoG device (Figure 10 E, F. Figure 11).

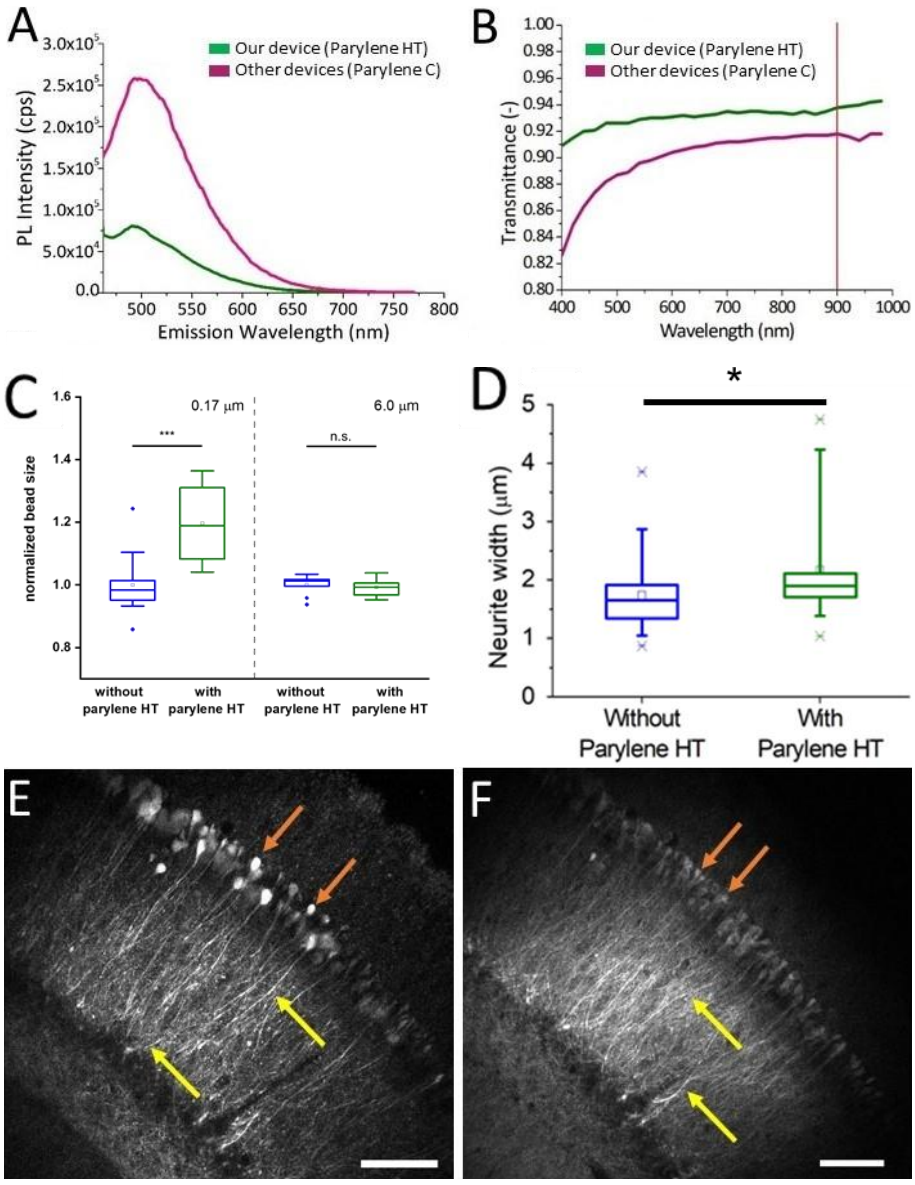

Figure 10. (A) Autofluorescence emission spectra of Parylene C (purple) and Parylene HT (green) at 510 nm excitation wavelength in counts per second (cps). (B) Transmittance spectra of Parylene C (purple) and Parylene HT (green) between 400 nm and 980 nm. Orange line denotes the wavelength of two-photon imaging. (C) Boxplots of normalized microbead size. Left: 0.175 μm microbeads. Normalized size without ECoG: 1.00 ± 0.03, with ECoG: 1.20 ± 0.04. Right: 6.0 μm diameter microbeads. Normalized size without ECoG: 1.00 ± 0.01, with ECoG: 1.00 ± 0.01. (D) Measured neurite width 30 - 70 μm from the cell soma. Boxplots indicate 25th and 75th percentiles and the mean. Whiskers extend to the most extreme data points not considered outliers. Outliers are denoted with the '+' symbol (Origin built in boxplot function). (E-F) Sample images of CA1 neurons in hippocampal slices without (E) and with the transparent ECoG device (F), using 72 mW and 22.3 mW respectively. Red and yellow arrows show cell soma and dendrites, respectively.

4.1.6. Evaluation of photodegradation

High intensity laser scanning is known to have possible adverse effects on the sample due to heating. While this is taken into consideration for living tissue, it may also have considerable effect on implanted microECoG devices. Since long-term usability is highly valued in studies using either two-photon imaging or surface microECoG devices, it is also certainly desired when the two are combined. However, devices may be fragile and vulnerable to damage caused by high laser intensity scanning, since optical considerations exclude the use of robust devices. Damage to implanted ECoG devices may limit their long-term use due to deterioration of optical and electrophysiological performance. To address this issue, I investigated the vulnerability of the device to two-photon scanning by exposing it to high laser power in Ringer's solution. Two scenarios were taken into account. In case 1) I imaged the device's surface directly, as this simulates an experimenter locating areas of interest. In this test, I varied laser power to determine any limit above which potential adverse effects might appear (Figure 13 B). In case 2) I imaged closely below the device plane, which simulates measurements inside the brain (Figure 11). By testing this, I aimed to explore whether there is a minimum necessary distance between the imaging plane and the device's plane that is advised to be kept, in

order not to damage the device. In this case, I also assumed that it is more possible to damage the device when scanning closer to it. In the first case, I imaged the array's surface while gradually increasing laser intensity until I registered visible damage to the device; while in the second case, I used laser power that was sure to damage the device when imaging on its surface, and decreased the distance from the device's surface gradually between images. I also compared two different scanning modes, galvanic and resonant scanning, for both cases. Using these approaches, I determined the laser power sufficient to damage the device under these conditions and advised limits to be used during imaging the device's surface accordingly (Figure 12, Figure 13 A). I found that two-photon scanning of the device's surface (case 1) can cause damage to the device near recording sites (Figure 13 B), with an approximately 2.5-fold difference between galvanic and resonant scanning in safe-to-use laser intensity limits (galvanic: 13 mW at Z = 0 µm, range tested: 7-19 mW; resonant: 33 mW at Z = 0 µm, range tested: 7-105 mW). Focusing below the device (case 2) increased the limits of tolerance, while the difference between scanning modes increased (galvanic: 34 mW at Z = −30 µm; resonant: 132 mW at Z = −20 µm). Exposing the device to laser intensities above these limits induced a change in the autofluorescence and transparency of the device (Figure 13 A, B), particularly around recording sites. The observed inhomogenous autofluorescence resulted in the appearance of a previously unobserved shadow under the recording site, in deeper layers of the cortex (Figure 13 C, D), hindering two-photon imaging directly under the damaged area. This effect may be caused by the local delamination of Parylene HT due to heat stress around the more vulnerable recording sites. However, as focusing below the device's surface even by 20 µm allowed for high-laser power measurements (132 mW at Z = −20 µm with resonant scanning), damage is easily avoidable when keeping to the advised laser power limits without hindering imaging or usability.

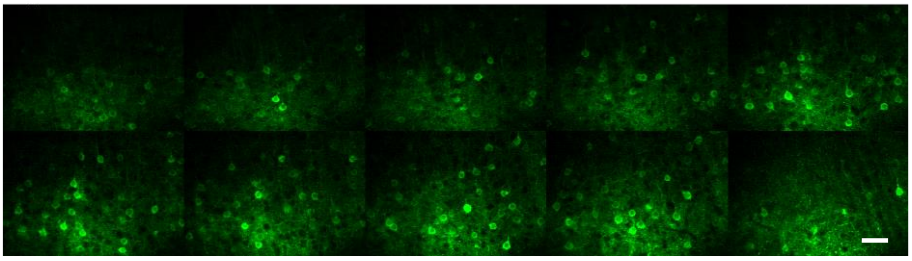

Figure 11. Z-dimensional image stack of an in vitro measurement. Images of the stack are 10 µm apart in depth (left to right, upper row: −100 µm to −60 µm, bottom row: −50 µm to −10 µm), and were imaged with the same light intensity. Scalebar is 50 µm.

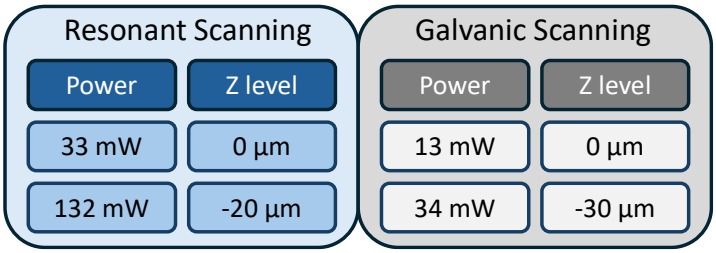

Figure 12. Safe-to-use laser power limits of different scanning modes in the two tested conditions.

4.1.7. Evaluation of photoelectric artefacts

Besides damaging the ECoG device at higher laser intensities, scanning can also induce artificial signals on the electrodes, photoelectric artefacts, which contaminate the recordings. A photoelectric artefact is an electric noise detected on the recording sites of the ECoG when the laser beam passes through the conductive layers. In the electrophysiology data, this noise is superimposed on real signals, which makes further analysis hard due to the decreased signal-to-noise ratio. Generating these artefacts may be avoided by avoiding scanning the electrodes, however this also limits the imaging field of view. Moreover, in a concurrent imaging and electrophysiology approach, such a strategy is disadvantageous. Therefore, it is important to characterize the sensitivity of the Parylene HT / ITO microECoG device to such artefacts.

Photoelectric artefacts were evaluated with two- photon microscopy using different scanning modes (galvanic and resonant), depth of focal plane with respect to the device plane (distance) and at various intensity of irradiation (laser power) in Ringer's solution with two device compositions, Parylene HT / ITO and Parylene C / Ti/Au. The characteristic patterns of photoelectric artefacts are shown on (Figure 13 E). Parylene C samples holding Ti/Au metallization were tested in galvanic scanning as a control material to compare the light-induced intensity of artefact signals. The power density of

artefact signals in the focal plane (Z = 0) of the devices was lower for ITO than for Ti/Au at the tested light intensities (Figure 13 F). Galvanic scanning evoked larger amplitude artefacts than resonant scanning (Figure 13 G) and power values below 12 mW in resonant mode did not evoke substantial photoelectric artefacts (Figure 14). Focusing below the device by Z = −5 μm in resonant (33 mW) and at Z = −10 μm in galvanic (13 mW) scanning mode under an ITO recording site apparently suppressed the power density of noise (Figure 13 H).

Based on our optical measurements focusing on the limitations of device operation, we can conclude that two- photon laser scanning close to the device plane (within 10 μm) requires special caution to avoid possible damages and light induced artefacts in the recorded signals. If the focal plane of the imaging is out of this range, the device is not particularly sensitive to the applied experimental parameters.

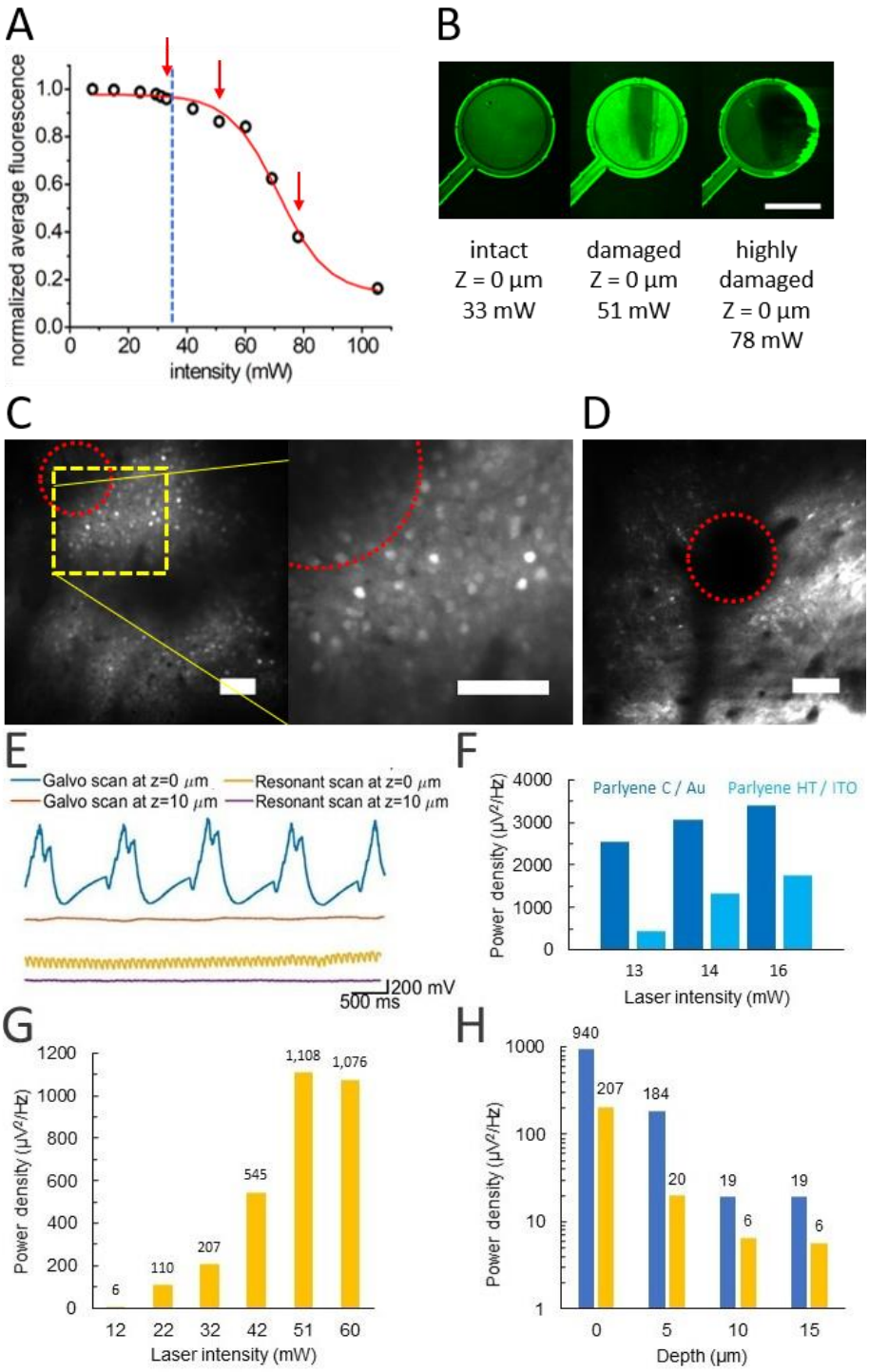

Figure 13. Effect of laser power on material degradation of the electrode. (A) Quantification of damage to the electrode by standard deviation of average fluorescence of the contact site. The dashed blue line shows the safe-to-use limit (33 mW) with resonant scanning at the device's surface. Arrows refer to the images in (B) sequentially.

(B) Resonant scan images (average of 155 frames) taken at the device's surface (Z = 0 μm) with 33 mW (left), 51 mW (middle) and 78 mW (right) laser power, respectively. Note the darkening of the recording site, indicating damage. Look-up tables are not uniform, for demonstration purposes. (C) Two-photon image of L2/3 cells (~ − 160 μm from the surface) under an intact recording site, where only GCaMP6f expression and blood vessels limit the areas suitable for imaging. Left, wide field of view image of GCaMP6f labelled cells under an implanted ECoG device. Right, magnified area inside the yellow box on the left image. The red dotted circle shows the position of a contact site on the surface. (D) The same area as in (C), after the recording site on the surface was damaged and became nontransparent. Note the shadow of the damaged recording site masking previously visible cells. (E) Representative curves on the sensitivity of signal recording to photoelectric artefacts at galvanic and resonant scanning modes measured on the device plane (Z = 0 μm) and at Z = −10 μm. (F) Comparison of the photoartefacts of Parylene C / Ti/Au devices and Parylene HT / ITO electrodes at various light intensities at the fundamental harmonic for galvanic scanning (2.11 Hz). (G) Maximum power density of noise using various light intensities on a recording site (Z = 0 μm) at the fundamental harmonic frequency of resonant mode (30.98 Hz). (H) Maximum power density of noise at different distances from the device plane. The laser was focused on the site (Z = 0 μm) and under the site at the shown depth. Laser intensities are 13 mW and 33 mW for galvanic and resonant mode, respectively.

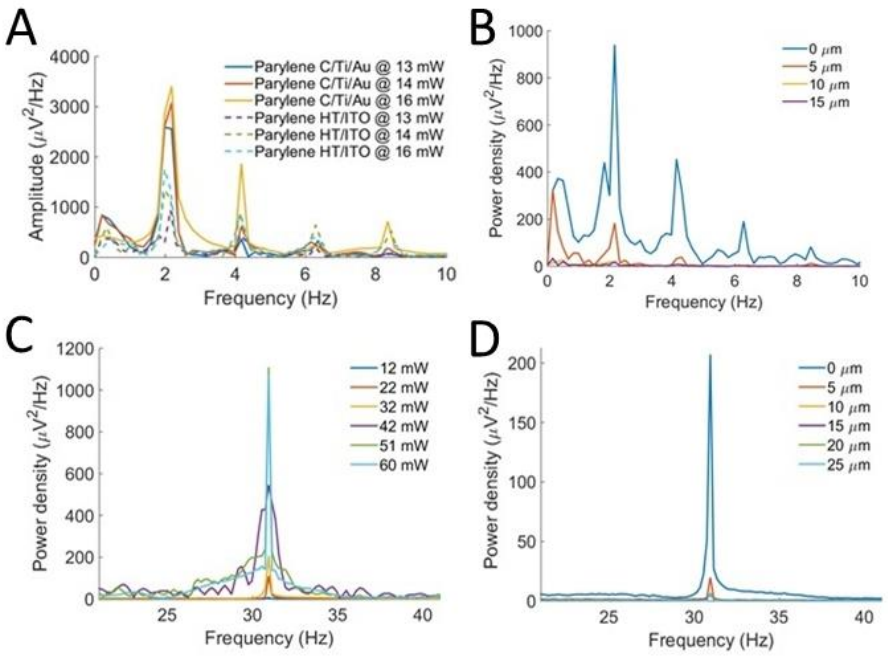

Figure 14. (A) Comparison of the light induced artefacts during galvanic scanning on Parylene C/Ti/Au devices and Parylene HT/ITO devices. (B) Galvanic scanning with 13 mW laser power at different distances from the plane of the device. (C) Resonant scanning spectrum using various laser powers at the plane of the device (Z = 0 μm). (D) Resonant scanning spectrum at different distances from the plane of the device. Scanning was focused on or below the recording site with the same 33 mW laser power.

4.1.8. In vivo two-photon calcium imaging

After extensive bench-top and in vitro tests, I sought to prove the applicability of two-photon imaging through the Parylene HT / ITO device and its usability in chronic in vivo experiments by implanting the device into GCaMP6f injected mice and imaging the spontaneous activity of V1 neurons in awake head-fixed mice. Apart from the implantation of the ECoG device, this approach is well-known and widely used in two-photon imaging studies to measure neuronal activity. The implantation of the microECoG device into the craniotomy and covering with glass coverslips did not damage either the contact sites or the wires, which allowed the detection of spontaneous electrophysiological activity (Figure 15 A). The spatial distance between the channels

increases from top to bottom, which is reflected in the growing difference in the raw traces and heatmap profiles. As contact sites and their connections cover a considerable area of the craniotomy, the high transparency of ITO is highly beneficial for two-photon imaging, since the scattering of photons would reduce the signal-to-noise ratio. The activity of neurons under recording sites was very similar to cells under the substrate (Figure 15 C, E). Neurons with varying rates and amplitude of Ca^{2+} activity were present at both locations (Figure 15 D). In one animal, more than 25 active cells were observed under recording sites during a single 3-minute long recording. Due to the different levels of GCaMP6f expression that determine the baseline fluorescence, maximal $\Delta F/F$ values were used to compare neuronal activity below recording sites and below Parylene HT only. There was no significant difference between the average maximal event amplitude (HT / ITO: 1.10 ± 0.09; HT: 1.17 ± 0.13, n=25 cells) (Figure 15 E). Representative Ca^{2+} activity of 53 individual cells are shown on (Figure 16). The clarity of neurons after 51 days remained as good as it was 17 days after implantation (Figure 15 F), suggesting that optical access is primarily unaffected by the presence of the implanted ECoG device, and more limited by reporter expression and quality of surgery. We also compared the rate of activity and the decay time of events in neurons of microECoG device implanted and unimplanted control mice, which did not reveal a significant difference (Figure 17). For this comparison, imaging data was binned to 160 ms (~5 frames) bins and a bin was determined as active if the elevation in fluorescence amplitude was at least 2 times larger than the standard deviation for the baseline period. The decay parameter was calculated by fitting the decay of Ca^{2+} events with a single or double exponential function. The number of active bins was 41.68 ± 2.68 / minute with the microECoG device and 39.38 ± 2.22 / minute without the microECoG device (n=25 each, p=0.51, two-sample t-test, mean ± SEM), while the decay parameter was 0.42 ± 0.03 $\Delta F/F_0$ /s and 0.46 ± 0.04 $\Delta F/F_0$ /s respectively (n=72 and 42 events, p=0.34, two-sample t-test, mean ± SEM). To summarize, we found that the fully transparent Parylene HT / ITO based microECoG device does not interfere with the two-photon calcium imaging of neurons and provides simultaneous multi-channel electrocorticography data of intracranial activity.

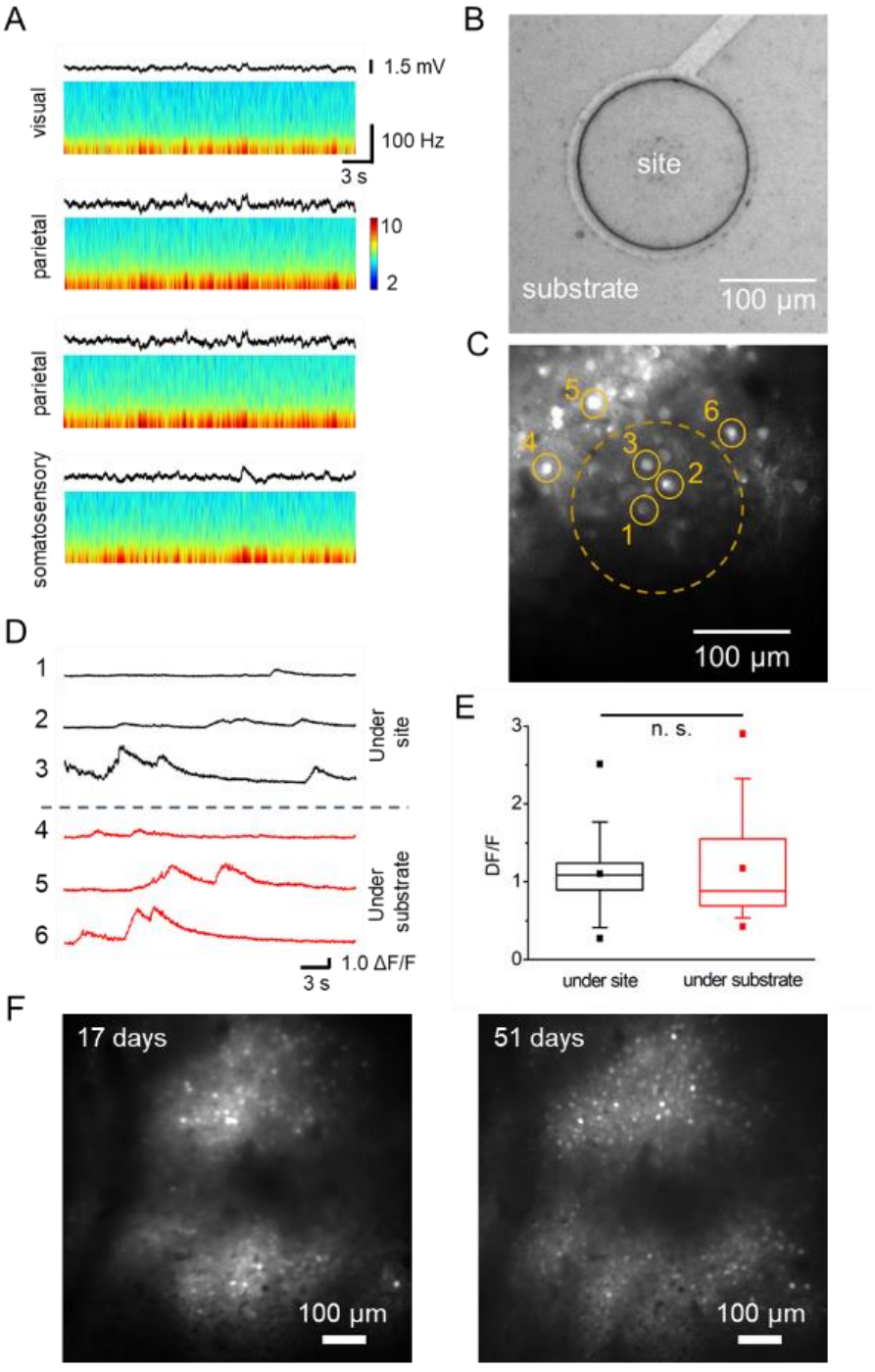

Figure 15. In vivo Ca^{2+} imaging. (A) Examples of ECoG recordings showing spontaneous activity and heatmaps of their frequency - dependent signal power. (B) Camera image of a recording site of the microECoG device. (C) Two-photon image of the same field of view as in (B), 250 µm below the surface (L2/3). GCaMP6f expressing neurons were visible under the substrate and also the recording site. Cells on (D) are denoted by solid circles. The dashed circle marks the position of the recording site in (B) on the surface.

(D) 30 s long Ca^{2+} activity of the numbered cells on (C), registered from below the substrate or the recording site. (E) Statistical comparison of peak amplitude (in $\Delta F/F_0$) produced by neurons below the recording site or the surrounding substrate (n = 25 cells, Mann–Whitney U test: $p > 0.5$). (F) Images of the entire area of viral expression in the V1 region 17 (left) and 51 (right) days after device implantation.

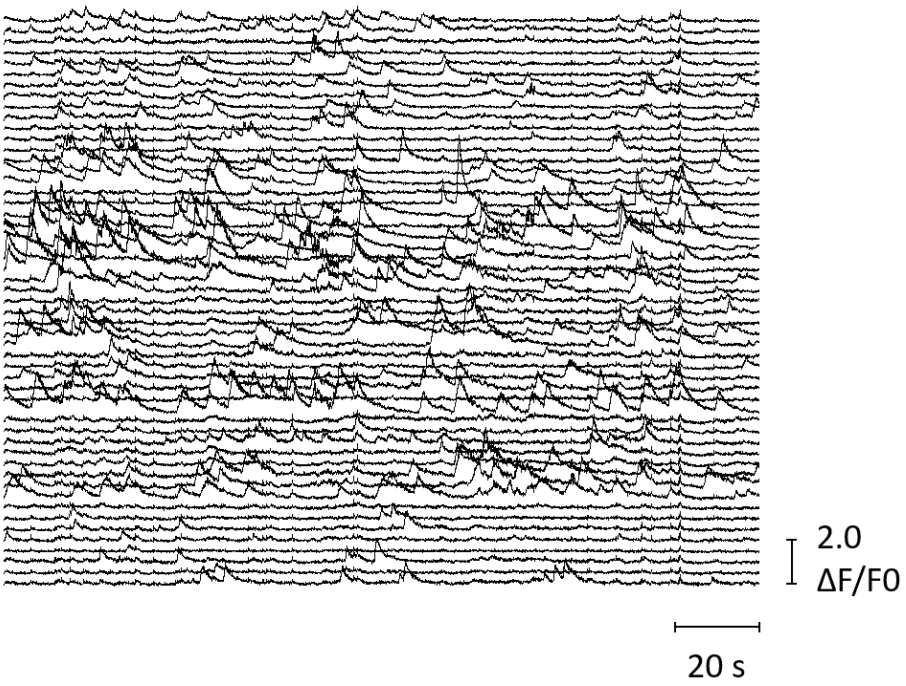

Figure 16. 180s long raw fluorescence traces of 53 individual cells measured under the microECoG device (same field of view as in Figure 15 C).

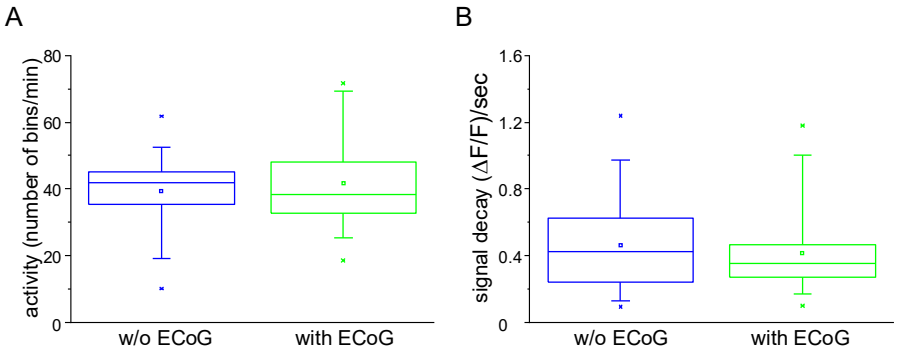

Figure 17. (A) Comparison of rate of activity and (B) decay time with and without the microECoG device. (A) The number of active bins was 41.68 ± 2.68 / minute with, and 39.38 ± 2.22 / minute without the microECoG device (n=25 each, p=0.51, two-sample t-

test, mean ± SEM). (B) The decay parameter was 0.42 ± 0.03 $\Delta F/F_0$ /s with, and 0.46 ± 0.04 $\Delta F/F_0$ /s without the microECoG device (n=72 and 42 events, p=0.34, two-sample t-test, mean ± SEM).

4.1.9. Immunohistology

The immune response elicited by the implantation of microECoG devices is an important aspect in chronic experiments. To assess the immune response following implantation of the Parylene HT / ITO device, I analyzed the fluorescence of DAPI and GFAP staining, neuron counts and cortical thickness in brain sections after 10-12 weeks of implantation of five male mice (M1-M5) from the in vivo experimental group, aged 117–149 days. After an implantation period of 42–116 days (Table 1), mice were sacrificed and subjected to immunohistochemical analysis. Table 2 summarizes statistical comparisons of this analysis.

Table 1. Three groups were formed for analysis according to the duration of implantation (M1, M2–4, M5), marked with shades of blue. Implantation length and age are given in days.

Animal	Implantation length	Age at implantation	Age at perfusion	Number of evaluated slices
M1	42	143	185	18
M2	75	149	224	18
M3	76	148	224	16
M4	83	145	228	17
M5	116	117	233	18

Examination of M2-4, implanted for 75, 76 and 83 days, served as the starting point of the evaluation (Figure 18). Intensity of DAPI and NeuroTrace stainings were higher in superficial ROIs of M2-4 on the implanted side (DAPI: 4.96% ± 28.94%, p = 0.0123; NeuroTrace: 5.41% ± 24.73%, p = 0.0165), but not in deep ROIs (Figures 20 B-G). A higher NeuroTrace intensity is a sign of elevated protein synthesis capacity, indicative of Nissl substance redistribution to the periphery of cells in injured or regenerating neurons. Intensity of GFAP stainings were moderately higher on both superficial (11.21% ± 38.51%, p = 0.0018) and deep ROIs of M2-4 (7.56% ± 33.94%, p = 0.0042) (Figure 18 H–J, Figure 19 A), indicating an elevated astroglial presence after a considerably long period of implantation. While neuronal density was not different between the implanted

and control side (Figure 19 B), the cortex on the implanted side was thinner (−23.36 µm ± 66.34 µm, p = 0.0201; Figure 19 C). In M1, implanted for 42 days, the intensity of DAPI and NeuroTrace stainings were higher in superficial ROIs (DAPI: 12.07% ± 18.15%, p = 0.0142; NeuroTrace: 8.27% ± 17.63%, p = 0.0482), but not in deep ROIs (Figure 20 A–G), just as in M2-4. The intensity of GFAP staining was greatly increased in both superficial (187.78% ± 71.61%, p < 0.0001) and deep ROIs (50.18% ± 38.45%, p = 0.0361) (Figure 20 H–J; Figure 19 A), indicating the ongoing peak astroglial response. Although the difference in neuronal density was nonsignificant (Figure 19 B), the cortex on the implanted side was again thinner (−32.49 µm ± 42.13 µm, p = 0.0045) (Figure 19 C). Generally, results of M1 mirror those of M2-4 with a larger magnitude, suggesting an attenuation of the observed effects over time (Figure 19 A). Moreover, the significant differences in labeling intensities of M1 and M2-4 on superficial, but not on deep ROIs suggests a greater and more localized impact of implantation on superficial layers. In M5, implanted for 116 days, the intensity of DAPI and NeuroTrace stainings were significantly lower in the superficial ROIs on the implanted (DAPI: −10.53% ± 26.44%, p = 0.0083; NeuroTrace: −16.2% ± 13.55%, p = 0.0003), but not in deep ROIs (Figure 21 A–G). The intensity of GFAP staining was also lower in superficial ROIs of the implanted side (−8.13% ± 17.74%, p = 0.0361) (Figure 21 H–J; Figure 19 A). Contrary to M1 and M2-4, neuronal density of the implanted side in M5 was significantly lower (−2.32% ± 4.13%, p = 0.015) (Figure 19 B). This was paired, however, with a significantly thicker cortex (31.26 µm ± 33.21 µm, p = 0.0009) (Figure 19 C). The lower intensity of the three stainings on the implanted side in M5 is noteworthy. In the sense of continuity, it complements the attenuating trend of M1 and M2-4, although a balanced or slightly higher intensity on the implanted side was more expected. The thicker cortex on the implanted side also corresponded to the intensity data, while neural density deviated from the tendency of the results of M5. Finally, as in M1 and M2-4, the differences between control and implanted ROIs were larger in the superficial ROIs.

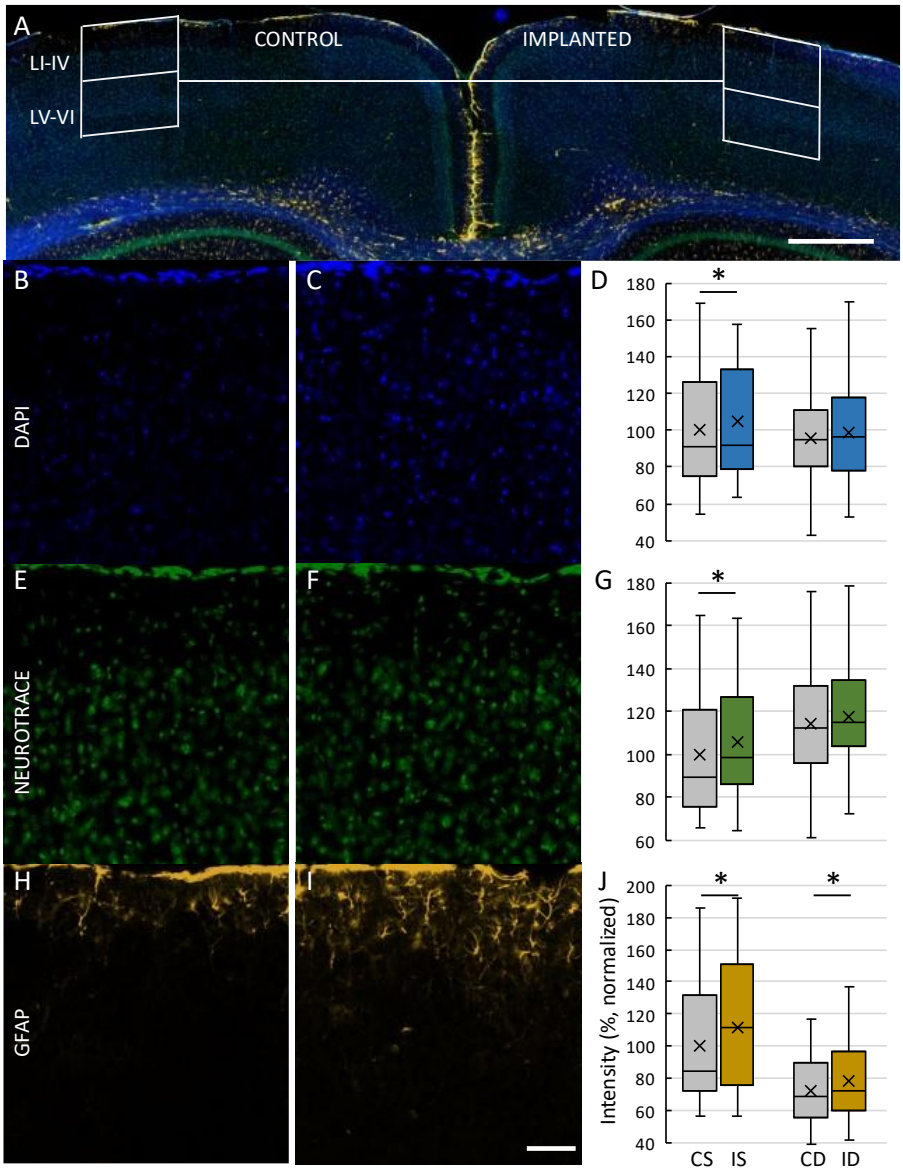

Figure 18. Images of stained brain sections of a mouse (M2) chronically implanted with a Parylene HT / ITO ECoG device for 75 days. (A) Composite image of a coronal slice showing the arrangement of ROIs on control (B, E, H) and implanted (C, F, I) cortex. ROIs are divided into superficial (layers I–IV) and deep (layers V–VI). Magnification 3.2X, scale bar 500 µm. (B, C) Cell nuclei stained with DAPI. (E, F) Neurons stained with NeuroTrace, a fluorescent Nissl stain. (H, I) Astrocytes labeled with GFAP. Magnification 20X, scale bar 50 µm. (D, G, J) Comparison of ROI fluorescent intensity of DAPI (D), NeuroTrace (G) and GFAP (J) labeling. Mean ROI intensity was normalized to ROI area and presented here as a percentage of the mean of control, superficial ROIs

of their respective stainings. CS – control, superficial. IS – implanted, superficial. CD – control, deep. ID – implanted, deep. Asterisks denote significant differences ($p < 0.05$).

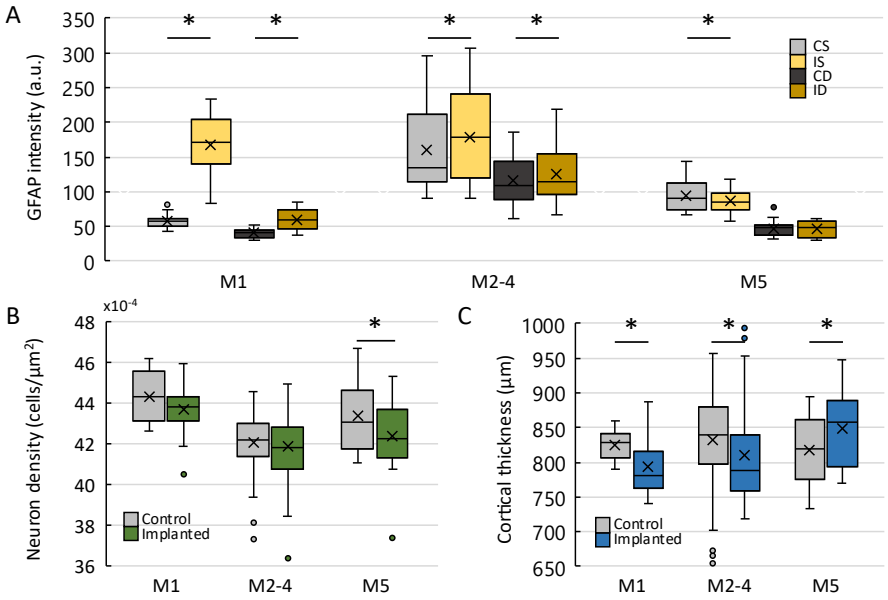

Figure 19. Characterisation of implanted and control hemispheres of three implantation lengths. (A) Comparison of fluorescence intensities of GFAP stainings between superficial and deep ROIs on control and implanted hemispheres. Mean ROI intensity was normalized to the ROI area. CS – control, superficial. IS – implanted, superficial. CD – control, deep. ID – implanted, deep. (B) Neuron density on control and implanted hemispheres. Counted cells in superficial and deep ROIs were summed and normalized to the summed area of both ROIs. (C) Cortical thickness on control and implanted hemispheres. Asterisks denote significant differences ($p < 0.05$).

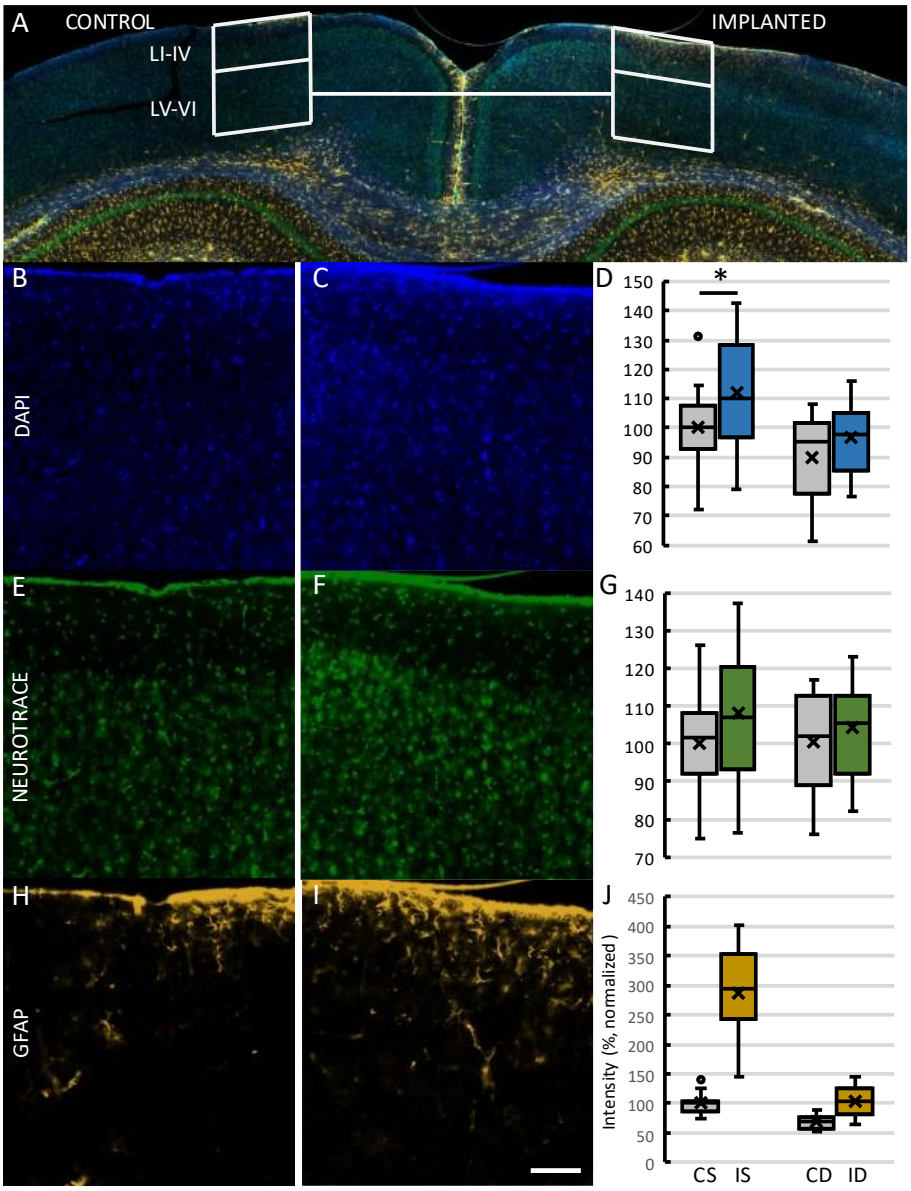

Figure 20. Images of a Parylene HT / ITO ECoG implanted brain after 42 days of chronic implantation (M1). (A) Composite image of a coronal slice showing the arrangement of ROIs on control (B, E, H) and implanted (C, F, I) cortex. ROIs are divided into superficial (layers I-IV) and deep (layers V-VI). Magnification 3.2X, scale bar 500 µm. (B, C) Cell nuclei stained with DAPI. (E, F) Neurons stained with NeuroTrace, a fluorescent Nissl stain. (H, I) Astrocytes labeled with GFAP. Magnification 20X, scale bar 50 µm. (D, G, J) Comparison of ROI fluorescent intensity of DAPI (D), NeuroTrace (G) and GFAP (J) labeling. Mean ROI intensity was normalized to ROI area and presented here as a percentage of the mean of control, superficial ROIs of their respective stainings. CS -

control, superficial. IS - implanted, superficial. CD - control, deep. ID - implanted, deep. Asterisks denote significant differences ($p<0.05$).

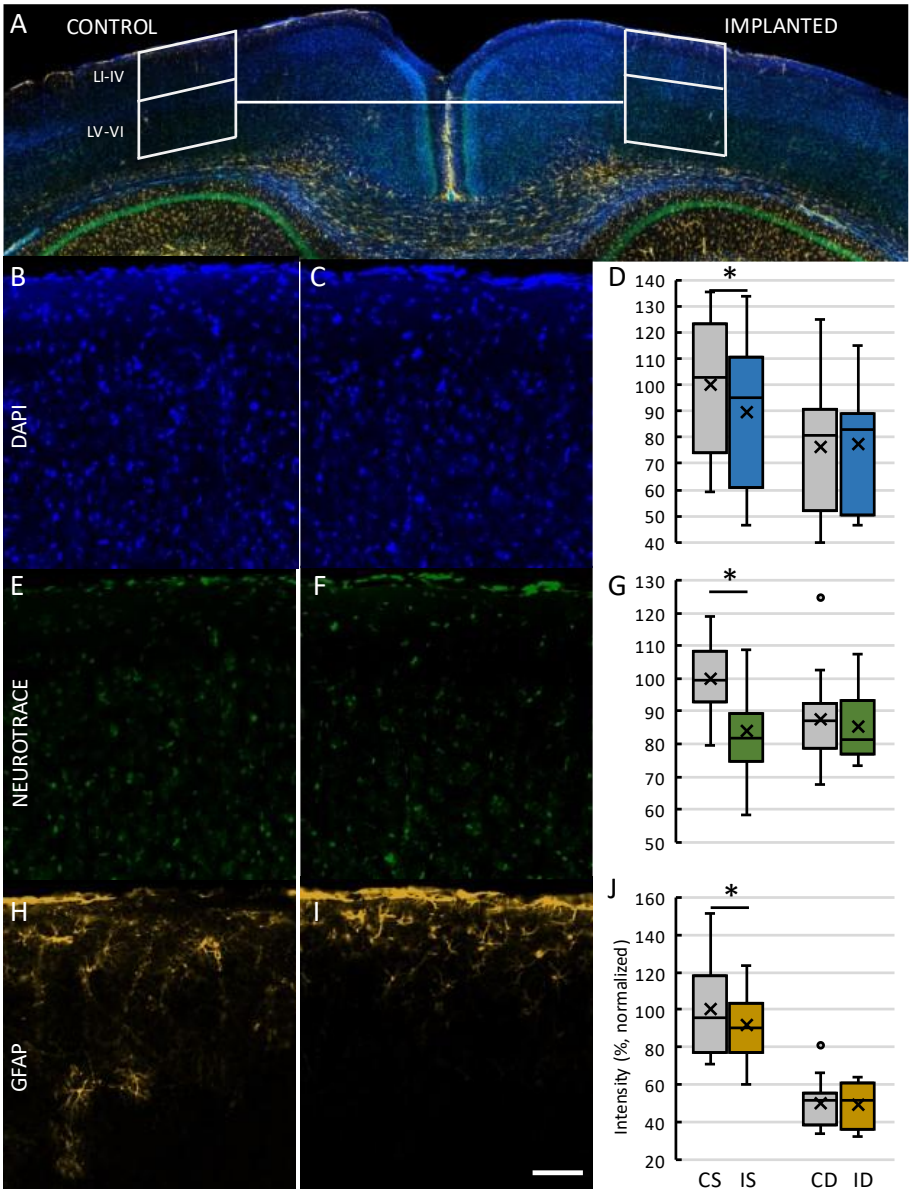

Figure 21. Images of a Parylene HT / ITO ECoG implanted brain after 116 days of chronic implantation (M5). (A) Composite image of a coronal slice showing the arrangement of ROIs on control (B, E, H) and implanted (C, F, I) cortex. ROIs are divided into superficial (layers I-IV) and deep (layers V-VI). Magnification 3.2X, scale bar 500 µm. (B, C) Cell nuclei stained with DAPI. (E, F) Neurons stained with NeuroTrace, a fluorescent Nissl stain. (H, I) Astrocytes labeled with GFAP. Magnification 20X, scale bar 50 µm. (D, G,

J) Comparison of ROI fluorescent intensity of DAPI (D), NeuroTrace (G) and GFAP (J) labeling. Mean ROI intensity was normalized to ROI area and presented here as a percentage of the mean of control, superficial ROIs of their respective stainings. CS - control, superficial. IS - implanted, superficial. CD - control, deep. ID - implanted, deep. Asterisks denote significant differences ($p<0.05$).

Table 2. Data on statistical tests of Parylene HT / ITO implanted animals. NT – NeuroTrace. Superf. – superficial.

Data	Stain	Mouse	ROI	Difference (%)	SD (%)	Statistical test	t / W value	# of pairs	p
Intensity	DAPI	M1	Superf.	12,07	18,15	Paired t - test	2,772	15	**0,0142**
Intensity	DAPI	M1	Deep	7,58	14,26	Paired t - test	2,001	15	0,0638
Intensity	DAPI	M2-4	Superf.	4,96	28,94	Wilcoxon matched-pairs signed rank test	530	51	**0,0123**
Intensity	DAPI	M2-4	Deep	3,73	28,26	Paired t - test	1,577	50	0,1211
Intensity	DAPI	M5	Superf.	-10,53	26,44	Paired t - test	2,985	17	**0,0083**
Intensity	DAPI	M5	Deep	1,44	28,20	Paired t - test	0,3509	17	0,73
Intensity	NT	M1	Superf.	8,27	17,63	Paired t - test	2,151	15	**0,0482**
Intensity	NT	M1	Deep	3,79	12,78	Paired t - test	1,167	15	0,2615
Intensity	NT	M2-4	Superf.	5,41	24,73	Paired t - test	2,48	50	**0,0165**
Intensity	NT	M2-4	Deep	2,48	20,71	Paired t - test	1,122	50	0,2671
Intensity	NT	M5	Superf.	-16,20	13,55	Paired t - test	4,556	17	**0,0003**
Intensity	NT	M5	Deep	-2,50	12,67	Paired t - test	0,671	17	0,5113
Intensity	GFAP	M1	Superf.	187,78	71,61	Paired t - test	11,75	15	**<0.0001**
Intensity	GFAP	M1	Deep	50,18	38,45	Paired t - test	5,621	15	**0,0361**
Intensity	GFAP	M2-4	Superf.	11,21	38,51	Wilcoxon matched-pairs signed rank test	654	51	**0,0018**
Intensity	GFAP	M2-4	Deep	7,56	33,94	Paired t - test	3,002	50	**0,0042**
Intensity	GFAP	M5	Superf.	-8,13	17,74	Paired t - test	2,276	17	**0,0361**
Intensity	GFAP	M5	Deep	-2,13	22,80	Paired t - test	0,5576	17	0,5844
Density	NT	M1	Both	-1,40	2,84	Paired t - test	1,604	17	0,1272
Density	NT	M2-4	Both	-0,43	3,94	Wilcoxon matched-pairs signed rank test	-176	51	0,4153
Density	NT	M5	Both	-2,32	4,13	Paired t - test	2,705	17	**0,015**
Thickness	DAPI	M1	NA	-32,49	42,13	Paired t - test	3,272	17	**0,0045**
Thickness	DAPI	M2-4	NA	-23,36	66,34	Wilcoxon matched-pairs signed rank test	-493	51	**0,0201**
Thickness	DAPI	M5	NA	31,26	33,21	Paired t - test	3,994	17	**0,0009**

4.2. Characterization of the Thiol-ene/acrylate / SIROF device

The Thiol-ene/acrylate based microECoG devices were fabricated in two configurations. During packaging, after exposing gold recording sites and bonding pads, an additional 300 nm thick SIROF layer was patterned on top of the recording sites (SIROF devices), or this step was omitted (gold-only devices). Of the 6 mice used for cortical in vivo experiments with Thiol-ene/acrylate devices, 3 mice implanted with 3 SIROF devices were used for immunohistology and 3 mice implanted with 1 SIROF and 2 gold-only devices were used for in vivo two-photon calcium imaging. As both configurations exclude the possibility of involving the recording sites in the imaging field of view, the difference had little impact on the two-photon imaging capability. Impedance spectroscopy, where the configuration difference is most expected to be relevant, was performed for both device configurations. The Thiol-ene/acrylate devices implanted over the hippocampus were SIROF devices.

4.2.1. Electrochemical stability

Electrode impedance spectroscopy was performed in a 16 day experiment where the device was immersed in room temperature PBS and the impedance magnitude and phase angle of the device was measured daily.

The initial impedance of the recording sites on the SIROF devices in the mice used for immunohistology was 7.33 ± 1.93 kΩ on average (n = 31), which decreased minimally by the 6th day (5.54 ± 0.49 kΩ, n = 31). Impedance did not change afterwards during the soaking experiment until the last day (5.31 ± 0.50 kΩ, Figure 22). Phase angle shifted from the initial −40.0 ± 6.9° degree to −18.5 ± 2.5° by the 6th day, then remained stable. An equivalent circuit model was built to analyze the results of the impedance spectroscopy. Parameters of the equivalent circuit model suggest that electrode behavior and conductivity were dominated by resistance. The uniform decrease in the impedance (Figure 22 C), changes in the value and characteristics of the phase curves mainly at higher frequency ranges and the slight decrease of CCPE and α indicated a possible penetration of electrolyte (i.e. water uptake) throughout polymer layers of the substrate. Of the 31 recording sites, 29 remained functional by the end of the immersion experiment.

Of the devices used in the in vivo two-photon experiments, the initial average impedance of the two gold - only device was 9.9 ± 1.8 kΩ at 1 kHz, which decreased to 9.2 ± 5.7 kΩ after 16 days. Average impedance of the SIROF device was 6.4 ± 0.9 kΩ at 1 kHz, which decreased to 4.1 ± 0.3 kΩ after 16 days (Figure 23). During the EIS test, the number of functional electrodes decreased from 30 functional sites to 26 (impedance rose over 500 kΩ), which we associated with compromised bonding pad connections. Changes in impedance were likely due to the water uptake of the substrate material [Zátonyi 2019].

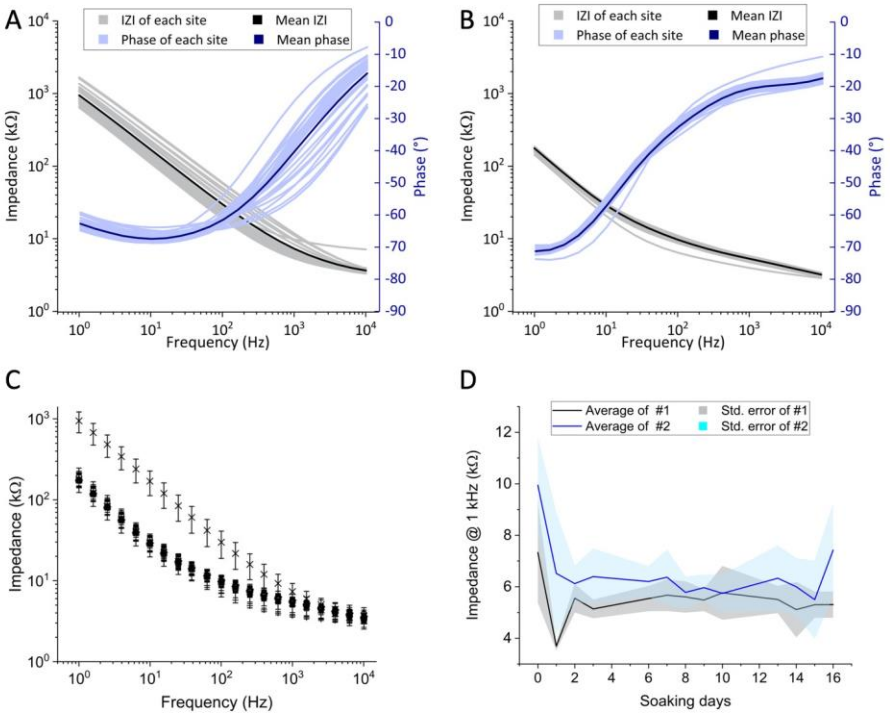

Figure 22. Electrochemical impedance spectroscopy of SIROF devices used for in vivo electrocorticography and immunohistology. (A, B) Pale gray lines represent the impedance; pale blue lines represent the phase across the 1 Hz–10 kHz frequency range for all functional electrode sites immediately after immersion (A) and on the 16th day (B) of soaking test. Thick lines represent the averages. (C) Impedance of all frequencies (1 Hz–10 kHz) for a representative microECoG device at 13 time points (Mean of each electrode □} standard error: initial (X), 1st (+), 2nd (◯), 3rd (□), 6th (△), 7th (▽), 8th (◊), 9th (◁), 10th (▷), 13th (⬡), 14th (☆), 15th (⬠), 16th (✻) day of EIS test period).

(D) Average impedance (thick black and blue lines) at 1 kHz on two different but functionally identical microECoG devices. Shaded areas represent the standard error.

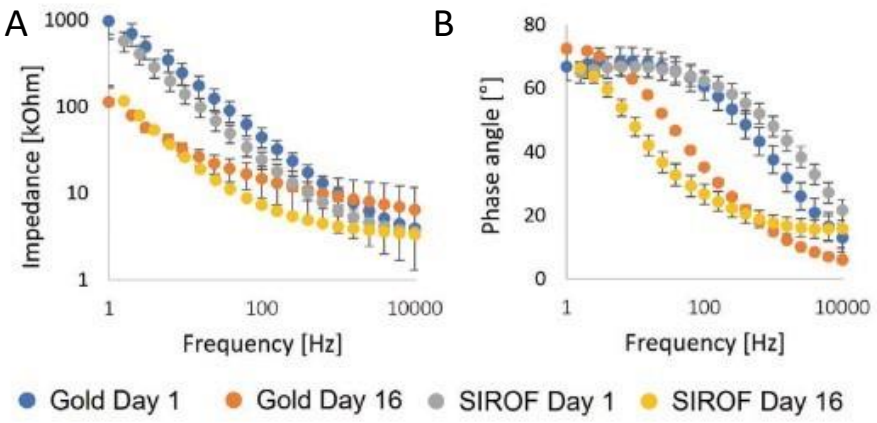

Figure 23. (A) Mean magnitude of impedance and (B) phase angle of gold-only or SIROF devices after encapsulation (Day 1) and after a 16-day long soaking test. Whiskers show SD.

4.2.2. Microbead measurements

The potential influence the implanted device may have on spatial resolution was investigated by two-photon imaging of fluorescent microbeads with a nominal diameter of 6.0 μm with and without the Thiol-ene/acrylate device covering them. The field of view was matched in the two conditions, so that the same microbeads can be measured. The diameter of 68 microbeads were measured with and without device cover with a custom MATLAB based algorithm. Mean size without the device was calculated to be 5.6651 ± 0.0066 μm, (Figure 24 C), which was not a significant difference (Student's two-sample paired t-test, ($t(67) = 1.08$, $p = 0.29$, difference of means: 0.0142 μm).

4.2.3. Neurite size measurements

Before proceeding to in vivo experiments, the quality of two-photon calcium imaging was further tested on in vitro hippocampal slices of GCaMP6f expressing mice. To compare image quality, neurite diameter was measured with and without the microECoG device on acute brain slices (Figure 24 A, B). Neurites were detected on images of

hippocampal regions, where the plane of the image was parallel to the neurites, to maximize the number of samples. Our custom detection algorithm detected 81 neurites on images without the device and 112 neurites with the device present. There was no significant difference between the neurite diameters without and with the microECoG device (Figure 24 D, Student's two-sample t-test, $\alpha = 0.05$). The results of this in vitro comparison show that even fine neuronal structures can be imaged in the hippocampus in the presence of the device reliably.

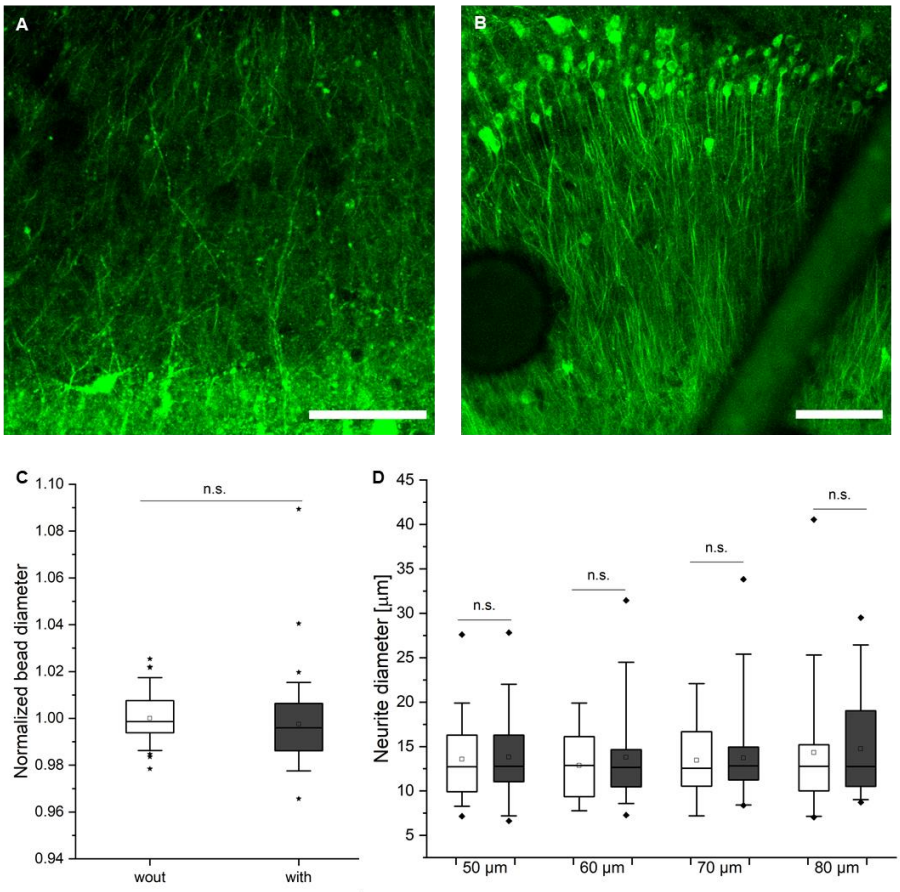

Figure 24. Representative images of hippocampal regions without (A) and under (B) the microECoG device. Scale bars are 100 µm. (C) Diameter of the same microbeads without (n = 68) and with (n = 68) the microECoG device covering them. Values are normalized to the mean diameter of the beads without the device (5.67 ± 0.0066 µm). (D) Diameter of neurites measured on in vitro slices from the same field of view at different depths. Empty box plots show data without device cover and filled box plots show data with device on the slice. Boxplot whiskers are 5th and 95th percentiles, ◆ are the outliers.

4.2.4. In vivo electrocorticography

The ability of chronically implanted Thiol-ene/acrylate / SIROF devices to record electrocorticography were investigated in awake, freely moving, head-fixed mice on a weekly basis. Evaluation of functionality relied on impedance testing, which may reveal device failure, including any mechanical damage (cracking, delamination, leakage), and on calculation of SNR of the recorded data. Recording sites were monitored before and after implantation, up to the point when the mice were sacrificed.

In case of mice used for immunohistology, impedance magnitude of recording sites at 1 kHz increased 6 days (73.10 ± 27.81 kΩ, n = 24) and further 12 days after implantation (127.72 ± 52.73 kΩ, n = 24), compared to immediately before the implantation (16.56 ± 2.62 kΩ, n = 28), then remained stable throughout the rest of the experiment (Figure 25 A). Average post-implantation SNR ranged from 1.04 to 5.74 on three different microECoG devices (Figure 25 B), and did not show any trends except for two consecutive outlying, low SNR measurements towards the end of the experiments, which recovered to previous ranges on the last measurement. The number of functional electrodes decreased by 25% after implantation, but no additional loss was observed throughout the rest of the in vivo experiment (Figure 26). Representative raw and theta frequency (3.5 – 11 Hz) filtered ECoG data of these devices is shown on Figure 25 C.

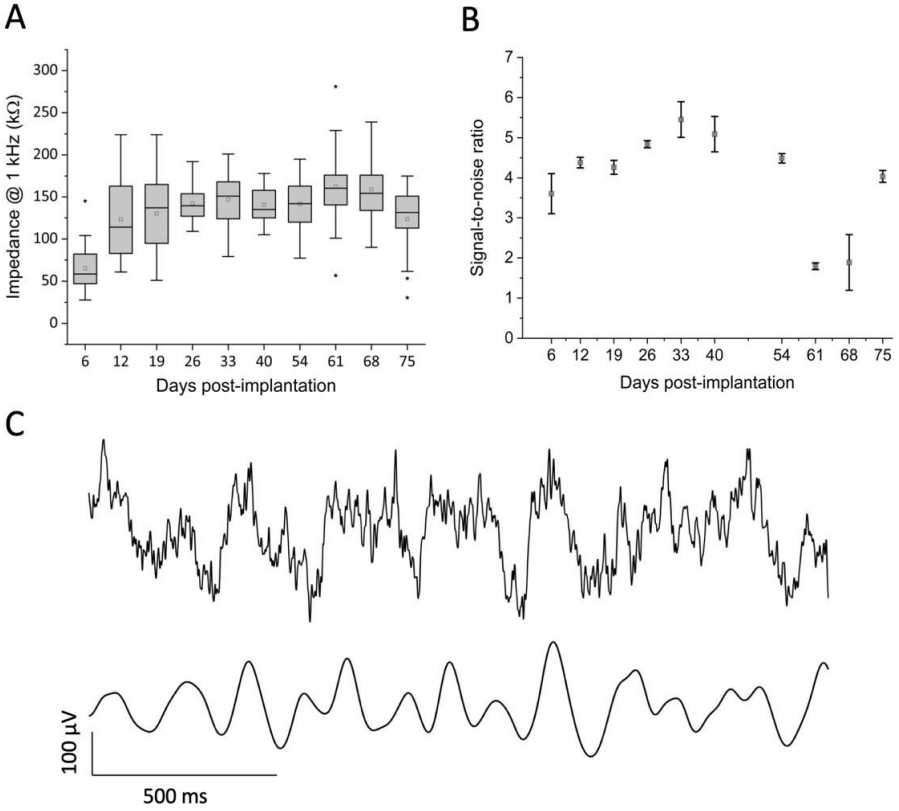

Figure 25. (A) Post-implantation impedance of one device at 1 kHz. Acceptance limit as a functional electrode was 500 kΩ. Post-implantation data are from n = 24 electrodes of the same representative device. Impedance magnitude increased over time from day 6 until day 61, then started to decrease. (B) SNR at ten time points (n = 24). Data are shown as mean ± standard error. (C) 2 s long filtered ECoG signal from a representative electrode at the 33rd day post-implantation and the theta range (3.5 – 11 Hz) of the signal. In A–C), data were collected and analyzed from the same mouse (#2) of the group used for immunohistology.

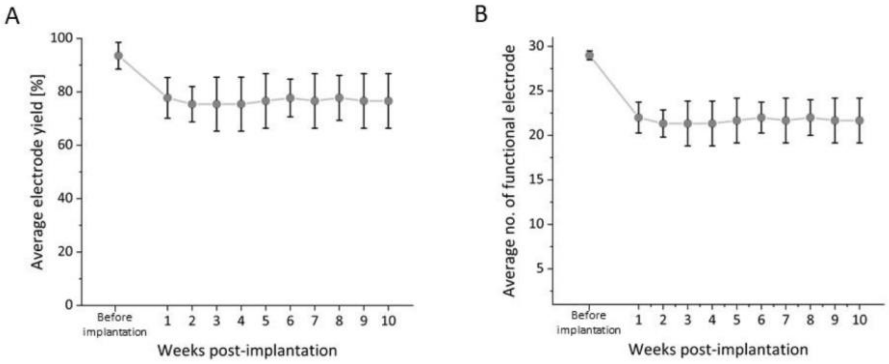

Figure 26. (A) Average electrode yield (percentage of functional channels out of all) and (B) absolute number of functional electrodes before implantation and at different time points after implantation. Data are shown as mean (%) ± standard error (%) from three different microECoG devices.

Regarding the devices used in the in vivo two-photon experiments, there was a decrease in the average impedance of gold-only devices after implantation (Figure 27 A), but no significant change occured between Week 2 and Week 11 (Student's -paired sample t-test at $\alpha = 0.05$: $t(9) = 0.12$, $p = 0.91$). At the same time, the SNR increased slightly (Figure 27 B). The average impedance of the SIROF device increased after implantation and also between Week 1 and Week 22 significantly (Student's paired sample t-test at $\alpha = 0.05$: $t(9) = -5.81$, $p << 0.05$), but still remained under 100 kΩ (Figure 28 A). At the same time, the SNR increased moderately (Figure 28 B). "Precranio" values are derived from measurements in saline, while the rest of the data were collected after implantation. Health condition of the two mice implanted with gold-only devices required earlier termination of the experiment than the mouse implanted with the SIROF based device. This was unrelated to the difference in the material composition of the devices.

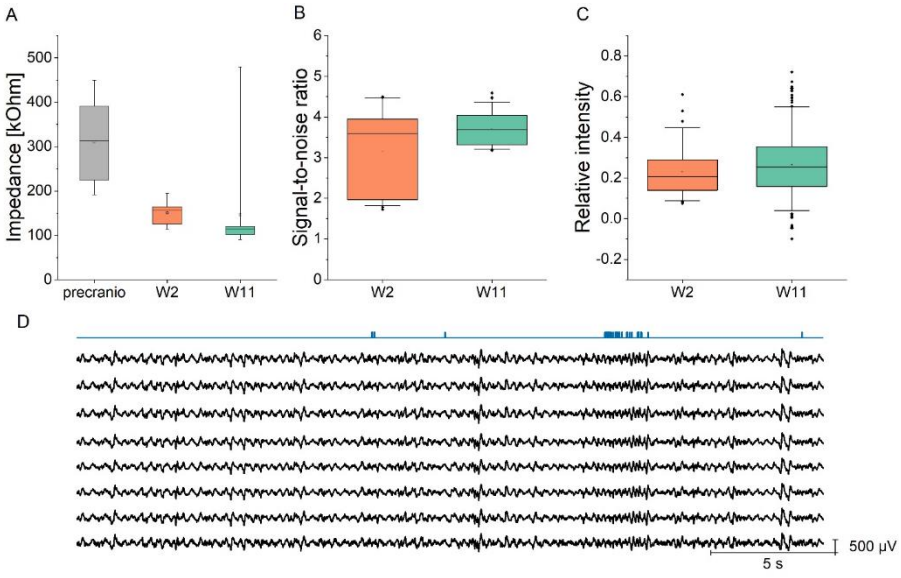

Figure 27. Measurements with a Thiol-ene/acrylate / gold-only microECoG device. (A) Average impedance values of the channels (n = 10) on different measurement days at 1 kHz. (B) Signal-to-noise ratio on the first (n = 55) and last (n = 66) measurement day. (C) Long-term two-photon relative intensity change compared to the background intensity (nW2 = 66; nW11 = 254). The different boxes represent the different measurement days. Boxplot whiskers are 5th and 95th percentiles, and ◆ are the outliers. (D) 30 s long representative electrophysiological activity captured on W11 (Week 11) by the ECoG. The blue curve represents the movement of the animal.

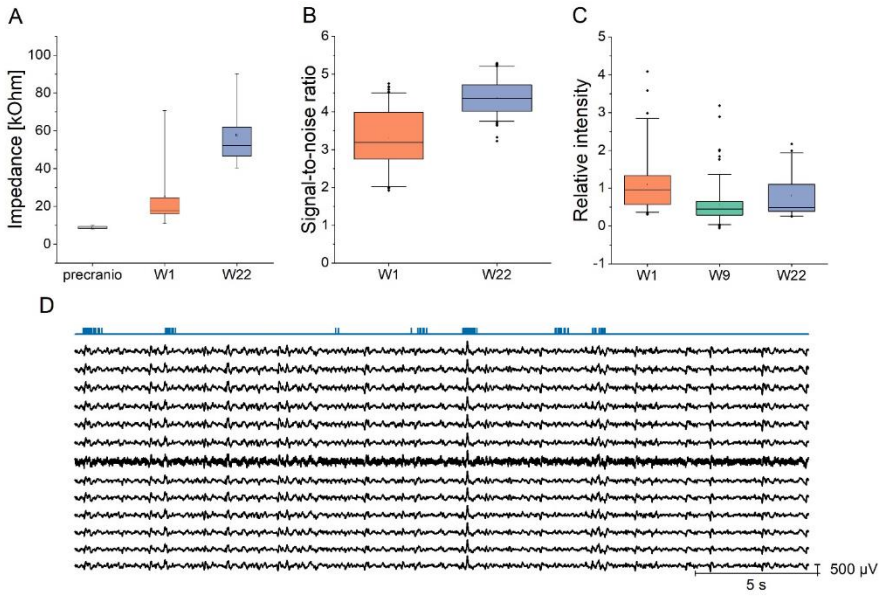

Figure 28. Measurements with a Thiol-ene/acrylate / SIROF microECoG device. (A) Average impedance values of the channels (n = 10) on different measurement days at 1 kHz. (B) Signal-to-noise ratio on the first (n = 135) and last measurement day (n = 143). (C) Long-term two-photon intensity change of cells relative to background intensity (nW1 = 67; nW22 = 57). Box plots represent different measurement days. Boxplot whiskers are 5th and 95th percentiles, and ◆ are the outliers. (D) 30 s long representative electrophysiological activity captured on W22 (Week 22) by the ECoG. The blue curve represents the movement of the animal.

4.2.5. Hippocampal sharp wave - ripples

Besides cortical implantations, Thiol-ene/acrylate / SIROF devices were implanted over the hippocampus as well, to measure field potentials and calcium events with the microECoG device and two-photon imaging. The devices were placed on the hippocampal surface after removing the overlying cortex and fixed in place with an optically transparent cylindrical silicon deep brain adapter. This procedure and experimental setup was granted by the improved adaptability of the Thiol-ene/acrylate microECoG devices, a result of its design process, as it required the flexibility of the device as well as space management for successful chronic use.

In the weekly recordings, sharp wave-ripples (SPW-Rs) (Figure 29) and MUA/SUA (Figure 33) could be detected in the local field potential (LFP) recordings and SPW-Rs detected on identical channels could be compared longitudinally (Figure 31), supporting the capability of the device in chronic electrophysiological recordings. SPW-Rs displayed a wide range in amplitude (Figure 30) and in spatial involvement as well, appearing on a fraction or on the majority of the recording sites (Figure 32). Based on the event distribution of SPW-Rs, we categorized events recorded 2 months after implantation in 3 recording sessions of 3 mice as widespread (detected on >10 channels, upper quartile of SPW-R detection distribution) or spatially-restricted (detected on 7-10 channels). The frequency of widespread and spatially-restricted SPW-Rs in these recordings was 0.1 Hz and 0.33 Hz on average, respectively (Figure 32).

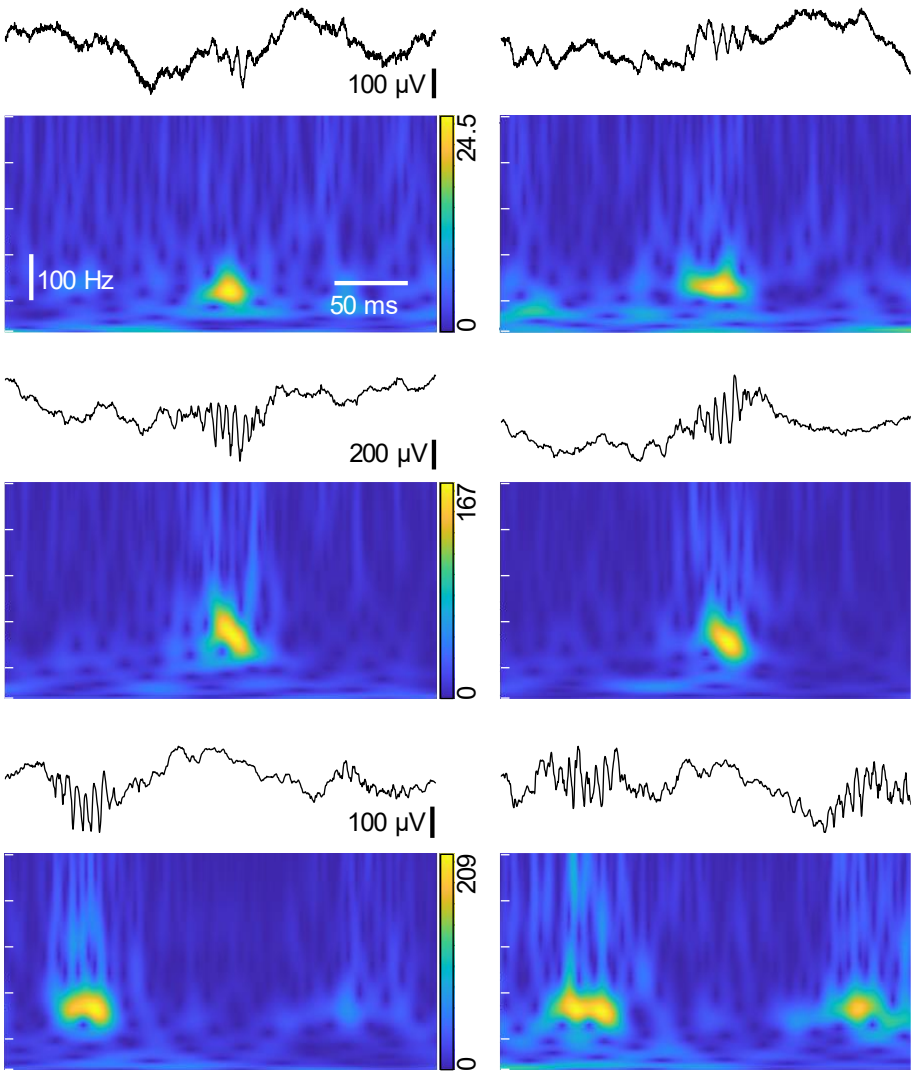

Figure 29. (A–C) Representative LFP data of characteristic SPW-Rs (top) and their continuous 1-D wavelet transforms (bottom, arbitrary units) after one week (A), one month (B) and two months (C) of implantation. Note the doublet SPW-R event on (C). (A) shows separate events, (B–C) show events detected simultaneously on different sites. Continuous wavelet transform (CWT) spectrogram coefficient magnitudes are shown as arbitrary units, and frequency scale bar ticks denote 31, 100, 200, 300, 400 and 500 Hz.

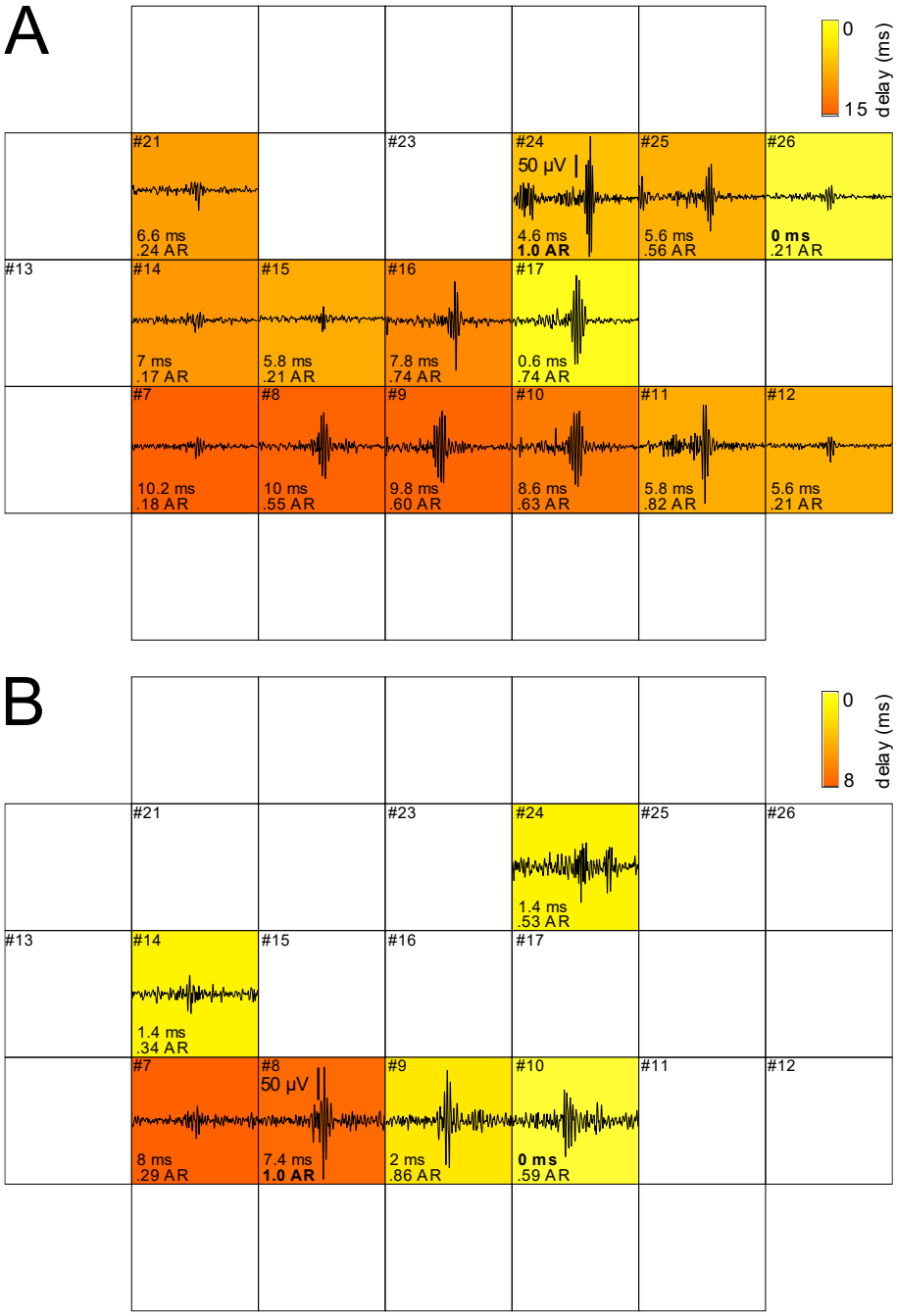

Figure 30. (A, B) Representative topography plots from the same recording show synchronous occurrence of SPW-Rs on multiple recording sites two months after implantation. (A) shows a widespread (>11 channels) event detected on 14 recording sites, while (B) shows a spatially more restricted event (<11 channels). LFP traces of SPW-Rs are shown for every recording site where the event was detected. The amplitude ratio (AR) of detected SPW-Rs, which is the peak-to-peak amplitude of a SPW-R on a site normalized to the highest detected peak-to-peak amplitude, is shown for every

involved recording site. The color scale indicates the delay relative to the earliest detection. Numbered but empty sites are channels where the impedance was acceptable, but no SPW-R was detected at the time of the event.

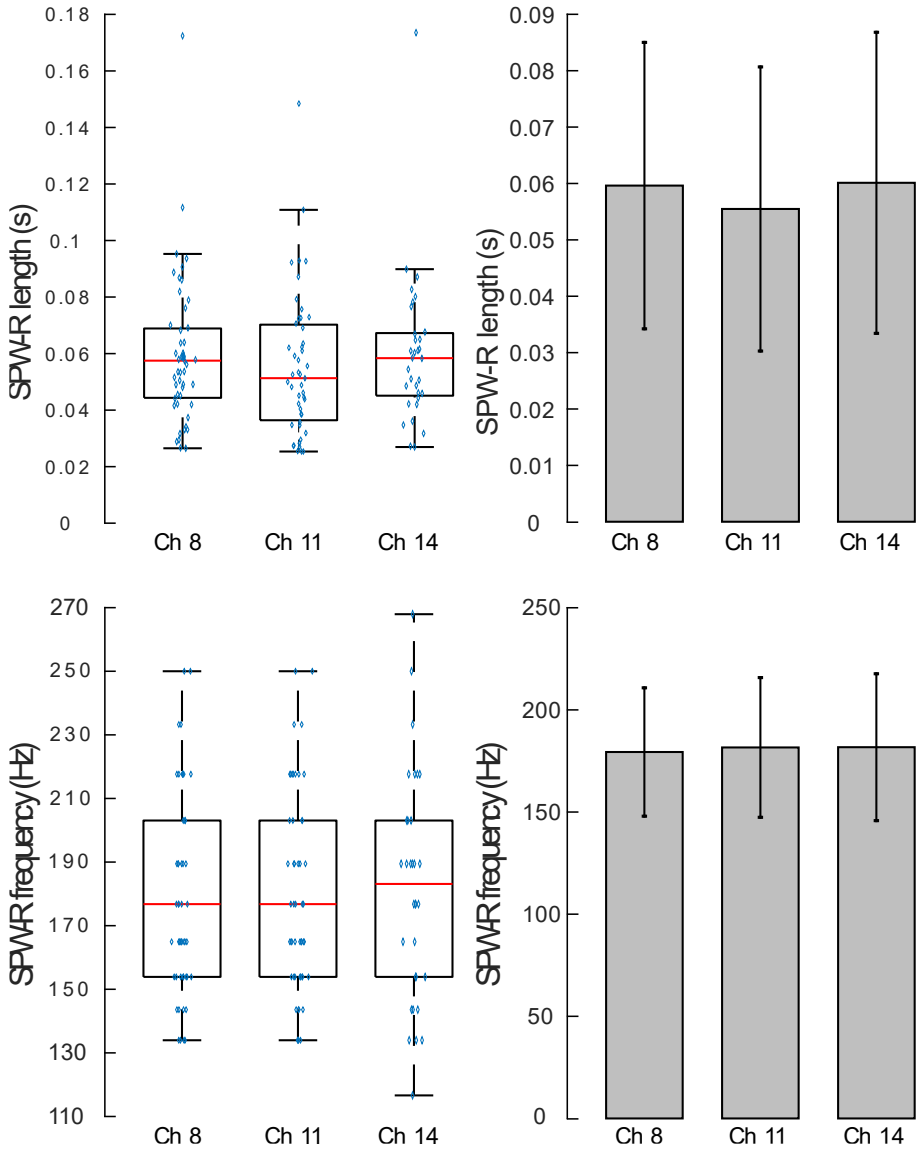

Figure 31. Characteristic features of SPW-Rs detected simultaneously on different channels two months after implantation in mouse 1. The length (upper) and frequency (lower) of detected SPW-R envelopes are presented as box plots (left) and bar graphs (right). Box plots show the interquartile range extending from the 25th to the 75th percentile, whiskers represent the furthest data point within 1.5 times the interquartile range from each box end. Any data point outside the boundary of the whiskers is

considered an outlier. The red line inside the boxplots shows the median. Bar graphs show mean ± SD of event lengths (upper) and frequencies (lower) from the same three channels.

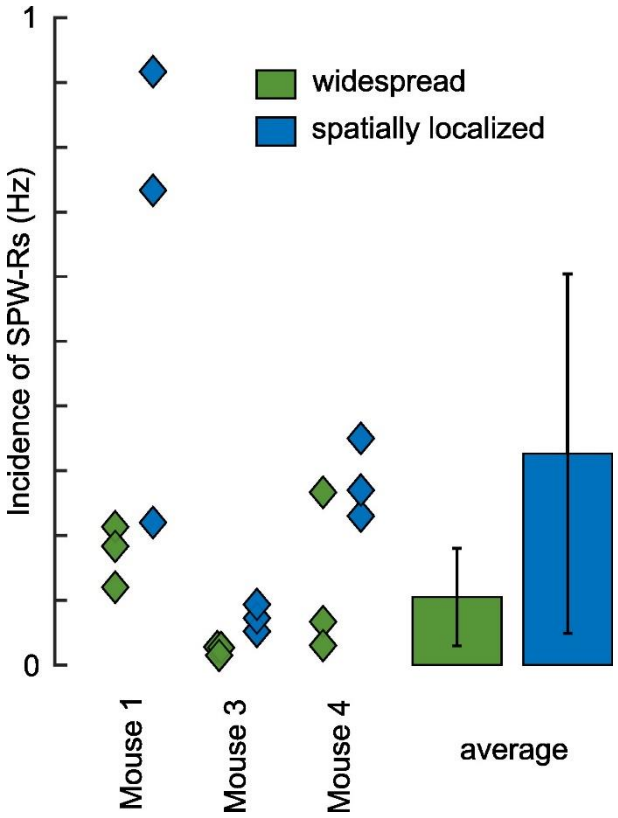

Figure 32. Incidence of sharp wave-ripples synchronously recorded on multiple recording sites two months after implantation, from 3 sessions of 3 animals. Events simultaneously appearing on up to 7-10 channels were considered as spatially localized (blue) while events with synchronous appearance on more than 10 channels were considered as widespread SPW-Rs (green). The occurrence of widespread and spatially-restricted SPW-Rs was 0.1 Hz and 0.33 Hz on average, respectively (right). Error bars represent mean ± SD.

4.2.6. Unit activity

For seven weeks, the data collected from a single hippocampally implanted animal consistently showed spikes. The recordings included both multi-unit and single-unit activity. To distinguish between the various cell types, putative pyramidal cells, narrow-

waveform interneurons, and wide-waveform interneurons were classified based on the trough-to-peak time of the waveform and the burstiness index. The clustering resulted in an average of 24.01% ± 7.8% of the cells being classified as narrow-waveform interneurons, 52.15% ± 14.63% as wide-waveform interneurons and 23.84% ± 14.24% as pyramidal cells. The distribution of detected cell types over the seven weeks is summarized in Table 3. The mean burstiness index for the different neuron types was 1.267 ± 0.208 for narrow-waveform interneurons, 1.033 ± 0.142 for wide-waveform interneurons, and 1.426 ± 0.273 for pyramidal cells. These values indicate that pyramidal cells tend to have a higher burstiness index than interneurons, reflecting their well-known burst firing patterns. Figure 33 A displays the waveforms of 82 spikes, along with their average, extracted from a cluster of a putative pyramidal cell that exhibited single-unit activity. Figure 33 B shows the auto-correlogram of this cluster, while Figure 33 C presents the firing rate and spontaneous firing of the single-unit activity (SUA) cluster. The investigation involved the analysis of spike clusters recorded over seven weeks using all available channels. The number of detected clusters varied based on recording quality and cell firing rates. The signal-to-noise ratio (SNR) was assessed over the seven weeks of recordings (Figure 33 D). The signal-to-noise ratio (SNR) fell below 1 in week five, although it was also within the same range as in weeks one and three. Figures 35 E, F show the mean amplitude and mean number of spikes observed in long-term recordings, respectively. The amplitude decreased over time, while the number of spikes increased. Additionally, Figure 33 G illustrates the average count of spike clusters detected in weekly recordings, which varied over the seven weeks. In addition to the overall analysis, the spike clusters identified on two specific channels during long-term recordings enabled a detailed examination of the characteristics of neuronal activity over an extended period. Figure 33 H illustrates the spike amplitude for the two identified spike clusters. Figure 33 I presents the corresponding firing rates for each cluster. It is noteworthy that the spike clusters under examination are in close alignment with the average amplitude and spike count data presented in Figure 33 E, F. This consistency lends further support to the reliability of our findings and suggests that the observed characteristics in the spike clusters reflect broader trends in the data.

Table 3. Percentages of the different cell types over the seven measurement weeks.

Weeks	Percentage of Narrow- waveform Interneurons (%)	Percentage of Wide-waveform Interneurons (%)	Percentage of Pyramidal Cells (%)
1	25	31,25	43,75
2	36,36	54,55	9,09
3	20	70	10
4	16,67	41,67	41,66
5	30,77	46,15	23,08
6	14,29	71,43	14,298
7	25	50	25

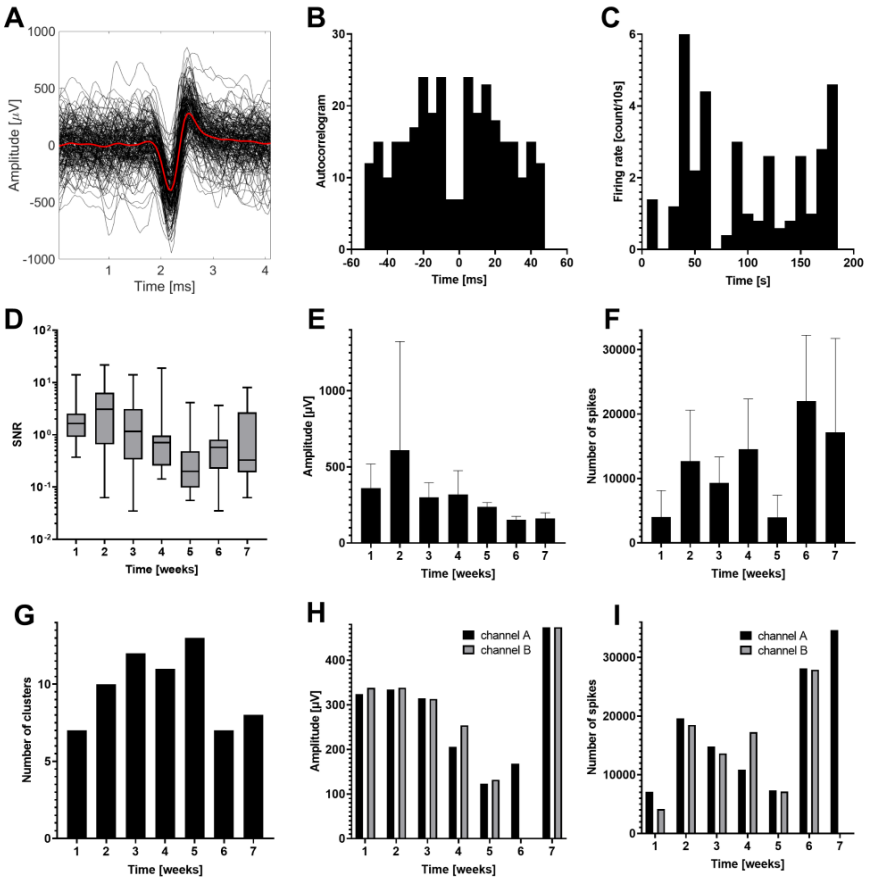

Figure 33. (A) Waveforms of one single-unit cluster, their average is highlighted (B) Auto correlogram of the single unit cluster. (C) Firing rate of the single unit cluster. (D) Signal-to-noise ratio of the clusters. The box plot shows the interquartile range, which extends from the 25th to the 75th percentile, and the whiskers represent the minimum and maximum values of the data set. (E) Mean amplitude of the spikes in all of the clusters during the chronic recordings. (F) Firing rate in all of the clusters. (G) Number of detected clusters in the chronic recordings. (H) Mean amplitude of the spikes in two clusters (cluster A and B). (I) Mean firing rate of cluster A and B. Error bars represent standard deviation.

4.2.7. In vivo two-photon calcium imaging

I imaged two-photon neuronal calcium activity in three awake, freely moving mice implanted cortically with the Thiol-ene/acrylate based device (one SIROF, two gold-only devices) over a chronic timescale (Figure 34). Mice underwent two to three imaging sessions at different time points after implantation, over a period of 22 weeks at most. GCaMP6f labeled neurons were prominent on the initial measurements 1–2 weeks after implantation and this clear distinction from the background continued for the rest of the experiment. We quantified this by calculating the intensity of automatically detected neurons compared to background fluorescence for each measurement day. Relative intensity change was not significantly different between measurement days of gold-only devices (Student's t-test: $t(65) = -0.79$, $p = 0.43$)(Figure 27 C). Although in the case of SIROF based devices, there was a significant difference between the relative intensity values on different measurement days (one-way repeated measures analysis of variance in OriginPro: $F(1.72, 96.15) = 16.99$, $p << 0.05$), the mean of the relative intensity stayed over 0.5 during the whole measurement period (Figure 28 C). Since imaging was performed with the same substrate material (Thiol-ene/acrylate) in the light path in the case of both devices, we hypothesize that the optical performance was influenced by other aspects, most likely suboptimal expression of GCaMP6f. Chronic imaging quality may be influenced by the immune response, sensor expression, and tissue regrowth, as well as factors introduced by the device. Nevertheless, cells also displayed spontaneous calcium activity often exceeding 50% increase in relative fluorescence (Figure 34 B, D, F), and

the same cells were identifiable between measurements through 21 weeks (Figure 34 A, C, E).

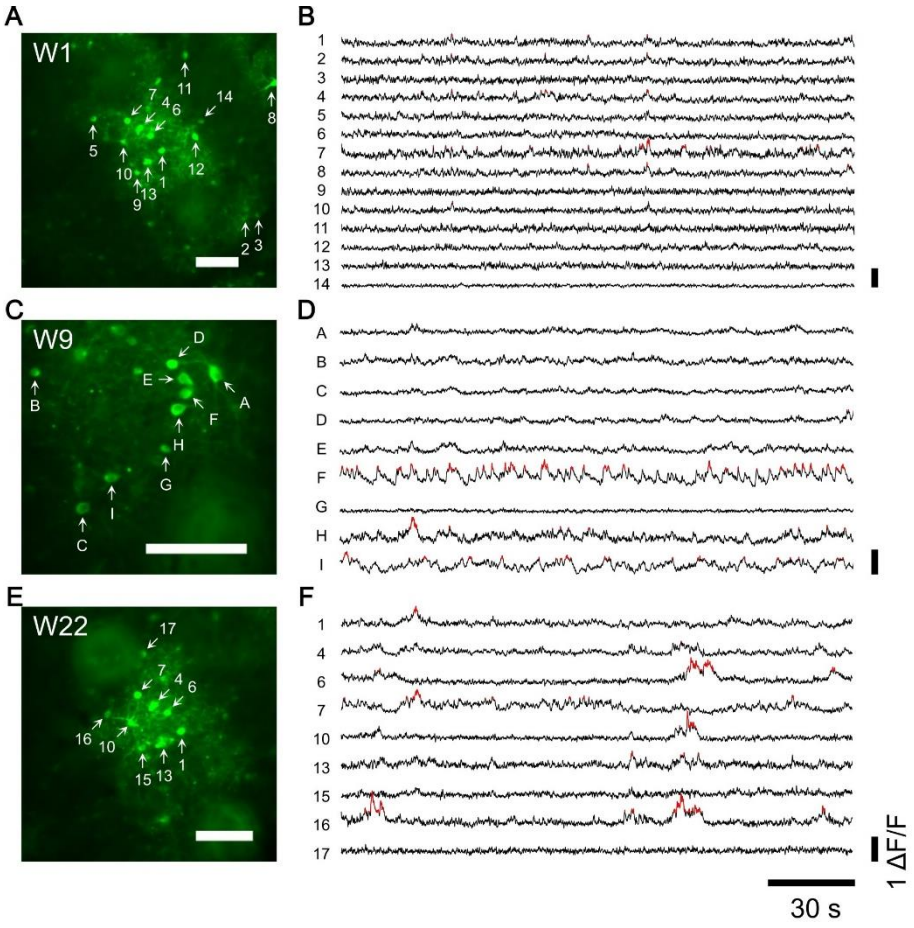

Figure 34. (A, C, E) In vivo two-photon imaging field-of-view and (B, D, F) spontaneous neural activity on different measurement days of a mouse implanted with a Thiol-ene/acrylate / SIROF device. (A, B) 1 week post implantation. (C, D) 9 weeks post implantation. (E, F) 22 weeks post implantation. Images were recorded 150 µm below the brain surface. Field-of-view on (A) and (E) is identical, and numbers on (B) and (F) label activity of the same cells measured 1 and 22 weeks post implantation. On (B, D, F), $\Delta F/F_0$ increases of over 50% are highlighted in red. Scalebar shows 100 µm.

For hippocampal two-photon imaging, the Thiol-ene/acrylate based device was implanted over the hippocampus of GCaMP6f expressing transgenic mice. Hippocampal two-photon imaging is constrained by the increased working distance compared to the cortical

imaging. In this case, the implanted transparent microECoG device allowed optical access to the dorsal hippocampus and provided ipsilateral electrophysiology signals. Figure 35 A shows the implanted Thiol-ene/acrylate device on the hippocampal surface. The transgenic mouse line showed a net-like expression pattern of GCaMP6f in the pyramidal layer, which was clearly visible in the implanted animals and a sham-implanted littermate (Figure 35 B, C).

Leveraging the flexible 3D scanning capability of the AO microscope with chessboard scanning, multiple areas were scanned in different planes of the field of view. For the recording of spontaneous calcium activity, we divided the FOV into three chessboard scans according to their best match to the pyramidal layer. Each chessboard scan covered a 100 by 100 µm square area. This simultaneous high-speed scanning of multiple areas picked-up the sparse, stochastic activity of the densely populated CA1 neurons (Figure 35 D, Figure 36).

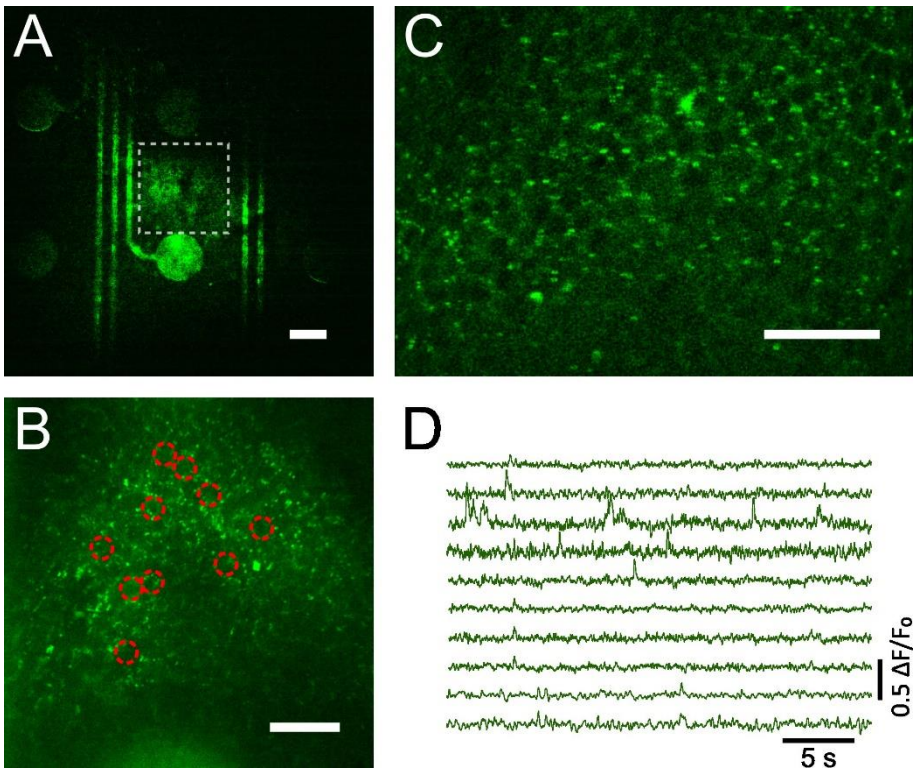

Figure 35. Calcium activity recorded from mice implanted with a Thiol-ene/acrylate device. (A) Two-photon image of the Thiol-ene/acrylate device covering six recording sites. The grey box shows the field of view on B. Scale bar is 100 µm. (B) Two-photon

image showing the pyramidal layer under the device, from the box on A. The FOV was selected to be between the central sites on panel A. Red circles show the ROIs for D. Scale bar is 50 µm. (C) GCaMP6f. expression in the pyramidal layer of a thy1-GCaMP6f. transgenic mouse without device implantation. Scale bar is 50 µm. (D) Representative calcium traces of GCaMP6f. labelled cells from the area in B, in the CA1 pyramidal layer during spontaneous activity.

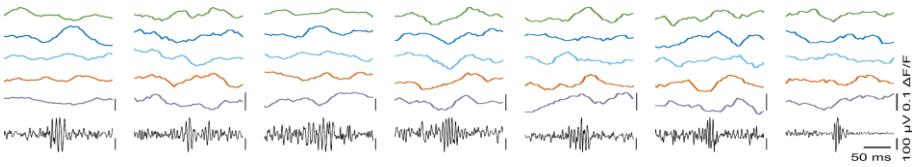

Figure 36. Example neuronal calcium activity and correlated SPW-Rs recorded from 5 neurons in a single session of mouse 1. Colored traces show neuronal calcium activity, black traces below show filtered concurrent SPW-R activity. Scale bars uniformly show 50 ms / 100 µV / 0.1 $\Delta F/F_0$.

4.2.8. Immunohistology

To evaluate the impact caused by the long-term chronic implantation of the Thiol-ene/acrylate device, histology targeting astrocytes (GFAP) and the physiological state of neurons (NeuroTrace) was performed after 80 days of implantation on average, in three mice. Figure 37 shows representative fluorescent images for each marker and the calculated fluorescent intensity of the implanted and contralateral hemisphere, which functioned as primary control. For secondary control, only a glass coverslip was implanted to one subject, without probe implantation. Compared to primary control, there was no significant difference in the intensity and number of cell nuclei (DAPI), while the difference of GFAP intensity was highly significant, indicating that after 10 weeks of implantation, repairing and scarring mechanisms were in progress. The highly significant increase in the intensity of NeuroTrace staining (measured in 2 of 3 mice due to technical difficulties) reflects the consistent high protein synthesis capacity of neuronal cells, as in injured or regenerating neurons, Nissl substance is redistributed around the periphery of the cell body. Secondary controls supported the results of the primary control (Figure 38).

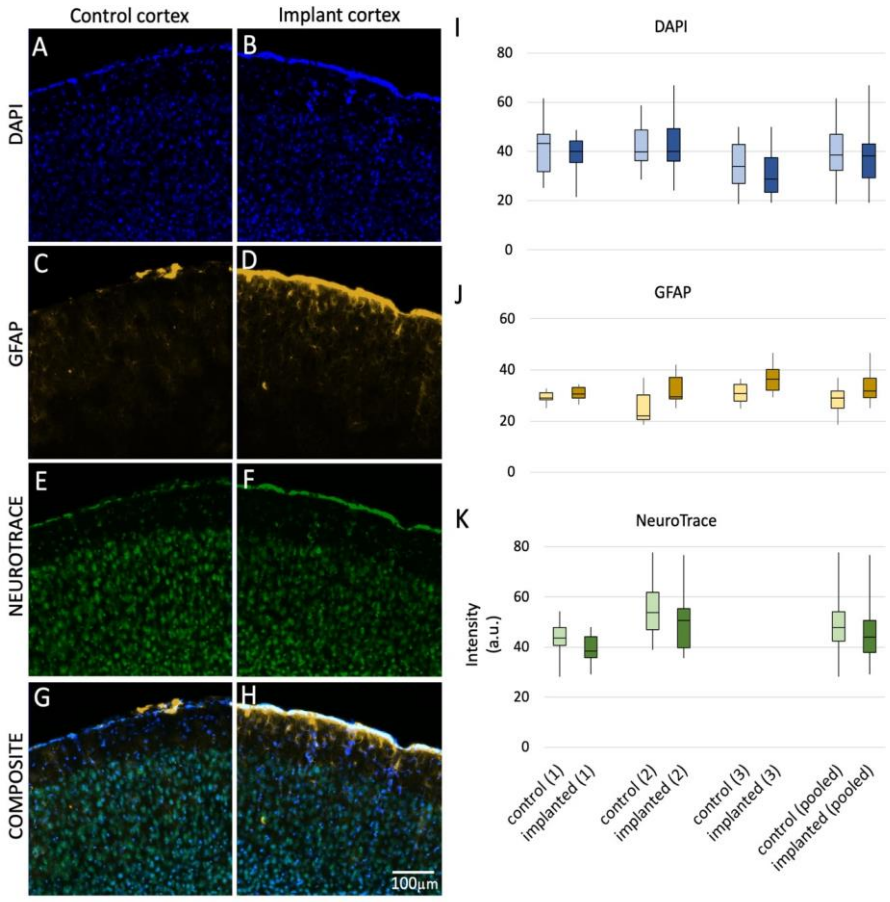

Figure 37. Fluorescent images of Thiol-ene/acrylate *microECoG* implanted brains after 80 days of chronic implantation. Images show layers I–IV of the mouse cortex. (A, B) Cell nuclei stained with DAPI. (C, D) Astrocytes stained with GFAP. (E, F) Neurons stained with NeuroTrace, a fluorescent Nissl stain. (G, H) Composite images of the three stains. (I) Box plots showing minimum, quartiles, mean and maximum of DAPI staining intensity for control and implanted cortices in three subjects and averaged. (J) Same as (I), for GFAP staining. (K) Same as (I), for NeuroTrace staining in 2 subjects.

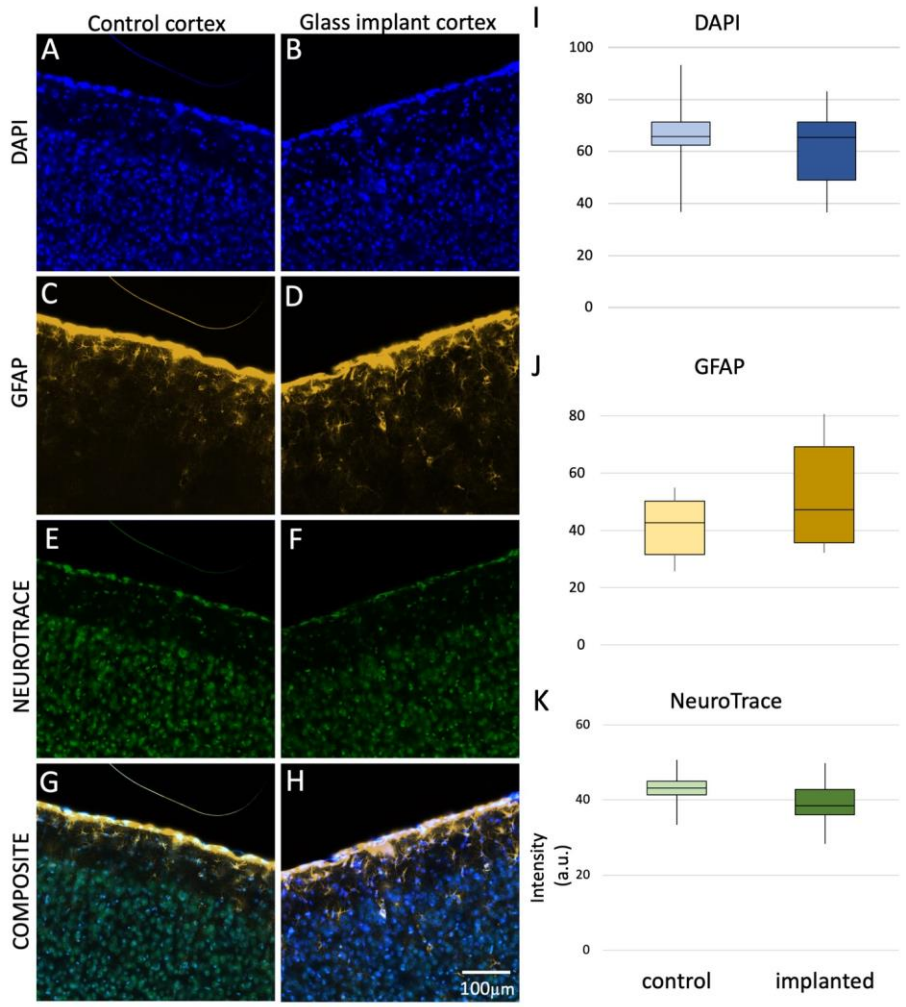

Figure 38. Fluorescent images of immunostaining in a coverglass implanted control subject. (A-H): Images of DAPI (A-B), GFAP (C-D), NeuroTrace (E-F) and composite (G-H) immunostaining. Intensity of DAPI (I), GFAP (J) and NeuroTrace (K) was compared between coverglass implanted and untreated contralateral hemispheres.

We examined the cellular changes following hippocampal implantation as well. The analysis was based on labeling of cell nuclei (DAPI) and astrocytes (GFAP) in six mice. We identified 12 regions of interest (ROIs) beneath the implantation site and in the corresponding area of the opposite hemisphere, which served as our primary control (Figure 39 B-G) for each of the 5 implanted animals included. Additionally, one animal was implanted with a hippocampal adapter alone, without a device, to determine whether the implantation of the electrode caused any additional damage (Figure 39 A). One

implanted animal was excluded from immunohistological evaluation due to early termination without perfusion. Fundamentally, we sought answers to three questions during the analysis: Did the implantation influence the total cell count? Did the CA1 pyramidal layer of the hippocampus, which lay nearly directly beneath the electrode, sustain damage? Did gliotic activity increase due to the implantation? Initially, we compared data from the implanted hemisphere of the five animals with data from the intact hemisphere. In all four animals implanted with electrodes, there was a significant increase in the number of astrocytes ($p = 7.71E{-}14$), correlating with an increase in total cell count ($p = 3.52E{-}09$), and significant cell death was observed in the CA1 pyramidal cells ($p = 2.88E{-}14$). Similar changes were observed in the control animal implanted only with a cylinder, without an electrode ($p = 0.01, 0.04, 0.04$, respectively).

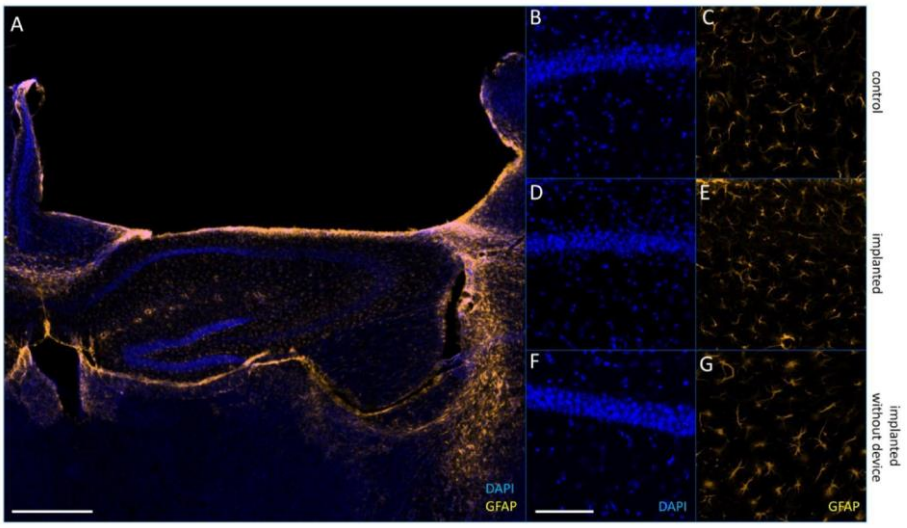

Figure 39. Fluorescent images made after the chronic implantation of shape memory polymer based devices into mouse brains. (A) Fluorescent image of the surgical area without the electrode and the cylinder. Cell nuclei stained with DAPI, astrocytes labeled with GFAP. Scale bar: 0.5 mm, magnification: 4X. (B–D) Magnified (15X) fluorescent ROIs from below the implanted area and the contralateral control hemisphere, also from the control animal (only cylinder implanted). Scale bar: 0.05 mm.

Subsequently, we compared data from the implanted hemisphere of the experimental animals with data from the operated hemisphere of the control animal without an electrode to observe whether electrode implantation enhanced cellular changes. In this

case, contrary to comparison with its own control hemisphere, astrocyte activity significantly decreased (n°1: p = 9.64E−10, n°2: p = 0.01, n°3: p = 0.00022, n°4: 0.0078, n°5: 1.02E−07) and this trend was followed by a significant decrease in total cell count in three out of four animals, though not significantly in two (n°1: p = 2.56E−6, n°2: p = 0.00026, n°3: p = 0.0066, n°4: 0.45, n°5: 0.074). The number of cells counted in the CA1 pyramidal cell layer decreased in all cases except one (animal n°5), of which only one was significant (n°1: p = 0.0011, n°2: p = 0.1, n°3: p = 0.4, n°4: 0.25, n°5: 0.19) (Figure 40).

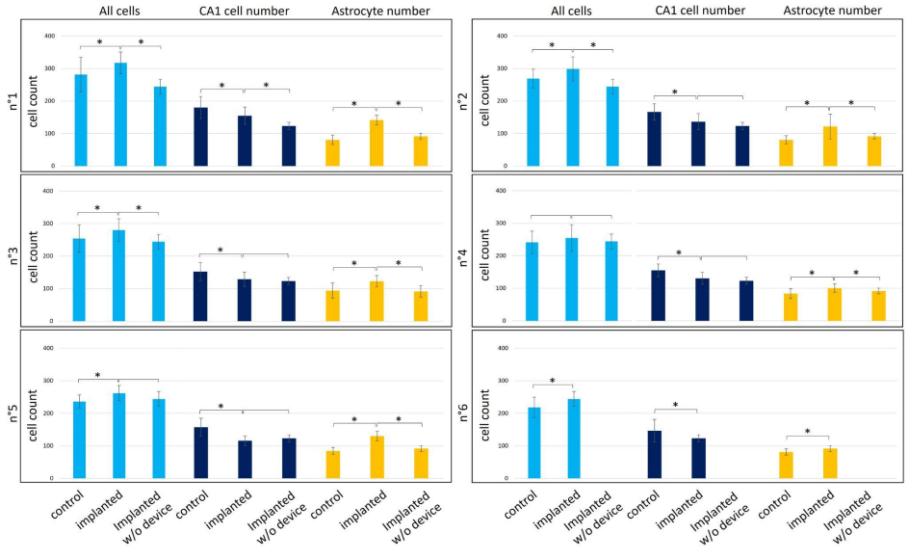

Figure 40. Bar graphs representing data from three cell counting methodologies (total cell count, hippocampal CA1 region cell count, and astrocyte count) are shown, displaying the mean and standard deviation. Error bars represent the standard deviation, and asterisks indicate significant differences where the p-value threshold is <0.05. Data from six different animals (n°1–n°6) are illustrated across six panels; mouse n°6 was not implanted with a device. Each methodology includes data from the control case, which represents the contralateral hemisphere, and the implanted case, representing the electrode-implanted hemisphere. The implanted case is also compared to data from the treated hemisphere of the animal that underwent surgery without device implantation.

5. Discussion

5.1. The applicability of Parylene HT / ITO devices

The goal of this work was to demonstrate the application of the Parylene HT / ITO based transparent microECoG device. Combination of these two materials is not common, however, our study revealed several advantages that maintained the performance of two-photon imaging, when such a device is implanted and located in between the microscope objective and the living tissue.

5.1.1. Mechanical stability of the ITO based device

Parylene HT has the lowest moisture absorption among polymer- based implant materials, which is beneficial due to the decreased risk of delamination due to swelling. Adhesion and potential brittleness of ITO was also addressed experimentally, since there had been concerns about the stability of ITO on flexible substrates [Kwon 2013, Ledochowitsch 2011, Kim 2010]. The cyclic mechanical tests confirmed that ITO forms a reliable conductive layer encapsulated in Parylene HT and is not prone to failure when exposed to bending (Figure 5, Figure 9). The fabrication scheme of the Parylene HT / ITO device is also simple, cost-effective and straightforward, requiring only two photolithography steps, compared to that of graphene for example, that relies on stacking monolayers in complicated steps, which deteriorates uniformity and process reproducibility (Figure 2).

5.1.2. High transparency of substrate and recording sites

The advantage of the current structure relying on Parylene HT / ITO lies in the fact that scan size and quality is not limited by the metallization layer. Fluorescent signals of individual neurons underneath the wires and recording sites can be freely captured with high resolution (Figure 10 E, F; Figure 11; Figure 13 C, D; Figure 15 C, F). The useful surface for neuroimaging through transparent microECoG devices made of graphene [Park 2014, Blaschke 2017] or bilayer-nanomesh [Qiang 2018] structures is usually

limited to the close vicinity of the recording sites, since other non-transparent metal traces (e.g. gold) are used to provide stable interconnection between recording sites and connector pins, and to reduce the overall impedance. The use of ITO without additional metal layers for ECoG recording has been successfully demonstrated for recording purposes earlier [Zátonyi 2018]. The overall optical properties of the final multi-layer structure also make our ECoG superior to other approaches proposed in the related literature. Parylene HT shows transparency greater than 90% between 400–980 nm (Figure 10 B) that is remarkably higher than that of polyimide [Zátonyi 2018] or PET [Ong 2012], slightly higher than that of Parylene C and similar to that of SU-8 substrates [Prajzler 2014] and PDMS [Liu 2015].

5.1.3. Low autofluorescence of Parylene HT

As the principle of two-photon imaging is real-time collection of changes in fluorescence, relatively low autofluorescence of the polymer substrate is also desired to avoid the disturbing background noise. Compared to other substrate materials like polyimide, PDMS, SU-8 or PET, Parylene C is more preferable, due to its lower autofluorescence (Lu 2009, Lu 2010, Walczak 2011), while Parylene HT in turn provide better performance compared to Parylene C, according to our fluorometric measurements in the relevant biological window (Figure 10 A). This is attributable to the strength of the C-F bond compared to the C-H bond, as it is less sensitive to dehydrogenation, consequently the amount of C = C bonds which are responsible for higher autofluorescence remains low under UV illumination [Lu 2010].

5.1.4. Imaging neuronal structures through the device

The spatial resolution of two-photon imaging was compared with microbeads and in vitro hippocampal slices (Figure 10 C). Based on statistical analysis, there was no remarkable difference in measured bead sizes when beads were covered and not covered with the transparent microECoG device. In case of acute brain slices, dendritic structures were clearly identified without significant difference in their dimensions (Figure 10 D-F). It should be noted that the refractive index of Parylene HT (1.55) is higher than that of the

surrounding medium (aCSF or distilled water), which may contribute to the slight differences in the presence of the microECoG device (Liu 2012). These experiments also confirmed that imaging even underneath the ITO recording sites and traces allow high resolution of neuronal structures.

5.1.5. Impedance spectroscopy and accelerated aging

In terms of electrical properties, the accelerated aging test provided valuable indications on device stability (Figure 8). Systematic variation in the impedance magnitude and phase angle at every frequency revealed a more dominant resistive mode of conductivity than on the first day of the accelerated aging test. Since Parylene HT exhibits the lowest permeability to moisture, fluids and gases among Parylene variants (<0.01% water absorption after 24 h — SCS DataSheet), the changes likely occurred at the surface of ITO. Overall, the EIS results predicted stable and acceptable impedance magnitude in the physiological environment to record field potentials in vivo. As expected, the ITO devices demonstrated impedance values in the same range (few hundred kΩ) than the previous Au/PEDOT:PSS nanomesh or graphene devices designed for the same purpose, but with a smaller site diameter [Qiang 2018, Kuzum 2014]. Although the area of our recording sites is slightly larger (0.018 mm^2) to maintain low impedance, two-photon imaging and fluorescence Ca^{2+} imaging through the sites and wiring are still unhindered (Figure 10 C–F).

5.1.6. Characterization of photodegradation and photoelectric artefacts

Besides optical, electrical and mechanical performance of the transparent microECoG device, its integrity under two-photon exposure was also tested (Figure 13 A-D). These tests provided valuable guidelines for future users to avoid damage to either the device or to the tissue (Figure 12). Recommended laser powers were determined for both galvanic and resonant scanning modes at different depths relative to the surface of the device. The results revealed that below the limits of 13 mW in galvanic and 33 mW in resonant scanning mode, direct exposure on the device layer does not cause any visible

degradation. Naturally, the explicit scanning of the surface of the device is generally not the aim in the experimental context, as the usual regions of interest are located well below the superficial layer of the cortex. However, location of ROIs and navigation inside the craniotomy are potentially critical points in this sense. By focusing below the microECoG device by several tens of micrometers, the amount of power could be significantly increased without impairment of the transparent device.

Besides potential photodegradation of the device, light induced artefacts must also be considered when the optimal distance of the focal plane from the device is determined. Electrical artefacts on both ITO and Ti/Au (control) recording sites were quantified during galvanic and resonant scanning with various laser powers and at various distances from the device plane. In general, laser exposure 10 μm below the device plane does not induce apparent noise in the signal, while low power exposure close to the device plane contributes to parasite peaks in the power density spectra, where the fundamental frequency is corresponding to the frame rate of image acquisition (Figure 13 E-H, Figure 14).

5.1.7. Chronic two-photon calcium imaging in awake mice

In vivo two-photon imaging through the proposed device with simultaneous recording of ECoG was arguably the most important test of the microECoG device (Figure 15). Cell bodies and dendrites were clearly visualized up to ~ − 400–500 μm in the cortex, either under the substrate or under ITO wires and recording sites. Since ITO is less transparent than the surrounding Parylene HT, shadowed areas under wires and recording sites crossing the labeled area could influence measurements (Figure 15 B, C). In contrast to this, comparison of neuronal activity under recording sites with the activity of surrounding neurons did not reveal any difference, showing that wires and recording sites do not present a barrier to imaging (Figure 15 D, E, Figure 17). Imaging can be influenced in another aspect as well. Implantation of an added layer between the brain and the cover glasses may give ground to enhanced bone ingrowth and result in less transmittance. However, this was not observed in the implanted mice, as the craniotomy remained clear throughout the imaging period (Figure 15 F). An inherent complication of two-photon imaging combined with electrophysiology is limited space, as implanted electrodes can

block the approach of objectives. Moreover, as a necessity for chronic imaging with the implanted device, the 32 channel connector of the device needed to be fixed to the skull in a way that did not limit freedom of movement for the animals between measurements. This was successfully resolved without complications to two-photon imaging or ECoG recordings, as the flexibility of the device neck allowed the appropriate placement of the connector as well. This ultimately allowed me to perform concurrent ECoG and two-photon calcium imaging (Figure 15 A, D), and verify that our Parylene HT / ITO based microECoG device is a good candidate for large area and high-resolution electrocorticography and simultaneous two-photon calcium imaging for cortical mapping of neuronal ensembles.

5.1.8. Immunohistological responses

Over extended periods of chronic implantation, it is necessary to evaluate the immune response to the implantation of a device and the presence of its material components. Both the biocompatibility of ITO [Selvakumaran 2002, Selvakumaran 2000] and Parylene HT [Meng 2008, Xie 2011, Castagnola 2015, Huang 2008, Cogan 2008] is well supported by both in vitro and in vivo experiments.

The immune response was evaluated with immunohistochemical staining of DAPI, NeuroTrace and GFAP and comparison of neuronal density and cortical thickness 42 to 116 days post implantation (Table 1, Figure 18, 20, 21), in the superficial and deeper layers of the cortex. GFAP labeling, indicative of the astroglial response, recapitulated the described response to cranial surgery [Holtmaat 2009, Koletar 2019]. We found a major increase in its intensity at the shortest time point relative to the control side, more localized to the superficial layers (Figure 19 A). This is in agreement with the described formation of glial scars in the immediate vicinity of implanted devices and shows the higher exposure of superficial layers to surgery induced changes.The relative preservation of deeper layers and the lack of considerable difference between the implanted and control side is promising for imaging of deeper cortical layers long after implantation, and may advocate the adaptation of longer implantation periods in chronic imaging efforts. Regarding the absolute levels of GFAP intensity at different time points, the superficial ROIs of M2-4 were comparable to the highly elevated superficial ROIs of M1 (Figure 19

A). While the statistical testing of this is hindered by the overall number of animals, the causes of this apparent elevation may be speculated. A possible explanation may be an increase in baseline GFAP levels at this implantation time, as the differences between control and implanted sides are preserved.

Changes in cortical thickness or neuronal density may be indicative of an ongoing or concluded immune response and are therefore useful in evaluating the impact caused by the implantation of the device. Although it could be expected that the total width of the cortex would correlate with the neuronal density, the results showed a different picture. Despite unchanged neuronal density in the first two time points, the thickness of the cortex was reduced significantly in M1 and M2-4 (Figure 19 C), while neuron density was lower only in M5, where cortical thickness was actually larger on the implanted side (Figure 19 B).

The evoked immune response encountered here, particularly GFAP and NeuroTrace labeling, is in line with previous reports of immune response after cranial window [Holtmaat 2009] or epidural device implantation [Fedor 2022]. GFAP expression increases 1–2 weeks after surgery ipsilaterally and remains elevated, to a lesser degree, for up to 6 months [Brosch 2020], although there are reports of regained baseline levels [Koletar 2019, Park 2019]. The magnitude of these increases covers a wide range, from 17% [Brosch 2020, Fedor 2022] and 50% [Holtmaat 2009] to 300% [Schweigmann 2021]. In some cases, the reported increase is not quantified [Xu 2007, Guo 2017, Brodnick 2019, Koletar 2019], or the amount of increase is not reported [Park 2019]. Importantly, this agreement with previous reports shows that the implantation of Parylene HT did not evoke an immune response that would exceed the responses evoked by a common craniotomy window surgery.

Softness and flexibility is hypothesized to be an important contributor to the biocompatibility of a device and its effect can be quantified by measuring the depression of the cortex (or cortical thickness) caused by a device [Vomero 2020]. Here, we found that implanted cortices were slightly thinner in the first two implantation lengths, by 32 µm and 23 µm on average respectively, and slightly thicker at the last time point, by 31 µm on average. While the flexibility of Parylene HT is certainly surpassed by shape memory polymers [Fedor 2022] and hydrogel - based devices, its impact here manifests in tens of micrometers on average (Figure 19 C).

It is important to note that the data presented here may be limited by the overall number of implanted mice (Table 1). In particular, the shortest (M1) and longest (M5) implantation lengths had only one mouse examined. While the initial GFAP response after craniotomy, corresponding to M1, is well described, further testing would certainly strengthen the results of the longest implantation period. Nevertheless, the results correspond well to the described effects of cranial implantation surgery [Holtmaat 2009, Schweigmann 2021] and do not suggest an additional, aggravating element introduced by the materials of the ECoG device. Therefore, Parylene HT can be recommended as a stable and biocompatible substrate for chronically implanted transparent neural interfaces.

5.2. The applicability of Thiol-ene/acrylate / SIROF devices

The experiments performed with the Thiole acrylate / SIROF devices were aimed to demonstrate that this transparent microECoG device can be used to concurrently interrogate cortical and hippocampal neuronal populations with ECoG and two-photon calcium imaging (Figure 7). The device was designed specifically for such chronic recordings in awake mice, with the challenges in mind that arise in combined neuroimaging and electrocorticography experiments where a cranial window is also necessary, such as limited space and weight (Figure 3).

5.2.1. Shape memory polymers as substrates

Probes implantable in the rodent brain have been proposed to perform intracortical recordings successfully [Zátonyi 2019, Stiller 2018, Stiller 2020]. Previous research suggests that mechanically compliant neural interfaces that conform better to the curvilinear surface of the brain would be more likely to reduce stress at the biotic–abiotic interface and may mitigate foreign body response [Harris 2011, Lecomte 2018, Jorfi 2015], including studies on SMP substrates [Driscoll 2021, Zátonyi 2019]. Thiol-ene/acrylate compositions have been shown to undergo remarkable changes in elastic properties, softening from over 1 GPa to 300 MPa with less than 3% water uptake upon exposure to PBS at 37 °C. Hovewer, even the low water uptake of Thiol-ene/acrylate necessitated the use of an inner encapsulating layer of Parylene C to prevent short-circuits of the conductive layer. The conductive tracks and their Parylene C capping are located along the neutral axis of the whole multi-layer structure, so the softening behavior of the substrate and its bending stiffness minimally changed. This way, the beneficial mechanical property of the tissue-device interface to foreign body response was exploited, while functionality was maintained even during chronic use. In vitro EIS measurements indicated a uniform decrease in impedance and increase in phase angle (Figure 22, 23), that, together with the equivalent circuit analysis, suggested the diffusion of solvent into the polymer layers [Zátonyi 2019, Takmakov 2015]. This may have undermined the electrophysiological performance of the device except for the additional Parylene C encapsulation (Figure 3 C).

The soft nature of the device was leveraged and validated to great extent in the hippocampal experiments, since the device was folded at 90 degrees at two locations by the silicone cylinder (Figure 7 D). Despite the sharp folds that are suboptimal for handling, the impedance tests and electrode yields showed that the device remained functional until at least seven weeks. This was underlined by the detection of sharp waves in the recorded dataset (Figure 29).

5.2.2. In vivo impedance spectroscopy

In vivo EIS measurements and electrocorticography were carried out weekly with the implanted SIROF based devices of the immunohistology group (Figure 25). Although electrode yield decreased immediately after implantation by 25%, no additional loss of recording sites was observed over the 75-day measurement period (Figure 26). Impedance increased after implantation compared to pre-implantation, most likely in association with acute inflammation, reaching its largest magnitude after 61 days. By the 75th day, impedance magnitude was similar to what was measured after 12 days (Figure 25 A). Long-term electrical stability of an SMP probe softening similarly to our substrate (from 2 Gpa to 300 Mpa) was investigated by Stiller et al., who found that impedance magnitude significantly decreased after 7 weeks but was found to not hinder recording capabilities up to 13 weeks. During that time period, SNR of their device was also maintained [Stiller 2018]. In our study, Thiol-ene/acrylate devices with SIROF (Figure 25 B) or gold-only metallization exhibited similar changes in impedance, while showing a stable SNR during the 22-week long experiment (Figure 27 A-B, Figure 28 A-B). The SNR values are comparable to those of DC sputtered platinum electrodes (SNR = 8.9) on a polyimide microECoG device [Zátonyi 2018]. With the same SNR calculating method, silicon-based arrays were examined [Suner 2005], and a signal quality scale was defined, according to which the Thiol-ene/acrylate / SIROF device would receive a “fair” signal quality. Since this scaling was defined for the higher standards of penetrating electrode arrays, the SNR of our microECoG device is acceptable and appropriate.

5.2.3. Detection of hippocampal sharp wave - ripples

The key hallmark of the hippocampal LFP during immobility, drinking, eating and grooming is the appearance of SPW-Rs, while theta oscillations dominate LFP activity of the walking animal [Buzsáki 2015]. SPW-Rs can arise from any site of the hippocampal CA1 region and propagate along the septotemporal axis depending on ripple magnitude [Patel 2013]. Our recordings from the surface of the dorsal hippocampus further support these statements (Figure 30). A handful of studies reported similar data about the distribution of SPW-Rs as described here, recorded with different electrode types under different conditions (sleep/awake; freely moving/head restrained) and from various species (mice, rats, humans)[Patel 2013, Yitzhak 2021]. In a study using comparable methods by Liu et al. [Liu 2022], the simultaneous recording of SPW-Rs and Ca^{2+} activity with a 16-channel PET / graphene electrode was introduced, describing local and global SPW-R events and corresponding neuronal populations, although their frequency was not addressed. Our dataset provide firm evidence on the feasibility to detect sharp wave ripples in the hippocampus in this experimental scheme (Figure 29, 31) and on the frequency of spatially-restricted (local) and widespread (global) events (Figure 30, 32). This underlines the quality of electrocorticography that can be achieved with the Thiol-ene/acrylate / SIROF device. Taken together, the observed SPW-R incidences found here fit well to those reported in the literature [Buzsáki 2015].

5.2.4. Single unit activity

Although the device was not designed to record single unit activity, we also proved that recording of action potentials is possible at sufficient quality (Table 3, Figure 33). To optimise the performance of SUA recordings using our technology, recording site area, and inter-site distance should be reduced, while channel numbers should be increased [Khodagholy 2014]. A larger density of recording sites will also improve localization of the signal sources within the hippocampus [Tóth 2021], however, high-density arrays also limit the field of view for optical imaging. This trade-off could be partially addressed by the application of transparent wiring based on e.g., indium-tin-oxide [Zátonyi 2020] or PEDOT:PSS [Dijk 2022].

5.2.5. Chronic two-photon calcium imaging

The longevity of two-photon imaging measurements with transparent microECoG devices is an important and often neglected aspect. In the Thiol-ene/acrylate / SIROF implanted mice, neuronal calcium activity in the cortex and in the hippocampus could be measured with two-photon calcium imaging even 22-24 weeks after implantation (Figure 34, 35). This measurement period is considerably longer than for other transparent ECoG devices. Thunemann et al. presented successful multimodal imaging through the PET-based microECoG array in anaesthetized rats [Thunemann 2018]. In the work of Donahue et al., a Parylene C / PEDOT:PSS based device was used to simultaneously monitor pathological activity in the 4-Aminopyridine (4AP) induced acute epilepsy model [Donahue 2018]. Driscoll et al. investigated induced epileptic seizures in acute experiments using a Parylene C / graphene MEA [Driscoll 2021]. Schweigmann et al. used a liquid crystal polymer (LCP)-based array for 28 days to capture GCaMP3 signals of neurons and astrocytes [Schweigmann 2021].

This longevity was reinforced by the quality of calcium signals detected in the *str. pyramidale* of the hippocampus for six months after the implantation (Figure 35 D), simultaneously with sharp wave ripples (Figure 36), and convincingly confirmed our concurrent measurement scheme relying on the use of the Thiol-ene/acrylate / SIROF microECoG device. Through these experiments, facilitated by the improved desing and the softening property of the device, I was able to demonstrate the simultaneous measurement of ECoG and two-photon calcium imaging both in the cortex and the hippocampus of mice.

5.2.6. Immunohistological responses to cortical implantation

In the experiments where the Thiol-ene/acrylate / SIROF devices were implanted over the cortex (Figure 37), we observed an increased GFAP signal in the immunohistochemical staining on the implanted hemisphere compared to the primary control, the contralateral cortical region of the same mouse. The electrode-cortex interface was dominated by $GFAP^+$ astrocytes (Figure 37 D), which indicated that foreign body response may still be in progress 80 days after implantation. There was high protein synthesis made visible by NeuroTrace labeling as well, but no significant difference in DAPI signal intensity. Histology from a secondary control, coverglass implanted mouse

suggested that these changes are likely not due to the presence of the device. The increase in astrocyte activity and protein synthesis may instead be due to the surgical procedure (e.g., removal of dura mater) and the use of coverglass as a substitute of skull bone (Figure 38). Our findings are in good agreement with the work of Saxena et al., who found the same high appearance of GFAP astrocytes at the electrode-cortex interface 16 weeks post-implantation in rats [Saxena 2013]. Moreover, Ravikumar et al. found that GFAP immunoreactivity was the highest at 2 and 16 weeks post-implantation in mice but concluded that they did not find any correlation between neurodegeneration and activated microglia [Ravikumar 2014].

5.2.7. Immunohistological responses to hippocampal implantation

Immunohistochemical examination of the hippocampal implantations revealed that the implantation of the electrode caused significant cellular changes in the brains of the examined mice following approximately six months of chronic implantation (Figure 39 Figure 40). In terms of the effect of electrode implantation surgery, it was associated with increased gliotic activity and a decrease in cell population in the hippocampal CA1 region. When comparing surgery with and without implantation, no significant difference was observed in the total number of cells and the changes in the CA1 region. However, it can be stated that during surgery without implantation, astrocyte activity was significantly lower. Although gliotic activity increased, gliotic scar tissue did not develop during the observed period, which would have isolated the electrode from the brain tissue, thus the quality of the measurements could have been maintained. Furthermore, the fact that gliotic activity increased when compared in all of the cases when comparing with the contralateral hemisphere, leads back to the conclusion that the surgical procedure greatly influences cellular organisation, and the changes observed are not solely caused by the implantation of the Thiol-ene/acrylate microECoG devices.

Our study highlighted the first successful chronic application of a softening microECoG device incorporated in a hippocampal cranial chamber to record sharp wave-ripples and action potentials, while facilitating optical access to measure calcium signals through the transparent substrate layer. The chronically implanted shape memory polymer based device provided stable electrophysiological signals from the surface of the dorsal

hippocampus, including SPW-Rs and MUAs/SUAs, for several weeks with preserved transparency for two-photon imaging up to six months in GCaMP6f expressing transgenic mice. These valuable features make the presented Thiol-ene/acrylate / SIROF device a strong candidate for future studies where long term electrophysiological monitoring and simultaneous calcium imaging might support discoveries, such as in epilepsy research or drug development for neurodegenerative diseases

6. Conclusions

In my thesis, I introduced a transparent microECoG device composed of Parylene HT / ITO and presented its first use in chronic, simultaneous ECoG and two-photon calcium imaging experiments in awake mice. The device is simple, cost-effective and straightforward to fabricate, its recording sites exhibit impedance in the range of a few hundred kΩ-s and compatible with two-photon imaging as demonstrated by our experiments aimed at photovoltaic effects and photodamage. In vivo two-photon imaging and combined ECoG recordings demonstrated that cell bodies and dendrites were clearly visualized at −250 μm (Figure) and up to −400 μm in the cortex, either under the polymer layer or under wires and recording sites. In line with previous reports of immune responses after cranial surgery [Holtmaat 2009, Schweigmann 2021], we encountered increased GFAP and NeuroTrace labeling. We conclude that these changes do not suggest an additional, aggravating element introduced by the materials of the microECoG device, and recommend Parylene HT as a stable and biocompatible substrate for chronically implanted transparent neural interfaces.

In the second part of my thesis, I introduced a microECoG device featuring the shape memory polymer Thiol-ene/acrylate as an encapsulating substrate and gold/SIROF conductive layers. The device was designed specifically for chronic recordings in awake mice, with the challenges in mind that arise in combined neuroimaging and electrocorticography experiments. Excellent recording quality was reflected throughout the course of the experiment by high SNR, impedance in the range of several hundred kΩ-s, detection of hippocampal sharp wave – ripple events and the recording of single-unit activity. This underlines the quality of electrophysiology that can be achieved with the Thiol-ene/acrylate / SIROF microECoG devices. The optical performance of these devices satisfied the requirements of chronic experiments aiming for the synergetic use of two-photon microscopy and cortical electrophysiology. Cortical measurements of two-photon calcium imaging were performed up to 22 weeks atfer implantation of the device, a period that is considerably longer than for other transparent microECoG devices. In the *str. pyramidale* of the hippocampus, we recorded neuronal level calcium events simultaneously with sharp wave – ripples, confirming the parallel use of the Thiol-

ene/acrylate microECoG device. Although histological evaluation indicated increased GFAP levels in both cortically and hippocampally implanted mice, histology of secondary control, coverglass implanted mice as well as data in the literature suggested that the surgical procedure greatly influences cellular organisation, and the changes observed in implanted mice are unlikely to be caused solely by the implantation of the Thiol-ene/acrylate / SIROF microECoG device.

7. Summary

Through extensive characterization and experiments in vitro and in vivo in awake mice, we sought to validate the usability of the Parylene HT/ ITO and Thiol-ene/acrylate / SIROF composed transparent, implantable ECoG devices in two-photon imaging experiments. We introduced novel material compositions and device designs and subjected those devices to many tests, covering particularly electrochemical properties, transparency and rigidity. In vitro tests on acute mouse brain slices served as a middle ground towards in vivo experiments, and we explored the optical characteristics, photothermal and photoelectric effects on the devices more in depth. As our main goal, we implanted these transparent devices in mice, both on the cortical and the hippocampal surface, for use in two-photon imaging and validated the in vivo, long term performance of ECoG and calcium imaging, the basis of concurrent measurements. Finally, we characterized the histological context of the implantations with DAPI, GFAP and NeuroTrace labelings at different time points post implantation.

The results of all of these tests point out conclusively the applicability of both Parylene HT/ ITO and Thiol-ene/acrylate / SIROF composed devices in concurrent ECoG and two-photon calcium imaging experiments in awake mice. The devices possess excellent optical transparency. Electrochemical properties reflected the material choices in the devices' design and allowed good quality recordings months after implantation with minimal loss of recording sites. Two-photon calcium imaging of GCaMP6f labelled cortical neurons through the implanted devices provided satisfactory data on the activity of neuronal populations 51 days (Parylene HT / ITO) and 22 weeks (Thiol-ene/acrylate / SIROF) after implantation. Last but not least, the use of shape memory polymer materials supported the implantation of the devices and the tackling of the following immune response by conforming to the cortical surface better.

In light of these experiments we concluded that the implantable devices introduced here are suitable for combined electrocorticography and two - photon calcium imaging chronically, in awake mice and are good candidates for cellular level resolution mapping of neuronal ensembles with electrophysiology and simultaneous two-photon imaging.

8. References

Alahi, M. E. E., Liu, Y., Xu, Z., Wang, H., Wu, T., & Mukhopadhyay, S. C. (2021). Recent advancement of electrocorticography (ECoG) electrodes for chronic neural recording/stimulation. In *Materials Today Communications* (Vol. 29). https://doi.org/10.1016/j.mtcomm.2021.102853

Atherton, T. J., & Kerbyson, D. J. (1999). Size invariant circle detection. *Image and Vision Computing*, *17*(11), 795–803. https://doi.org/10.1016/S0262-8856(98)00160-7

Baek, D.-H., Lee, J., Byeon, H. jin, Choi, H., Young Kim, I., Lee, K.-M., Jungho Pak, J., Pyo Jang, D., & Lee, S.-H. (2014). A thin film polyimide mesh microelectrode for chronic epidural electrocorticography recording with enhanced contactability. *Journal of Neural Engineering*, *11*(4), 046023. https://doi.org/10.1088/1741-2560/11/4/046023

Baumgartner, C., & Koren, J. P. (2018). Seizure detection using scalp- <scp>EEG</scp>. *Epilepsia*, *59*(S1), 14–22. https://doi.org/10.1111/epi.14052

Bédard, C., & Destexhe, A. (2012). Local field potentials. In *Handbook of Neural Activity Measurement* (pp. 136–191). Cambridge University Press. https://doi.org/10.1017/CBO9780511979958.005

Bérces, Z., Tóth, K., Márton, G., Pál, I., Kováts-Megyesi, B., Fekete, Z., Ulbert, I., & Pongrácz, A. (2016). Neurobiochemical changes in the vicinity of a nanostructured neural implant. *Scientific Reports*, *6*. https://doi.org/10.1038/srep35944

Bhunia, Swarup., Majerus, Steve., & Sawan, Mohamad. (2015). *Implantable biomedical microsystems : design principles and applications*. William Andrew, an imprint of Elsevier.

Black, B. J., Ecker, M., Stiller, A., Rihani, R., Danda, V. R., Reed, I., Voit, W. E., & Pancrazio, J. J. (2018). In vitro compatibility testing of thiol-ene/acrylate-based shape memory polymers for use in implantable neural interfaces. *Journal of Biomedical Materials Research - Part A*, *106*(11). https://doi.org/10.1002/jbm.a.36478

Blaschke, B. M., Tort-Colet, N., Guimerà-Brunet, A., Weinert, J., Rousseau, L., Heimann, A., Drieschner, S., Kempski, O., Villa, R., Sanchez-Vives, M. v, & Garrido, J.

A. (2017). Mapping brain activity with flexible graphene micro-transistors. *2D Materials*, *4*(2), 025040. https://doi.org/10.1088/2053-1583/aa5eff

Blumenthal, N. R., Petravicz, J. C., Breton-Provencher, V., Hu, M., Riemenschneider, F., Sarem, M., Sur, M., & Shastri, V. P. (2025). Stochastic Nanoroughness Inhibits and Reverses Glial Scarring In Vitro and In Vivo via a Mechanobiology Paradigm Involving Piezo-1. *Advanced Functional Materials*, *35*(1). https://doi.org/10.1002/adfm.202411965

Branco, M. P., Geukes, S. H., Aarnoutse, E. J., Ramsey, N. F., & Vansteensel, M. J. (2023). Nine decades of electrocorticography: A comparison between epidural and subdural recordings. *European Journal of Neuroscience*, *57*(8), 1260–1288. https://doi.org/10.1111/ejn.15941

Buccino, A. P., Hurwitz, C. L., Garcia, S., Magland, J., Siegle, J. H., Hurwitz, R., & Hennig, M. H. (2020). SpikeInterface, a unified framework for spike sorting. *ELife*, *9*. https://doi.org/10.7554/eLife.61834

Burle, B., Spieser, L., Roger, C., Casini, L., Hasbroucq, T., & Vidal, F. (2015). Spatial and temporal resolutions of EEG: Is it really black and white? A scalp current density view. *International Journal of Psychophysiology*, *97*(3). https://doi.org/10.1016/j.ijpsycho.2015.05.004

Buzsáki, G., & Wang, X.-J. (2012a). Mechanisms of Gamma Oscillations. *Annual Review of Neuroscience*, *35*(1), 203–225. https://doi.org/10.1146/annurev-neuro-062111-150444

Buzsáki, G., Anastassiou, C. A., & Koch, C. (2012b). The origin of extracellular fields and currents-EEG, ECoG, LFP and spikes. In *Nature Reviews Neuroscience* (Vol. 13, Issue 6). https://doi.org/10.1038/nrn3241

Campbell, A., & Wu, C. (2018). Chronically implanted intracranial electrodes: Tissue reaction and electrical changes. In *Micromachines* (Vol. 9, Issue 9). https://doi.org/10.3390/mi9090430

Castagnola, V., Descamps, E., Lecestre, A., Dahan, L., Remaud, J., Nowak, L. G., & Bergaud, C. (2015). Parylene-based flexible neural probes with PEDOT coated surface for brain stimulation and recording. *Biosensors and Bioelectronics*, *67*. https://doi.org/10.1016/j.bios.2014.09.004

Degenhart, A. D., Eles, J., Dum, R., Mischel, J. L., Smalianchuk, I., Endler, B., Ashmore, R. C., Tyler-Kabara, E. C., Hatsopoulos, N. G., Wang, W., Batista, A. P., & Cui, X. T. (2016). Histological evaluation of a chronically-implanted electrocorticographic electrode grid in a non-human primate. *Journal of Neural Engineering*, *13*(4). https://doi.org/10.1088/1741-2560/13/4/046019

Dijk, G., Kaszas, A., Pas, J., & O'Connor, R. P. (2022). Fabrication and in vivo 2-photon microscopy validation of transparent PEDOT:PSS microelectrode arrays. *Microsystems & Nanoengineering*, *8*(1), 90. https://doi.org/10.1038/s41378-022-00434-7

Donahue, M. J., Kaszas, A., Turi, G. F., Rózsa, B., Slézia, A., Vanzetta, I., Katona, G., Bernard, C., Malliaras, G. G., & Williamson, A. (2018). Multimodal characterization of neural networks using highly transparent electrode arrays. *ENeuro*, *5*(6). https://doi.org/10.1523/ENEURO.0187-18.2018

Driscoll, N., Rosch, R. E., Murphy, B. B., Ashourvan, A., Vishnubhotla, R., Dickens, O. O., Johnson, A. T. C., Davis, K. A., Litt, B., Bassett, D. S., Takano, H., & Vitale, F. (2021). Multimodal in vivo recording using transparent graphene microelectrodes illuminates spatiotemporal seizure dynamics at the microscale. *Communications Biology*, *4*(1). https://doi.org/10.1038/s42003-021-01670-9

Einevoll, G. T., Kayser, C., Logothetis, N. K., & Panzeri, S. (2013). Modelling and analysis of local field potentials for studying the function of cortical circuits. *Nature Reviews Neuroscience*, *14*(11), 770–785. https://doi.org/10.1038/nrn3599

Feidenhans'l, N. A., Lafleur, J. P., Jensen, T. G., & Kutter, J. P. (2014). Surface functionalized thiol-ene waveguides for fluorescence biosensing in microfluidic devices. *ELECTROPHORESIS*, *35*(2–3), 282–288. https://doi.org/10.1002/elps.201300271

Fekete, Z., & Pongrácz, A. (2017). Multifunctional soft implants to monitor and control neural activity in the central and peripheral nervous system: A review. In *Sensors and Actuators, B: Chemical* (Vol. 243). https://doi.org/10.1016/j.snb.2016.12.096

Franklin, K. B. J. ., & Paxinos, George. (2013). *Paxinos and Franklin's The mouse brain in stereotaxic coordinates*. Academic Press, an imprint of Elsevier.

Frewin, C. L., Ecker, M., Joshi-Imre, A., Kamgue, J., Waddell, J., Danda, V. R., Stiller, A. M., Voit, W. E., & Pancrazio, J. J. (2019). Electrical Properties of Thiol-ene-based

Shape Memory Polymers Intended for Flexible Electronics. *Polymers*, *11*(5), 902. https://doi.org/10.3390/polym11050902

Frewin, C. L., Ecker, M., Joshi-Imre, A., Kamgue, J., Waddell, J., Danda, V. R., Stiller, A. M., Voit, W. E., & Pancrazio, J. J. (2019). Electrical Properties of Thiol-ene-based Shape Memory Polymers Intended for Flexible Electronics. *Polymers*, *11*(5), 902. https://doi.org/10.3390/polym11050902

Furukawa, Y., Shimada, A., Kato, K., Iwata, H., & Torimitsu, K. (2013). Monitoring neural stem cell differentiation using PEDOT–PSS based MEA. *Biochimica et Biophysica Acta (BBA) - General Subjects*, *1830*(9), 4329–4333. https://doi.org/10.1016/j.bbagen.2013.01.022

Gallego-Carracedo, C., Perich, M. G., Chowdhury, R. H., Miller, L. E., & Gallego, J. Á. (2022). Local field potentials reflect cortical population dynamics in a region-specific and frequency-dependent manner. *ELife*, *11*. https://doi.org/10.7554/eLife.73155

Gilletti, A., & Muthuswamy, J. (2006). Brain micromotion around implants in the rodent somatosensory cortex. *Journal of Neural Engineering*, *3*(3). https://doi.org/10.1088/1741-2560/3/3/001

Goel, K., Pek, V., Shlobin, N. A., Chen, J., Wang, A., Ibrahim, G. M., Hadjinicolaou, A., Roessler, K., Dudley, R. W., Nguyen, D. K., El-Tahry, R., Fallah, A., & Weil, A. G. (2023). Clinical utility of intraoperative electrocorticography for epilepsy surgery: A systematic review and meta-analysis. *Epilepsia*, *64*(2), 253–265. https://doi.org/10.1111/epi.17472

Gong, S., Zhao, Y., Yap, L. W., Shi, Q., Wang, Y., Bay, J. A. P. B., Lai, D. T. H., Uddin, H., & Cheng, W. (2016). Fabrication of Highly Transparent and Flexible NanoMesh Electrode via Self-assembly of Ultrathin Gold Nanowires. *Advanced Electronic Materials*, *2*(7). https://doi.org/10.1002/aelm.201600121

Granqvist, C. G., & Hultåker, A. (2002). Transparent and conducting ITO films: new developments and applications. *Thin Solid Films*, *411*(1), 1–5. https://doi.org/10.1016/S0040-6090(02)00163-3

Grewal, S. S., Alvi, M. A., Perkins, W. J., Cascino, G. D., Britton, J. W., Burkholder, D. B., So, E., Shin, C., Marsh, R. W., Meyer, F. B., Worrell, G. A., & van Gompel, J. J.

(2020). Reassessing the impact of intraoperative electrocorticography on postoperative outcome of patients undergoing standard temporal lobectomy for MRI-negative temporal lobe epilepsy. *Journal of Neurosurgery*, *132*(2), 605–614. https://doi.org/10.3171/2018.11.JNS182124

Grienberger, C., Giovannucci, A., Zeiger, W., & Portera-Cailliau, C. (2022). Two-photon calcium imaging of neuronal activity. *Nature Reviews Methods Primers*, *2*(1), 67. https://doi.org/10.1038/s43586-022-00147-1

Hales, C. G., & Pockett, S. (2014). The relationship between local field potentials (LFPs) and the electromagnetic fields that give rise to them. *Frontiers in Systems Neuroscience*, *8*. https://doi.org/10.3389/fnsys.2014.00233

Han, X. (2012). In Vivo Application of Optogenetics for Neural Circuit Analysis. *ACS Chemical Neuroscience*, *3*(8), 577–584. https://doi.org/10.1021/cn300065j

Harris, J. P., Capadona, J. R., Miller, R. H., Healy, B. C., Shanmuganathan, K., Rowan, S. J., Weder, C., & Tyler, D. J. (2011). Mechanically adaptive intracortical implants improve the proximity of neuronal cell bodies. *Journal of Neural Engineering*, *8*(6). https://doi.org/10.1088/1741-2560/8/6/066011

Hébert, C., Masvidal-Codina, E., Suarez-Perez, A., Calia, A. B., Piret, G., Garcia-Cortadella, R., Illa, X., del Corro Garcia, E., de la Cruz Sanchez, J. M., Casals, D. V., Prats-Alfonso, E., Bousquet, J., Godignon, P., Yvert, B., Villa, R., Sanchez-Vives, M. v., Guimerà-Brunet, A., & Garrido, J. A. (2018). Flexible Graphene Solution-Gated Field-Effect Transistors: Efficient Transducers for Micro-Electrocorticography. *Advanced Functional Materials*, *28*(12). https://doi.org/10.1002/adfm.201703976

Hébert, C., Masvidal-Codina, E., Suarez-Perez, A., Calia, A. B., Piret, G., Garcia-Cortadella, R., Illa, X., del Corro Garcia, E., de la Cruz Sanchez, J. M., Casals, D. V., Prats-Alfonso, E., Bousquet, J., Godignon, P., Yvert, B., Villa, R., Sanchez-Vives, M. v., Guimerà-Brunet, A., & Garrido, J. A. (2018). Flexible Graphene Solution-Gated Field-Effect Transistors: Efficient Transducers for Micro-Electrocorticography. *Advanced Functional Materials*, *28*(12). https://doi.org/10.1002/adfm.201703976

Helmchen, F. (2009). *In vivo optical imaging of brain function*. CRC Press/Taylor & Francis. https://www.ncbi.nlm.nih.gov/pubmed/26844314

Herreras, O. (2016). Local Field Potentials: Myths and Misunderstandings. *Frontiers in Neural Circuits*, *10*. https://doi.org/10.3389/fncir.2016.00101

Herreras, O., Torres, D., Makarov, V. A., & Makarova, J. (2023). Theoretical considerations and supporting evidence for the primary role of source geometry on field potential amplitude and spatial extent. *Frontiers in Cellular Neuroscience*, *17*. https://doi.org/10.3389/fncel.2023.1129097

Hillman, E. M. C. (2007). Optical brain imaging in vivo: techniques and applications from animal to man. *Journal of Biomedical Optics*, *12*(5). https://doi.org/10.1117/1.2789693

Hillman, E. M. C. (2014). Coupling Mechanism and Significance of the BOLD Signal: A Status Report. *Annual Review of Neuroscience*, *37*(1), 161–181. https://doi.org/10.1146/annurev-neuro-071013-014111

Hollenberg, B. A., Richards, C. D., Richards, R., Bahr, D. F., & Rector, D. M. (2006). A MEMS fabricated flexible electrode array for recording surface field potentials. *Journal of Neuroscience Methods*, *153*(1). https://doi.org/10.1016/j.jneumeth.2005.10.016

Hotson, G., McMullen, D. P., Fifer, M. S., Johannes, M. S., Katyal, K. D., Para, M. P., Armiger, R., Anderson, W. S., Thakor, N. v., Wester, B. A., & Crone, N. E. (2016). Individual finger control of a modular prosthetic limb using high-density electrocorticography in a human subject. *Journal of Neural Engineering*, *13*(2). https://doi.org/10.1088/1741-2560/13/2/026017

Hu, J., Hossain, R. F., Navabi, Z. S., Tillery, A., Laroque, M., Donaldson, P. D., Swisher, S. L., & Kodandaramaiah, S. B. (2023). Fully desktop fabricated flexible graphene electrocorticography (ECoG) arrays. *Journal of Neural Engineering*, *20*(1), 016019. https://doi.org/10.1088/1741-2552/acae08

Huang, D.-Y., & Wang, C.-H. (2009). Optimal multi-level thresholding using a two-stage Otsu optimization approach. *Pattern Recognition Letters*, *30*(3), 275–284. https://doi.org/10.1016/j.patrec.2008.10.003

Hukins, D. W. L., Mahomed, A., & Kukureka, S. N. (2008). Accelerated aging for testing polymeric biomaterials and medical devices. *Medical Engineering and Physics*, *30*(10). https://doi.org/10.1016/j.medengphy.2008.06.001

Jorcin, J. B., Orazem, M. E., Pébère, N., & Tribollet, B. (2006). CPE analysis by local electrochemical impedance spectroscopy. *Electrochimica Acta*, *51*(8–9). https://doi.org/10.1016/j.electacta.2005.02.128

Jorfi, M., Skousen, J. L., Weder, C., & Capadona, J. R. (2015). Progress towards biocompatible intracortical microelectrodes for neural interfacing applications. In *Journal of Neural Engineering* (Vol. 12, Issue 1). https://doi.org/10.1088/1741-2560/12/1/011001

Judák, L., Chiovini, B., Juhász, G., Pálfi, D., Mezriczky, Z., Szadai, Z., Katona, G., Szmola, B., Ócsai, K., Martinecz, B., Mihály, A., Dénes, Á., Kerekes, B., Szepesi, Á., Szalay, G., Ulbert, I., Mucsi, Z., Roska, B., & Rózsa, B. (2022). Sharp-wave ripple doublets induce complex dendritic spikes in parvalbumin interneurons in vivo. *Nature Communications*, *13*(1), 6715. https://doi.org/10.1038/s41467-022-34520-1

Kajikawa, Y., & Schroeder, C. E. (2011). How local is the local field potential? *Neuron*, *72*(5), 847–858. https://doi.org/10.1016/j.neuron.2011.09.029

Khodagholy, D., Gelinas, J. N., Thesen, T., Doyle, W., Devinsky, O., Malliaras, G. G., & Buzsáki, G. (2015). NeuroGrid: Recording action potentials from the surface of the brain. *Nature Neuroscience*, *18*(2). https://doi.org/10.1038/nn.3905

Kim, C., Jeong, J., & Kim, S. J. (2019). Recent progress on non-conventional microfabricated probes for the chronic recording of cortical neural activity. In *Sensors (Switzerland)* (Vol. 19, Issue 5). https://doi.org/10.3390/s19051069

Kim, E.-H., Yang, C.-W., & Park, J.-W. (2010). Improving the delamination resistance of indium tin oxide (ITO) coatings on polymeric substrates by O2 plasma surface treatment. *Current Applied Physics*, *10*(3), S510–S514. https://doi.org/10.1016/j.cap.2009.12.028

Kim, J., Wilson, J. A., & Williams, J. C. (2007). A cortical recording platform utilizing microECoG electrode arrays. *Conference Proceedings : ... Annual International Conference of the IEEE Engineering in Medicine and Biology Society. IEEE Engineering in Medicine and Biology Society. Conference*.

Kim, Y., Alimperti, S., Choi, P., & Noh, M. (2022). An Inkjet Printed Flexible Electrocorticography (ECoG) Microelectrode Array on a Thin Parylene-C Film. *Sensors*, *22*(3), 1277. https://doi.org/10.3390/s22031277

Konerding, W. S., Froriep, U. P., Kral, A., & Baumhoff, P. (2018). New thin-film surface electrode array enables brain mapping with high spatial acuity in rodents. *Scientific Reports*, *8*(1). https://doi.org/10.1038/s41598-018-22051-z

Kunori, N., & Takashima, I. (2015). A transparent epidural electrode array for use in conjunction with optical imaging. *Journal of Neuroscience Methods*, *251*. https://doi.org/10.1016/j.jneumeth.2015.05.018

Kuzum, D., Takano, H., Shim, E., Reed, J. C., Juul, H., Richardson, A. G., de Vries, J., Bink, H., Dichter, M. A., Lucas, T. H., Coulter, D. A., Cubukcu, E., & Litt, B. (2014). Transparent and flexible low noise graphene electrodes for simultaneous electrophysiology and neuroimaging. *Nature Communications*, *5*. https://doi.org/10.1038/ncomms6259

Kwon, K. Y., Aviyente, S., & Li, W. (2013). Investigation of phase-locked neuronal oscillation with optical stimulation based on a time-frequency approach. *International IEEE/EMBS Conference on Neural Engineering, NER*. https://doi.org/10.1109/NER.2013.6695962

Kwon, K. Y., Sirowatka, B., Weber, A., & Li, W. (2013). Opto-μECoG Array: A Hybrid Neural Interface With Transparent μECoG Electrode Array and Integrated LEDs for Optogenetics. *IEEE Transactions on Biomedical Circuits and Systems*, *7*(5), 593–600. https://doi.org/10.1109/TBCAS.2013.2282318

Lecomte, A., Degache, A., Descamps, E., Dahan, L., & Bergaud, C. (2017). In vitro and in vivo biostability assessment of chronically-implanted Parylene C neural sensors. *Sensors and Actuators B: Chemical*, *251*, 1001–1008. https://doi.org/10.1016/j.snb.2017.05.057

Lecomte, A., Descamps, E., & Bergaud, C. (2018). A review on mechanical considerations for chronically-implanted neural probes. In *Journal of Neural Engineering* (Vol. 15, Issue 3). https://doi.org/10.1088/1741-2552/aa8b4f

Lecomte, A., Descamps, E., & Bergaud, C. (2018). A review on mechanical considerations for chronically-implanted neural probes. In *Journal of Neural Engineering* (Vol. 15, Issue 3). https://doi.org/10.1088/1741-2552/aa8b4f

Lecoq, J., Orlova, N., & Grewe, B. F. (2019). Wide. Fast. Deep: Recent advances in multiphoton microscopy of in vivo neuronal activity. *Journal of Neuroscience*, *39*(46). https://doi.org/10.1523/JNEUROSCI.1527-18.2019

Ledochowitsch, P., Olivero, E., Blanche, T., & Maharbiz, M. M. (2011). A transparent μECoG array for simultaneous recording and optogenetic stimulation. *2011 Annual International Conference of the IEEE Engineering in Medicine and Biology Society*, 2937–2940. https://doi.org/10.1109/IEMBS.2011.6090808

Ledochowitsch, P., Olivero, E., Blanche, T., & Maharbiz, M. M. (2011). A transparent μECoG array for simultaneous recording and optogenetic stimulation. *2011 Annual International Conference of the IEEE Engineering in Medicine and Biology Society*, 2937–2940. https://doi.org/10.1109/IEMBS.2011.6090808

Li, G. L., Wu, J. T., Xia, Y. H., He, Q. G., & Jin, H. G. (2020). Review of semi-dry electrodes for EEG recording. In *Journal of Neural Engineering* (Vol. 17, Issue 5). https://doi.org/10.1088/1741-2552/abbd50

Li, G., Wang, S., & Duan, Y. Y. (2018). Towards conductive-gel-free electrodes: Understanding the wet electrode, semi-dry electrode and dry electrode-skin interface impedance using electrochemical impedance spectroscopy fitting. *Sensors and Actuators B: Chemical*, *277*, 250–260. https://doi.org/10.1016/j.snb.2018.08.155

Li, G., Wang, S., Li, M., & Duan, Y. Y. (2021). Towards real-life EEG applications: novel superporous hydrogel-based semi-dry EEG electrodes enabling automatically 'charge–discharge' electrolyte. *Journal of Neural Engineering*, *18*(4), 046016. https://doi.org/10.1088/1741-2552/abeeab

Liu, J., Zong, G., He, L., Zhang, Y., Liu, C., & Wang, L. (2015). Effects of fumed and mesoporous silica nanoparticles on the properties of sylgard 184 polydimethylsiloxane. *Micromachines*, *6*(7). https://doi.org/10.3390/mi6070855

Liu, X., Terada, S., Ramezani, M., Kim, J. H., Lu, Y., Grosmark, A., Losonczy, A., & Kuzum, D. (2022). E-Cannula reveals anatomical diversity in sharp-wave ripples as a

driver for the recruitment of distinct hippocampal assemblies. *Cell Reports*, *41*(1). https://doi.org/10.1016/j.celrep.2022.111453

Liu, Y., Zhang, C., & Wang, L. v. (2012). Effects of light scattering on optical-resolution photoacoustic microscopy. *Journal of Biomedical Optics*, *17*(12), 126014. https://doi.org/10.1117/1.JBO.17.12.126014

Lu, B., Zheng, S., & Tai, Y. C. (2009). Parylene background fluorescence study for biomems applications. *TRANSDUCERS 2009 - 15th International Conference on Solid-State Sensors, Actuators and Microsystems*. https://doi.org/10.1109/SENSOR.2009.5285534

Lu, B., Zheng, S., Quach, B. Q., & Tai, Y. C. (2010). A study of the autofluorescence of parylene materials for μtAS applications. *Lab on a Chip*, *10*(14). https://doi.org/10.1039/b924855b

Lu, Y., Liu, X., Hattori, R., Ren, C., Zhang, X., Komiyama, T., & Kuzum, D. (2018). Ultralow Impedance Graphene Microelectrodes with High Optical Transparency for Simultaneous Deep Two-Photon Imaging in Transgenic Mice. *Advanced Functional Materials*, *28*(31). https://doi.org/10.1002/adfm.201800002

Malvache, A., Reichinnek, S., Villette, V., Haimerl, C., & Cossart, R. (2016). Awake hippocampal reactivations project onto orthogonal neuronal assemblies. *Science*, *353*(6305), 1280–1283. https://doi.org/10.1126/science.aaf3319

Marin, C. (2010). Biocompatibility of intracortical microelectrodes: current status and future prospects. *Frontier in Neuroengineering*, *3*. https://doi.org/10.3389/fneng.2010.00008

Márton, G., Orbán, G., Kiss, M., Fiáth, R., Pongrácz, A., & Ulbert, I. (2015). A multimodal, SU-8 - Platinum - Polyimide microelectrode array for chronic in vivo neurophysiology. *PLoS ONE*, *10*(12). https://doi.org/10.1371/journal.pone.0145307

Matelli, M., Luppino, G., & Rizzolatti, G. (1991). Architecture of superior and mesial area 6 and the adjacent cingulate cortex in the macaque monkey. *Journal of Comparative Neurology*, *311*(4). https://doi.org/10.1002/cne.903110402

Mazzoni, A., Logothetis, N. K., & Panzeri, S. (2012). *The information content of Local Field Potentials: experiments and models*.

Miller, K. J., Hermes, D., & Staff, N. P. (2020). The current state of electrocorticography-based brain–computer interfaces. *Neurosurgical Focus*, *49*(1), E2. https://doi.org/10.3171/2020.4.FOCUS20185

Minami, T. (2008). Substitution of transparent conducting oxide thin films for indium tin oxide transparent electrode applications. Thin Solid Films, 516(7). https://doi.org/10.1016/j.tsf.2007.03.082

Minev, I. R., Musienko, P., Hirsch, A., Barraud, Q., Wenger, N., Moraud, E. M., Gandar, J., Capogrosso, M., Milekovic, T., Asboth, L., Torres, R. F., Vachicouras, N., Liu, Q., Pavlova, N., Duis, S., Larmagnac, A., Vörös, J., Micera, S., Suo, Z., … Lacour, S. P. (2015). Electronic dura mater for long-term multimodal neural interfaces. *Science*, *347*(6218). https://doi.org/10.1126/science.1260318

Moon, H., Kwon, J., Eun, J., Chung, C. K., Kim, J. S., Chou, N., & Kim, S. (2024). Electrocorticogram (ECoG): Engineering Approaches and Clinical Challenges for Translational Medicine. *Advanced Materials Technologies*, *9*(12). https://doi.org/10.1002/admt.202301692

Muller, L., Rolston, J. D., Fox, N. P., Knowlton, R., Rao, V. R., & Chang, E. F. (2018). Direct electrical stimulation of human cortex evokes high gamma activity that predicts conscious somatosensory perception. *Journal of Neural Engineering*, *15*(2). https://doi.org/10.1088/1741-2552/aa9bf9

Muller, L., Rolston, J. D., Fox, N. P., Knowlton, R., Rao, V. R., & Chang, E. F. (2018). Direct electrical stimulation of human cortex evokes high gamma activity that predicts conscious somatosensory perception. *Journal of Neural Engineering*, *15*(2). https://doi.org/10.1088/1741-2552/aa9bf9

Norman, Y., Raccah, O., Liu, S., Parvizi, J., & Malach, R. (2021). Hippocampal ripples and their coordinated dialogue with the default mode network during recent and remote recollection. *Neuron*, *109*(17), 2767-2780.e5. https://doi.org/10.1016/j.neuron.2021.06.020

Norman, Y., Raccah, O., Liu, S., Parvizi, J., & Malach, R. (2021). Hippocampal ripples and their coordinated dialogue with the default mode network during recent and remote

recollection. *Neuron*, *109*(17), 2767-2780.e5. https://doi.org/10.1016/j.neuron.2021.06.020

Obaid, S. N., Yin, R. T., Tian, J., Chen, Z., Chen, S. W., Lee, K. B., Boyajian, N., Miniovich, A. N., Efimov, I. R., & Lu, L. (2020). Multifunctional Flexible Biointerfaces for Simultaneous Colocalized Optophysiology and Electrophysiology. *Advanced Functional Materials*, *30*(24). https://doi.org/10.1002/adfm.201910027

Ong, W. L., Low, Q. X., Huang, W., van Kan, J. A., & Ho, G. W. (2012). Patterned growth of vertically-aligned ZnO nanorods on a flexible platform for feasible transparent and conformable electronics applications. *Journal of Materials Chemistry*, *22*(17). https://doi.org/10.1039/c2jm00027j

Park, D. W., Brodnick, S. K., Ness, J. P., Atry, F., Krugner-Higby, L., Sandberg, A., Mikael, S., Richner, T. J., Novello, J., Kim, H., Baek, D. H., Bong, J., Frye, S. T., Thongpang, S., Swanson, K. I., Lake, W., Pashaie, R., Williams, J. C., & Ma, Z. (2016). Fabrication and utility of a transparent graphene neural electrode array for electrophysiology, in vivo imaging, and optogenetics. *Nature Protocols*, *11*(11). https://doi.org/10.1038/nprot.2016.127

Park, D. W., Schendel, A. A., Mikael, S., Brodnick, S. K., Richner, T. J., Ness, J. P., Hayat, M. R., Atry, F., Frye, S. T., Pashaie, R., Thongpang, S., Ma, Z., & Williams, J. C. (2014). Graphene-based carbon-layered electrode array technology for neural imaging and optogenetic applications. *Nature Communications*, *5*. https://doi.org/10.1038/ncomms6258

Pas, J., Rutz, A. L., Quilichini, P. P., Slézia, A., Ghestem, A., Kaszas, A., Donahue, M. J., Curto, V. F., O'Connor, R. P., Bernard, C., Williamson, A., & Malliaras, G. G. (2018). A bilayered PVA/PLGA-bioresorbable shuttle to improve the implantation of flexible neural probes. *Journal of Neural Engineering*, *15*(6), 065001. https://doi.org/10.1088/1741-2552/aadc1d

Prajzler, V., Nekvindová, P., Hypš, P., Lyutakov, O., & Jerˇábek, V. (2014). Flexible polymer planar optical waveguides. *Radioengineering*, *23*(3).

Qiang, Y., Artoni, P., Seo, K. J., Culaclii, S., Hogan, V., Zhao, X., Zhong, Y., Han, X., Wang, P. M., Lo, Y. K., Li, Y., Patel, H. A., Huang, Y., Sambangi, A., Chu, J. S. v., Liu,

W., Fagiolini, M., & Fang, H. (2018). Transparent arrays of bilayer-nanomesh microelectrodes for simultaneous electrophysiology and two-photon imaging in the brain. *Science Advances*, *4*(9). https://doi.org/10.1126/sciadv.aat0626

Qiang, Y., Seo, K. J., Zhao, X., Artoni, P., Golshan, N. H., Culaclii, S., Wang, P. M., Liu, W., Ziemer, K. S., Fagiolini, M., & Fang, H. (2017). Bilayer Nanomesh Structures for Transparent Recording and Stimulating Microelectrodes. *Advanced Functional Materials*, *27*(48). https://doi.org/10.1002/adfm.201704117

Ravikumar, M., Sunil, S., Black, J., Barkauskas, D. S., Haung, A. Y., Miller, R. H., Selkirk, S. M., & Capadona, J. R. (2014). The roles of blood-derived macrophages and resident microglia in the neuroinflammatory response to implanted Intracortical microelectrodes. *Biomaterials*, *35*(28), 8049–8064. https://doi.org/10.1016/j.biomaterials.2014.05.084

Renz, A. F., Lee, J., Tybrandt, K., Brzezinski, M., Lorenzo, D. A., Cerra Cheraka, M., Lee, J., Helmchen, F., Vörös, J., & Lewis, C. M. (2020). Opto-E-Dura: A Soft, Stretchable ECoG Array for Multimodal, Multiscale Neuroscience. *Advanced Healthcare Materials*, *9*(17). https://doi.org/10.1002/adhm.202000814

Richner, T. J., Thongpang, S., Brodnick, S. K., Schendel, A. A., Falk, R. W., Krugner-Higby, L. A., Pashaie, R., & Williams, J. C. (2014). Optogenetic micro-electrocorticography for modulating and localizing cerebral cortex activity. *Journal of Neural Engineering*, *11*(1). https://doi.org/10.1088/1741-2560/11/1/016010

Rubehn, B., Bosman, C., Oostenveld, R., Fries, P., & Stieglitz, T. (2009). A MEMS-based flexible multichannel ECoG-electrode array. *Journal of Neural Engineering*, *6*(3). https://doi.org/10.1088/1741-2560/6/3/036003

Saxena, T., Karumbaiah, L., Gaupp, E. A., Patkar, R., Patil, K., Betancur, M., Stanley, G. B., & Bellamkonda, R. v. (2013). The impact of chronic blood-brain barrier breach on intracortical electrode function. *Biomaterials*, *34*(20). https://doi.org/10.1016/j.biomaterials.2013.03.007

Scanziani, M., & Häusser, M. (2009). Electrophysiology in the age of light. *Nature*, *461*(7266), 930–939. https://doi.org/10.1038/nature08540

Schaft, E. v., Sun, D., Hoogteijling, S., Wang, Z., Leijten, F. S. S., van Eijsden, P., Ramsey, N. F., Robe, P., van ’t Klooster, M. A., & Zijlmans, M. (2025). Implementing intraoperative high-density electrocorticography during epilepsy surgery. *Epilepsia*, *66*(5), 1447–1461. https://doi.org/10.1111/epi.18302

Schalk, G., & Leuthardt, E. C. (2011). Brain-Computer Interfaces Using Electrocorticographic Signals. *IEEE Reviews in Biomedical Engineering*, *4*, 140–154. https://doi.org/10.1109/RBME.2011.2172408

Schendel, A. A., Thongpang, S., Brodnick, S. K., Richner, T. J., Lindevig, B. D. B., Krugner-Higby, L., & Williams, J. C. (2013). A cranial window imaging method for monitoring vascular growth around chronically implanted micro-ECoG devices. *Journal of Neuroscience Methods*, *218*(1). https://doi.org/10.1016/j.jneumeth.2013.06.001

Schweigmann, M., Caudal, L. C., Stopper, G., Scheller, A., Koch, K. P., & Kirchhoff, F. (2021). Versatile Surface Electrodes for Combined Electrophysiology and Two-Photon Imaging of the Mouse Central Nervous System. *Frontiers in Cellular Neuroscience*, *15*. https://doi.org/10.3389/fncel.2021.720675

SCS Specialty Coating Systems. (2015). Technical Data Sheet - Parylene Properties. *Retrieved from URL*, *800*. https://www.physics.rutgers.edu/~podzorov/parylene%20properties.pdf

Senzai, Y., & Buzsáki, G. (2017). Physiological Properties and Behavioral Correlates of Hippocampal Granule Cells and Mossy Cells. *Neuron*, *93*(3), 691-704.e5. https://doi.org/10.1016/j.neuron.2016.12.011

Seo, J., Kim, K., Seo, K., Kim, M. K., Jeong, S., Kim, H., Ghim, J., Lee, J. H., Choi, N., Lee, J., & Lee, H. J. (2020). Artifact-Free 2D Mapping of Neural Activity In Vivo through Transparent Gold Nanonetwork Array. *Advanced Functional Materials*, *30*(34). https://doi.org/10.1002/adfm.202000896

Shoffstall, A. J., Ecker, M., Danda, V., Joshi-Imre, A., Stiller, A., Yu, M., Paiz, J. E., Mancuso, E., Bedell, H. W., Voit, W. E., Pancrazio, J. J., & Capadona, J. R. (2018). Characterization of the neuroinflammatory response to thiol-ene shape memory polymer coated intracortical microelectrodes. *Micromachines*, *9*(10). https://doi.org/10.3390/mi9100486

Simon, D. M., Charkhkar, H., st. John, C., Rajendran, S., Kang, T., Reit, R., Arreaga-Salas, D., McHail, D. G., Knaack, G. L., Sloan, A., Grasse, D., Dumas, T. C., Rennaker, R. L., Pancrazio, J. J., & Voit, W. E. (2017). Design and demonstration of an intracortical probe technology with tunable modulus. *Journal of Biomedical Materials Research Part A*, *105*(1), 159–168. https://doi.org/10.1002/jbm.a.35896

Simon, D. M., Charkhkar, H., st. John, C., Rajendran, S., Kang, T., Reit, R., Arreaga-Salas, D., McHail, D. G., Knaack, G. L., Sloan, A., Grasse, D., Dumas, T. C., Rennaker, R. L., Pancrazio, J. J., & Voit, W. E. (2017). Design and demonstration of an intracortical probe technology with tunable modulus. *Journal of Biomedical Materials Research Part A*, *105*(1), 159–168. https://doi.org/10.1002/jbm.a.35896

Stieglitz, T., Beutel, H., Schuettler, M., & Meyer, J. U. (2000). Micromachined, polyimide-based devices for flexible neural interfaces. *Biomedical Microdevices*, *2*(4).

Stiller, A. M., Usoro, J., Frewin, C. L., Danda, V. R., Ecker, M., Joshi-Imre, A., Musselman, K. C., Voit, W., Modi, R., Pancrazio, J. J., & Black, B. J. (2018). Chronic intracortical recording and electrochemical stability of thiol-ene/acrylate shape memory polymer electrode arrays. *Micromachines*, *9*(10). https://doi.org/10.3390/mi9100500

Stiller, A. M., Usoro, J., Frewin, C. L., Danda, V. R., Ecker, M., Joshi-Imre, A., Musselman, K. C., Voit, W., Modi, R., Pancrazio, J. J., & Black, B. J. (2018). Chronic intracortical recording and electrochemical stability of thiol-ene/acrylate shape memory polymer electrode arrays. *Micromachines*, *9*(10). https://doi.org/10.3390/mi9100500

Stiller, A., Usoro, J., Lawson, J., Araya, B., González-González, M., Danda, V., Voit, W., Black, B., & Pancrazio, J. (2020). Mechanically Robust, Softening Shape Memory Polymer Probes for Intracortical Recording. *Micromachines*, *11*(6), 619. https://doi.org/10.3390/mi11060619

Stosiek, C., Garaschuk, O., Holthoff, K., & Konnerth, A. (2003). In vivo two-photon calcium imaging of neuronal networks. *Proceedings of the National Academy of Sciences*, *100*(12), 7319–7324. https://doi.org/10.1073/pnas.1232232100

Szalay, G., Judák, L., Katona, G., Ócsai, K., Juhász, G., Veress, M., Szadai, Z., Fehér, A., Tompa, T., Chiovini, B., Maák, P., & Rózsa, B. (2016). Fast 3D Imaging of Spine,

Dendritic, and Neuronal Assemblies in Behaving Animals. *Neuron*, *92*(4). https://doi.org/10.1016/j.neuron.2016.10.002

Takmakov, P., Ruda, K., Scott Phillips, K., Isayeva, I. S., Krauthamer, V., & Welle, C. G. (2015). Rapid evaluation of the durability of cortical neural implants using accelerated aging with reactive oxygen species. *Journal of Neural Engineering*, *12*(2), 026003. https://doi.org/10.1088/1741-2560/12/2/026003

Thunemann, M., Lu, Y., Liu, X., Kılıç, K., Desjardins, M., Vandenberghe, M., Sadegh, S., Saisan, P. A., Cheng, Q., Weldy, K. L., Lyu, H., Djurovic, S., Andreassen, O. A., Dale, A. M., Devor, A., & Kuzum, D. (2018). Deep 2-photon imaging and artifact-free optogenetics through transparent graphene microelectrode arrays. *Nature Communications*, *9*(1). https://doi.org/10.1038/s41467-018-04457-5

Toda, H., Suzuki, T., Sawahata, H., Majima, K., Kamitani, Y., & Hasegawa, I. (2011). Simultaneous recording of ECoG and intracortical neuronal activity using a flexible multichannel electrode-mesh in visual cortex. *NeuroImage*, *54*(1). https://doi.org/10.1016/j.neuroimage.2010.08.003

Torres, D., Makarova, J., Ortuño, T., Benito, N., Makarov, V. A., & Herreras, O. (2019). Local and Volume-Conducted Contributions to Cortical Field Potentials. *Cerebral Cortex*, *29*(12), 5234–5254. https://doi.org/10.1093/cercor/bhz061

Tóth, R., Miklós Barth, A., Domonkos, A., Varga, V., & Somogyvári, Z. (2021). Do not waste your electrodes - Principles of optimal electrode geometry for spike sorting. *Journal of Neural Engineering*, *18*(4). https://doi.org/10.1088/1741-2552/ac0f49

Tsien, R. W., & Tsien, R. Y. (1990). Calcium Channels, Stores, and Oscillations. *Annual Review of Cell Biology*, *6*(1), 715–760. https://doi.org/10.1146/annurev.cb.06.110190.003435

Tsien, R. Y. (2003). Imagining imaging's future. *Nature Reviews. Molecular Cell Biology*, *Suppl*, SS16-21.

Uludağ, K., & Roebroeck, A. (2014). General overview on the merits of multimodal neuroimaging data fusion. *NeuroImage*, *102*, 3–10. https://doi.org/10.1016/j.neuroimage.2014.05.018

Vitale, F., Shen, W., Driscoll, N., Burrell, J. C., Richardson, A. G., Adewole, O., Murphy, B., Ananthakrishnan, A., Oh, H., Wang, T., Lucas, T. H., Kacy Cullen, D., Allen, M. G., & Litt, B. (2018). Biomimetic extracellular matrix coatings improve the chronic biocompatibility of microfabricated subdural microelectrode arrays. *PLoS ONE*, *13*(11). https://doi.org/10.1371/journal.pone.0206137

Walczak, R., Śniadek, P., & Dziuban, J. A. (2011). SU-8 photoresist as material of optical passive components integrated with analytical microsystems for real-time polymerase chain reaction. *Optica Applicata*, *41*(4).

Ware, T., Simon, D., Hearon, K., Liu, C., Shah, S., Reeder, J., Khodaparast, N., Kilgard, M. P., Maitland, D. J., Rennaker, R. L., & Voit, W. E. (2012). Three-dimensional flexible electronics enabled by shape memory polymer substrates for responsive neural interfaces. *Macromolecular Materials and Engineering*, *297*(12). https://doi.org/10.1002/mame.201200241

Ware, T., Simon, D., Liu, C., Musa, T., Vasudevan, S., Sloan, A., Keefer, E. W., Rennaker, R. L., & Voit, W. (2014). Thiol-ene/acrylate substrates for softening intracortical electrodes. *Journal of Biomedical Materials Research Part B: Applied Biomaterials*, *102*(1), 1–11. https://doi.org/10.1002/jbmb.32946

Ware, T., Simon, D., Liu, C., Musa, T., Vasudevan, S., Sloan, A., Keefer, E. W., Rennaker, R. L., & Voit, W. (2014). Thiol-ene/acrylate substrates for softening intracortical electrodes. *Journal of Biomedical Materials Research Part B: Applied Biomaterials*, *102*(1), 1–11. https://doi.org/10.1002/jbmb.32946

Watanabe, S., Takahashi, H., & Torimitsu, K. (2017). Electroconductive polymer-coated silk fiber electrodes for neural recording and stimulation in vivo. *Japanese Journal of Applied Physics*, *56*(3), 037001. https://doi.org/10.7567/JJAP.56.037001

Weiergräber, M., Papazoglou, A., Broich, K., & Müller, R. (2016). Sampling rate, signal bandwidth and related pitfalls in EEG analysis. *Journal of Neuroscience Methods*, *268*, 53–55. https://doi.org/10.1016/j.jneumeth.2016.05.010

Wellman, S. M., Eles, J. R., Ludwig, K. A., Seymour, J. P., Michelson, N. J., McFadden, W. E., Vazquez, A. L., & Kozai, T. D. Y. (2018). A Materials Roadmap to Functional

Neural Interface Design. In *Advanced Functional Materials* (Vol. 28, Issue 12). https://doi.org/10.1002/adfm.201701269

Wu, F., Im, M., Yoon, E. (*2011) 16th Int. Solid-State Sensors, Actuators Microsystems Conf. TRANSDUCERS'11*, IEEE, New York **2011**, pp. 966–969.

Wu, F., Tien, L. W., Chen, F., Berke, J. D., Kaplan, D. L., & Yoon, E. (2015). Silk-backed structural optimization of high-density flexible intracortical neural probes. *Journal of Microelectromechanical Systems*, *24*(1). https://doi.org/10.1109/JMEMS.2014.2375326

Wurth, S., Capogrosso, M., Raspopovic, S., Gandar, J., Federici, G., Kinany, N., Cutrone, A., Piersigilli, A., Pavlova, N., Guiet, R., Taverni, G., Rigosa, J., Shkorbatova, P., Navarro, X., Barraud, Q., Courtine, G., & Micera, S. (2017). Long-term usability and bio-integration of polyimide-based intra-neural stimulating electrodes. *Biomaterials*, *122*. https://doi.org/10.1016/j.biomaterials.2017.01.014

Xiao, X., Qiu, X., Kong, D., Zhang, W., Liu, Y., & Leng, J. (2016). Optically transparent high temperature shape memory polymers. *Soft Matter*, *12*(11), 2894–2900. https://doi.org/10.1039/C5SM02703A

Yang, W., Gong, Y., Yao, C.-Y., Shrestha, M., Jia, Y., Qiu, Z., Fan, Q. H., Weber, A., & Li, W. (2021). A fully transparent, flexible PEDOT:PSS–ITO–Ag–ITO based microelectrode array for ECoG recording. *Lab on a Chip*, *21*(6), 1096–1108. https://doi.org/10.1039/D0LC01123A

Yu, K. J., Kuzum, D., Hwang, S. W., Kim, B. H., Juul, H., Kim, N. H., Won, S. M., Chiang, K., Trumpis, M., Richardson, A. G., Cheng, H., Fang, H., Thompson, M., Bink, H., Talos, D., Seo, K. J., Lee, H. N., Kang, S. K., Kim, J. H., … Rogers, J. A. (2016). Bioresorbable silicon electronics for transient spatiotemporal mapping of electrical activity from the cerebral cortex. *Nature Materials*, *15*(7). https://doi.org/10.1038/nmat4624

Zátonyi, A., Borhegyi, Z., Srivastava, M., Cserpán, D., Somogyvári, Z., Kisvárday, Z., & Fekete, Z. (2018). Functional brain mapping using optical imaging of intrinsic signals and simultaneous high-resolution cortical electrophysiology with a flexible, transparent microelectrode array. *Sensors and Actuators, B: Chemical*, *273*. https://doi.org/10.1016/j.snb.2018.06.092

Zátonyi, A., Madarász, M., Szabó, O., Lőrincz, T., Hodován, R., Rózsa, B., & Fekete, Z. (2020). Transparent, low-autofluorescence microECoG device for simultaneous Ca2+ imaging and cortical electrophysiology in vivo. *Journal of Neural Engineering*, *17*(1). https://doi.org/10.1088/1741-2552/ab603f

Zátonyi, A., Orbán, G., Modi, R., Márton, G., Meszéna, D., Ulbert, I., Pongrácz, A., Ecker, M., Voit, W. E., Joshi-Imre, A., & Fekete, Z. (2019). A softening laminar electrode for recording single unit activity from the rat hippocampus. *Scientific Reports*, *9*(1). https://doi.org/10.1038/s41598-019-39835-6

Zhang, J., Liu, X., Xu, W., Luo, W., Li, M., Chu, F., Xu, L., Cao, A., Guan, J., Tang, S., & Duan, X. (2018). Stretchable Transparent Electrode Arrays for Simultaneous Electrical and Optical Interrogation of Neural Circuits in Vivo. *Nano Letters*, *18*(5). https://doi.org/10.1021/acs.nanolett.8b00087

9. Bibliography of the candidate's publications

Articles related to thesis

Juhász, Gábor; Madarász, Miklós; Szmola, Benedek.; Fedor, Flóra Zsófia; Balogh-Lantos, Zsófia; Szabó, Ágnes; Rózsa, Balázs; Fekete, Zoltán. Hippocampal recording with a soft microelectrode array in a cranial window imaging scheme: a validation study SCIENTIFIC REPORTS 14 : 1 Paper: 24585, 13 p. (2024)

Madarász, Miklós*; Fedor, Flóra Zsófia*; Fekete, Zoltán; Rózsa, Balázs. Immunohistological responses in mice implanted with Parylene HT – ITO ECoG devices. FRONTIERS IN NEUROSCIENCE 17 Paper: 1209913, 8 p. (2023)

Szabó, Ágnes; Madarász, Miklós; Lantos, Zsófia; Zátonyi, Anita; Danda, Vindhya; Spurgin, Lisa; Manz, Connie; Rózsa, Balázs; Fekete, Zoltán. Transparent Thiol-ene/Acrylate-Based MicroECoG Devices Used for Concurrent Recording of Fluorescent Calcium Signals and Electrophysiology in Awake Animals. ADVANCED MATERIALS INTERFACES 9 : 25 Paper: 2200729, 10 p. (2022)

Fedor, Flóra Zsófia*; Madarász, Miklós*; Zátonyi, Anita; Szabó, Ágnes; Lőrincz, Tibor; Danda, Vindhya; Spurgin, Lisa; Manz, Connie; Rózsa, Balázs; Fekete, Zoltán. Soft, Thiol-ene/Acrylate-Based Electrode Array for Long-Term Recording of Intracranial EEG Signals with Improved Biocompatibility in Mice. ADVANCED MATERIALS TECHNOLOGIES 7 : 5 Paper: 2100942, 10 p. (2022)

Zátonyi, A*; Madarász, M*; Szabó, Á*; Lőrincz, T; Hodován, R; Rózsa, B; Fekete, Z. Transparent, low-autofluorescence microECoG device for simultaneous Ca 2+ imaging and cortical electrophysiology in vivo. JOURNAL OF NEURAL ENGINEERING 17 : 1 Paper: 016062, 17 p. (2020)

Fekete, Zoltán; Zátonyi, Anita; Kaszás, Attila; Madarász, Miklós; Slézia, Andrea. Transparent neural interfaces: challenges and solutions of microengineered multimodal implants designed to measure intact neuronal populations using high-resolution electrophysiology and microscopy simultaneously. MICROSYSTEMS & NANOENGINEERING 9 Paper: 66, 30 p. (2023)

Other articles

Csomos, Attila; Madarász, Miklós; Turczel, Gábor; Cseri, Levente; Katona, Gergely; Rózsa, Balázs; Kovács, Ervin; Mucsi, Zoltán. A Molecular Hybrid of the GFP Chromophore and 2,2′-Bipyridine: An Accessible Sensor for Zn2+ Detection with Fluorescence Microscopy. INTERNATIONAL JOURNAL OF MOLECULAR SCIENCES 25 : 6 Paper: 3504, 14 p. (2024)

Attila, Csomos; Miklós, Madarász; Gábor, Turczel; Levente, Cseri; Andrea, Bodor; Anett, Matuscsák; Gergely, Katona; Ervin, Kovács; Balázs, Rózsa; Zoltán, Mucsi. A GFP inspired 8-methoxyquinoline-derived fluorescent molecular sensor for the detection of Zn2+ by two-photon microscopy. CHEMISTRY-A EUROPEAN JOURNAL 30 : 31 Paper: e202400009, 7 p. (2024)

Csomos, Attila; Kovács, Ervin; Madarász, Miklós; Fedor, Flóra Zsófia; Fülöp, Anna; Katona, Gergely; Rózsa, Balázs; Mucsi, Zoltán. Two-Photon Fluorescent Chemosensors Based on the GFP-Chromophore for the Detection of Zn2+ in Biological Samples – From Design to Application. SENSORS AND ACTUATORS B-CHEMICAL 398 Paper: 134753, 14 p. (2024)

Chiovini, Balázs; Pálfi, Dénes; Majoros, Myrtill; Juhász, Gábor; Szalay, Gergely; Katona, Gergely; Szőri, Milán; Frigyesi, Orsolya; Lukácsné, Haveland Csilla; Szabó, Gábor; Erdélyi, Ferenc; Máté, Zoltán; Szadai, Zoltán; Madarász, Miklós; Dékány, Miklós; Csizmadia, Imre Gyula; Kovács, Ervin; Rózsa, Balázs; Mucsi, Zoltán. Theoretical Design, Synthesis, and In Vitro Neurobiological Applications of a Highly Efficient Two-Photon Caged GABA Validated on an Epileptic Case. ACS OMEGA 6 : 23 pp. 15029-15045. , 17 p. (2021)

Pálfi, Dénes; Chiovini, Balázs; Szalay, Gergely; Kaszás, Attila; Turi, Gergely; Katona, Gergely; Ábrányi-Balogh, Péter; Szőri, Milán; Potor, Attila; Frigyesi, Orsolya; Lukácsné Haveland, Csilla; Szadai, Zoltán; Madarász, Miklós; Vasanits-Zsigrai, Anikó; Molnár-Perl, Ibolya; Viskolcz, Béla; Csizmadia, Imre Gyula; Mucsi, Zoltán; Rózsa, Balázs. High efficiency two-photon uncaging coupled by the correction of spontaneous hydrolysis. ORGANIC & BIOMOLECULAR CHEMISTRY 16 : 11 pp. 1958-1970., 13 p. (2018)

Szalay, Gergely; Judák, Linda; Szadai, Zoltán; Chiovini, Balázs; Mezei, Dávid; Pálfi, Dénes; Madarász, Miklós; Ócsai, Katalin; Csikor, Ferenc; Veress, Máté; Maák, Pál; Katona, Gergely. Háromdimenziós, gyors, kétfoton-pásztázó eljárások sejt- és hálózatszintű idegsejtvizsgálatokhoz. ORVOSI HETILAP 156 : 52 pp. 2120-2126., 7 p. (2015)

10. Author Contribution

Packaging of the Parylene HT / ITO device was performed by Anita Zátonyi, Ágnes Szabó, Zsófia Lantos and Zoltán Fekete. Packaging of the Thiol-ene/acrylate was performed by Vindhya Danda, Lisa Spurgin and Connie Manz. Anita Zátonyi performed transmittance, autofluorescence and electrode impedance spectroscopy measurements. Ágnes Szabó performed neurite detection and neurite size analysis, analysis of light - induced artefacts, analysis of fluorescent microbead size and electrode impedance spectroscopy measurements. Benedek Szmola created code for the analysis of SPW-Rs. Flóra Zsófia Fedor performed immunohistological processing, staining and epifluorescence imaging. Gábor Juhász performed hippocampal implantation and analysis of sharp-wave ripples. Róbert Hodován performed the cyclic mechanical load experiments entirely. Tibor Lőrinc performed the analysis of activity rate and decay time for the Parylene HT / ITO device. Zsófia Balogh-Lantos performed analysis of single unit and multiunit activity.

11. Acknowledgements

First of all, let me warmly thank my supervisor, Dr. Rózsa J. Balázs, for the opportunity of joining his research group and his continued support ever since. Starting from a Bachelor's thesis until the completion of my dissertation, it has been a transformative experience from student to researcher that fundamentally influenced me during my years of learning.

I want to thank all of my colleagues, former and current, pupils, fellow students and mentors for all of their little and not so little help over this long and arduous journey that put me where I am now. Thank You!

Let me express my gratitude to the members of the NeuroMEMS group, whose positive and friendly attitude made the hard work of many published articles enjoyable. Accompanying them on their own path to graduation was truly enjoyable and helped me to move forward on my own one. The support and guidance of the late Dr. Zoltán Fekete have been especially invaluable to me. His encouragement and enthusiasm helped me greatly in both our collaborative work and in my progression as a researcher.

There is no chance that I would omit mentioning the friendship and support of Balázs Chiovini, Dénes Pálfi, Zsolt Mezriczky, Zoltán Szadai, Linda Sulcz-Judák and Gergely Szalay. Their goodwill, guidance and high spirits are firmly tied to my first years in the group and motivated me ever since. Part of this, but also more involved in a way, was Gábor Juhász. Above everything else, I would like to thank him for his perseverance in our common work and his quiet but always essential insights.

I want to say thanks to Flóra Fedor, who became my fast friend in the first project and who I could rely on ever since. Here is your tpyo!

Special thanks go to the team at KOKI, particularly to Áron Szepesi and to the new and the old guard: thank you for the jokes and the cheers and the final push on the last leg.

I would like to say thank you to my friends and family for standing with me during this period of my life and being so patient with me. I wouldn't have gotten far without you.

There are no words that would describe the love and support that I received from my wife Detti and the hardships I put her through during my PhD. I'm so sorry for the difficulties and thank you from the bottom of my heart for enduring them.